Very High Numerical Aperture Three-Dimensional Imaging with Three Objectives

by

Thomas Pearce Huelsnitz

(Under the Direction of Peter Kner)

Abstract

The increasing importance of three dimensional observation in biology necessitates advances in three dimensional microscopy techniques. In widefield and confocal microscopy, lateral resolution is 2 to 3 times better than axial resolution. This anisotropic resolution leads to poor three-dimensional imaging. We propose a microscope which utilizes three high numerical aperture objectives to image a sample from multiple angles and interferometrically combine the information from each objective to obtain a higher resolution and more isotropic point spread function than standard widefield and confocal techniques. The proposed microscope has a higher effective numerical aperture than standard techniques, thus it is more efficient at collecting light emitted from the sample. This improves the microscope's signal to noise ratio and, in the context of fluorescence microscopy, reduces photobleaching. Here we introduce the theoretical framework for describing the performance of a microscope and then we apply that same reasoning to quantitatively compare our proposed microscope to existing techniques.

INDEX WORDS: Isotropic Resolution, Three Objectives, Interferometry, 3D Imaging

Very High Numerical Aperture Three-Dimensional Imaging with Three Objectives

by

Thomas Pearce Huelsnitz

BS, University of Georgia, 2012

A Thesis Submitted to the Graduate Faculty of The University of Georgia in Partial Fulfillment of the Requirements for the Degree

Master of Science

Athens, Georgia

2015

Very High Numerical Aperture Three-Dimensional Imaging with Three Objectives

by

Thomas Pearce Huelsnitz

Major Professor:	Peter Kner
Committee:	Mable Fok
	Mark Haidekker

Electronic Version Approved:

Julie Coffield
Interim Dean of the Graduate School
The University of Georgia
May 2015

Acknowledgements

I sincerely appreciate the assistance and guidance that I have received from my major professor, Dr. Peter Kner. Through his effort I have learned far than I could have on my own and he has been kind and understanding throughout the entire process.

I also owe a debt of gratitude to my committee members Dr. Mark Haidekker and Dr. Mable Fok. Dr. Haidekker has been a constant positive influence on me throughout my time here. I have thoroughly enjoyed all of his courses and my experience working with him as a teaching assistant.

I thank my lab mate Kayvan Forouhesh Tehrani for his assistance and good nature throughout the last two years. He has been a great help and a true friend.

I would also like to thank Mrs. Clodagh Phair-Miller for her patience and understanding, especially when I register for classes after the deadline. Finally, thank you to Ms. Aretha Gartrell for always stopping and chatting with me in the hall and having encouraging words for me.

Table of Contents

Page

Acknowledgements ..... **iv**

Nomenclature ..... **vii**

Chapters

1 Introduction **1**

1.1 Purpose of Study 1

1.2 Thesis Objective and Organization 3

2 Background **5**

2.1 Introduction to Fluorescence Microscopy 5

2.2 The Microscope as a Linear System 7

2.3 Frequency Space Analysis of Single Objective Techniques 12

2.4 Out of Focus Light and 3D Imaging 16

2.5 The PSF as a Measure of Performance 20

3 Literature Review **27**

3.1 Mirror Techniques 27

3.2 Multiple-Objective Techniques 29

3.3 PSF Improvement with Pupil Filters 36

4 Confocal Analysis Methods **39**

4.1 Confocal Illumination 40

4.2 The Phase at Pupils 45

4.3 System Pupil 49

4.4 Pupil Clipping 52

4.5 Confocal Detection 53

5 Widefield Analysis Methods 56

5.1 Widefield Illumination 56

5.2 Widefield Detection 57

6 Results 66

6.1 Confocal Results 68

6.2 Pupil Phase Results and System Pupil Verification 79

6.3 Widefield Results 82

7 Discussion and Conclusion 89

7.1 Additional Advantages of Three-objective Arrangement 89

7.2 Microscope Design 90

7.3 Conclusion 91

References 94

Appendices

A.1 Objective Dimensions 96

A.2 Confocal Code 97

A.3 Phase at Pupils Code 101

A.4 Widefield Code 106

A.3 Utility Modules 110

Nomenclature

NA	Numerical aperture
F	Focal length
λ	Wavelength
PSF	Point spread function
OTF	Optical transfer function
u	Scalar electric field amplitude
h	Coherent point spread function
$\tilde{u}$	Coherent transfer function
I	Intensity
H	Incoherent point spread function
$\tilde{H}$	Incoherent transfer function
M	Magnification
$\vec{E}$	Electric field
P	Pupil function

Chapter 1

Introduction

1.1 Purpose of Study

The importance of imaging samples in a 3D environment is being recognized in the biological sciences.[1-3] Confining samples to two dimensions does not accurately reflect their in vivo environment and often leads to incorrect conclusions in biology research. An example is the study of Human osteosarcoma cells. These cells express hypoxia inducible factor[1] (HIF-1) when placed in a low oxygen environment. It has been observed that cells grown in monolayer do not express HIF-1 when submitted to hypoxia, whereas cells grown in a multicellular tumor spheroid model do express HIF-1, just as they would inside the body.[1] Similarly, the observation of human dendritic cell motility upon removal of an enzyme crucial for coordinating cell contortion led to two drastically different conclusions depending on whether the experiment was done in a two dimensional medium or a three dimensional medium.[2] These are just two examples of the detrimental effect of imaging biological samples is 2D environments. There are countless other examples of similar behavior throughout the literature. In general, neighboring cells communicate through their extra cellular matrix (ECM). When cells are grown in a monolayer, the ECM does not fully develop. Often times this leads to behavior which deviates from what happens in vivo.[3]

Innovations in imaging techniques are needed in order for biologists to fully exploit three-dimensional observation.[3] The Point Spread Function (PSF) is a measure of how well a microscope resolves a single point source. It is a fundamental characteristic of the microscope which directly quantifies its resolution capabilities. Today, widefield and confocal microscopy are the two most

commonly used microscopy techniques in biology. These techniques both have PSFs which are larger in the axial direction than in the lateral direction (Fig. 1.1). Due to the shape of their PSFs, these techniques achieve lateral resolutions of about 200 nm and axial resolutions around 600 nm. This resolution anisotropy is a hindrance for 3D imaging.

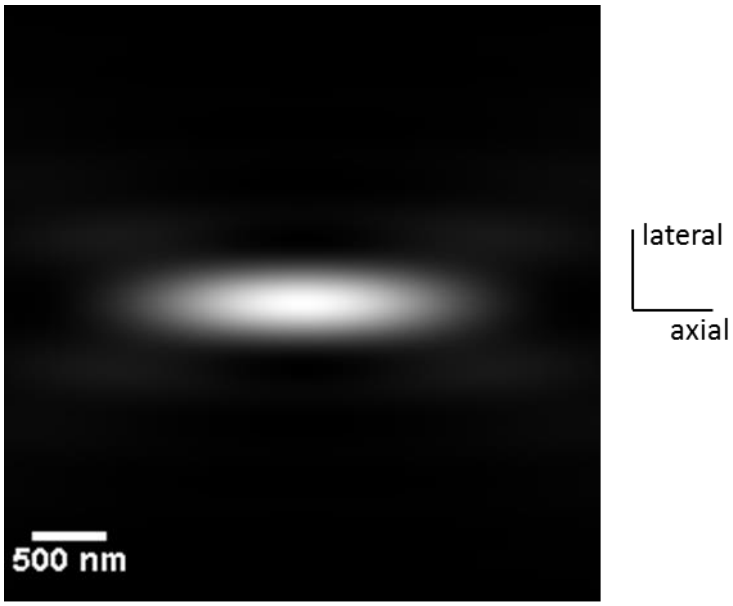

Fig. 1.1 Note the disparity in axial and lateral extent of the PSF. This translates directly to anisotropic resolution where axial resolution is approximately three times worse than lateral resolution.

Additionally, these arrangements do not make optimum use of the fluorescence light from the sample. Every photon of excitation light and corresponding fluorescence emission from the sample is precious in fluorescence microscopy. In any given fluorophore, a finite number of photons will be emitted before photobleaching occurs. Thus, an ideal microscope is one that gathers light as efficiently as possible. Standard widefield and confocal techniques fall short of what is possible.

We propose a new solution to the shortcomings of confocal and widefield microscopy. A microscope which uses three co-planar objectives with a common focal point and 120° separation between them (Fig 1.2), will have a more isotropic PSF and significantly better light gathering efficiency than existing techniques. The figure shown here is a simplified version of the optical setup. In a

confocal configuration, there would be spatial light modulators and deformable mirrors along each of the optical paths (Ch. 4). In a widefield arrangement, several additional optical components must be introduced (Ch. 5).

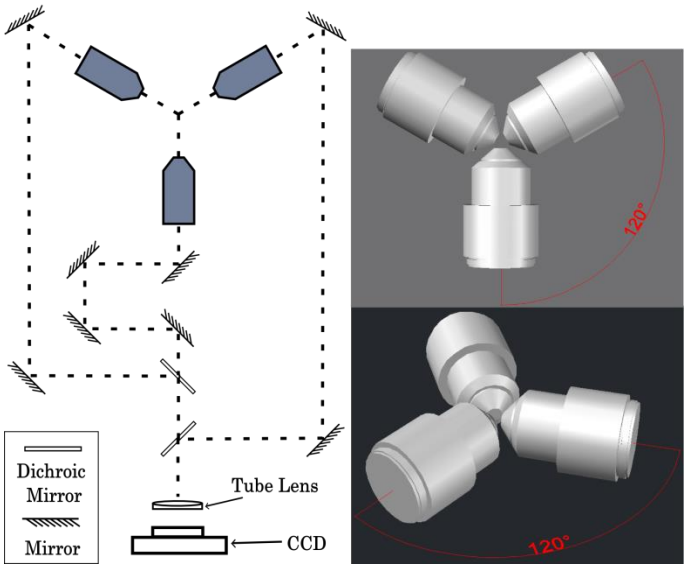

Fig. 1.2 Simplified schematic of the proposed system. The exit pupils from each objective are interferometrically combined on the tube lens. The tube lens then creates an image which is detected by the CCD. We chose an existing microscope objective which satisfies the physical requirements of our proposed system and modeled it to show that the arrangement is possible. This particular objective has a working distance of 2.4 mm and a numerical aperture of 0.9. In a confocal configuration, there would be spatial light modulators and deformable mirrors along each of the optical paths. In a widefield arrangement, several additional optical components must be introduced.

1.2 Thesis Objective and Organization

In this thesis, we will quantitatively describe the performance of the proposed system through theoretical modeling and simulation. We begin with background information regarding Fourier optics, the point spread function (PSF), the optical transfer function (OTF) and the relationship between them in Chapter 2. Chapter 3 is a literature review which is a brief overview of other techniques which attempt to overcome the resolution anisotropy of standard microscopy techniques. In Chapter 4, we discuss the methods employed to quantitatively describe the three-objective arrangement in a point scanning, confocal technique. Chapter 5 covers the methods for describing the arrangement employed

in a widefield technique. The data and analysis for the confocal and the widefield approaches are presented in Chapter 6. Finally, in Chapter 7 we conclude the thesis with a brief discussion of additional advantages and technical considerations of the proposed system, an assessment of the viability of the three-objective arrangement, and an outlook towards future research goals.

Chapter 2

Background

2.1 Introduction to Fluorescence Microscopy

Fluorescence microscopy is a form of light microscopy which is widely used in the biological sciences. It utilizes fluorescent molecules called fluorophores to label features of interest in biological samples. Fluorophores can be selectively attached to specific proteins within a sample. A specific wavelength range of illumination light raises these fluorophores to the excited state. As a fluorophore returns to the ground state, it emits a photon of a longer wavelength than the original, absorbed photon.

The general setup of an epifluorescence microscope is shown in Fig. 2.1. This is a specific type of fluorescence microscope in which illumination and detection are performed along the same optical path. In Fig. 2.1, the desired illumination wavelength is isolated by means of an emission filter. Alternatively, a laser of the correct wavelength can be used. Resulting fluorescence light from the fluorophores is then collected by the objective. The return path will have light from the fluorophores as well as some illumination light reflected by the sample. The emission filter filters out the reflected illumination light and only transmits the light from the fluorophores. These photons emitted by the fluorophores are then imaged onto the detector. This is typically either a charge-coupled device (CCD) in a widefield microscope or a pinhole aperture and photomultiplier tube in a confocal microscope.

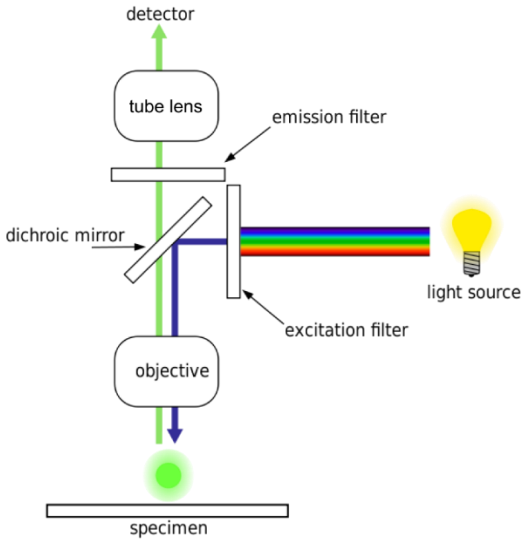

Fig. 2.1 Schematic of an epifluorescence microscope.

Most microscope objectives are designed to obey the Abbe sine condition. This means that object points in the focal plane of the objective form perfectly stigmatic image points at the back focal plane of the tube lens. Object points not in the focal plane of the objective form spherically aberrated image points. In an infinity corrected microscope, the Abbe sine condition means that rays emerging from a point in the focal plane of the objective will be collimated by the objective. This collimated light is then focused by the tube lens (Fig. 2.1) to form a perfectly stigmatic image point in the back focal plane of the tube lens. All rays emerging from the object are focused to the same point in image space. An object point which is axially displaced from the focal plane of the objective, or defocused, produces rays which are not perfectly collimated by the objective. Since the resulting rays incident on the tube lens are not parallel, they are focused to different points on the optic axis, essentially spreading the image of the point object along the optic axis. This is called spherical aberration.

The numerical aperture (NA) is an important parameter of any microscope. It is a dimensionless number which describes the range of angles over which the microscope accepts or emits light. It is defined as $NA = n \sin\theta$ where n is the index of refraction of the sample and θ is the half-angle of the maximum cone of light that can enter or exit the microscope. The Airy disk is the diffraction pattern which results from a uniformly illuminated circular aperture. The Airy disk

distribution is defined as $2\mathcal{J}_1(\chi)/\chi$ where $\mathcal{J}_1$ is the first-order Bessel function of the first kind. When a microscope images incoming plane waves, the intensity distribution in the image space is described by the Airy disk. A possible source of incident plane waves is a point source sufficiently far from the aperture that the curvature of the wavefronts is essentially planar. The numerical aperture is important because it determines the radius of the Airy disc, and thus the microscope's resolution. The Abbe diffraction limit states that the minimum radius of the Airy disc formed from incoming plane waves is $d = \lambda/2NA$ where λ is the wavelength of light. This is the physical limit to resolution in a light microscope. We call a system which achieves this level of resolution a diffraction-limited system.

Other imaging modalities such as electron microscopy or x-ray microscopy outperform fluorescence microscopy in various aspects. Electron microscopy can achieve of resolutions as low as $.05\text{ nm}$, whereas fluorescence microscopy is physically limited to about $140\ nm$ (assuming $NA = 1.4, \lambda = 390\text{ nm}$). X-ray microscopy can penetrate deeper into tissues than light microscopy and is capable of resolutions of about 20 nm. Fluorescence microscopy is important because it is better suited for biological imaging than these methods. Its main advantage is that it allows labeling of specific proteins in live samples. X-ray radiation is destructive to biological samples and the sample preparation process for an electron microscope involves freezing the sample and slicing it into layers of only $\sim 100\text{ nm}$ thickness due to the microscope's poor penetration into sample tissues. Fluorescence microscopy allows rapid imaging with moderate depth penetration and, relative to x-ray and electron microscopy, does not harm the sample. Therefore it is well suited for imaging of biological specimens and is an important tool for biologists.

2.2 The Microscope as a Linear System

A system is defined to be a mapping of a set of input functions to a set of output functions. If the system receives some input function, $u_1(x_1, y_1)$, then the output of the system is

$$u_2(x_2,y_2) = R\left[u_1(x_1,y_1)\right], \tag{2.1}$$

where R is the response of the system. In the case of electronics, these functions are voltage or current, dependent upon time. Similarly, a microscope can be treated as a system where the input functions and output functions are light intensity or electric field amplitude as two-dimensional functions of space. Presented here is a brief overview of this concept and its implications for microscopy. For a more thorough treatment, the reader is referred to the introductory text by Goodman.[4]

A microscope can be treated as a linear system. This type of system obeys the superposition principle, which states that the response of the system to a set of input functions is the superposition of the system's responses to the individual functions:

$$R\left[af(x_1,y_1)+bg(x_1,y_1)\right] = aR\left[f(x_1,y_1)\right]+bR\left[g(x_1,y_1)\right], \tag{2.2}$$

Where a and b are constants. To take advantage of this, we must find a way to decompose the input into its parts. For this, we can use the Dirac delta function which has the property

$$u_1(x_1,y_1) = \iint_{-\infty}^{\infty} u_1(\xi,\eta)\delta(x_1-\xi,y_1-\eta)\,d\xi\,d\eta\,. \tag{2.3}$$

At first glance, Eqs. 2.2 and 2.3 look very different, but they are actually quite similar. We can treat Eq. 2.3 as a superposition of many delta functions, each weighted by the function, $u_1(\xi,\eta)$. Here, $u_1(\xi,\eta)$ is analogous to a or b in Eq. 2.2. We can combine Eqs. 2.3 and 2.1 and, in a similar fashion to Eq. 2.2, we can say

$$u_2(x_2,y_2) = \iint_{-\infty}^{\infty} u_1(\xi,\eta)R\left[\delta(x_1-\xi,y_1-\eta)\right]d\xi\,d\eta\,. \tag{2.4}$$

The term $R\left[\delta\left(x_1-\xi, y_1-\eta\right)\right]$ is the response of the system at point $\left(x_2, y_2\right)$ to a delta function at point (ξ,η). This quantity is called the impulse response of the system and it is such a fundamentally important function that we will denote it $h\left(x_2, y_2; \xi,\eta\right)$.

Applying this treatment to a microscope allows us to take a "black box" approach in which we are only concerned with the relationship between the electric field distribution (or intensity) in the four planes shown in Fig. 2.2. For a coherent source, we say that the system is linear in electric field amplitude. Using the general setup shown in Fig. 2.2, the electric field distribution in the image plane is related to the field distribution in the object plane by

$$u_i(u,v)=\iint_{-\infty}^{\infty} h(u,v;\xi,\eta)u_O(\xi,\eta)d\xi d\eta, \tag{2.5}$$

where u_i is the image plane distribution, u_o is the object plane distribution and h is the Point Spread Function (PSF). The PSF is the impulse response of a microscope and it describes the field at a point (u,v) in image space due to a point source at (ξ,η) in object space. Here we will further assume that the impulse response (PSF) is space-invariant. The image of a point source changes in location but not distribution as the point source is moved throughout the object space. In practice, this is only approximately true for optical systems over certain regions of the object space. A region over which the PSF can be considered space-invariant is referred to as an isoplanatic patch.

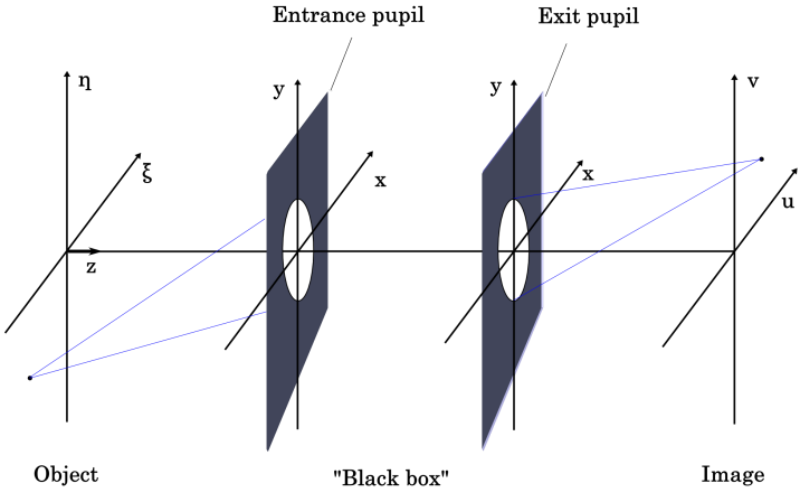

Fig. 2.2 We can treat a microscope as a linear system where, in the case of coherent light, the electric field amplitude distribution in object space is mapped to image space through a convolution operation in real space coordinates or a transfer function multiplication in frequency space. In the case of coherent light, a similar relationship holds, but in terms of the light intensity rather than the field amplitude. We are only interested in the field or intensity distribution at the object/image planes and the entrance/exit pupils. We assume that everything occurring inside the "black box" is correctly described by geometrical optics.

In order to assess the general behavior of a typical PSF, we turn to scalar diffraction theory. Goodman shows[4] that a system obeying the lens law, $(1/z_1)+(1/z_2)=1/f$, where z_1 is the distance from the object plane to the first principal plane, z_2 is the distance from second principal plane to the image plane and f is the system focal length has a PSF of the form

$$h(u,v;\xi,\eta)=\frac{A}{\lambda z_2}\int_{\Sigma}\exp\left\{-j\frac{2\pi}{\lambda z_2}\left[(u-\xi)x+(v-\eta)y\right]\right\}dxdy\,, \tag{2.6}$$

where A is the constant field amplitude, λ is the wavelength of the light source and Σ represents the set of all points (x,y) on the exit pupil. Eq. 2.6 is a simplified form of the Fresnel approximation. As mentioned, this form assumes the lens law is satisfied by the system. Additionally, a magnification of unity is assumed. Finally, a phase term dependent upon *(u,v)* has been neglected. This is justified by the fact that the intensity is the quantity of interest and so these phase terms cancel when converting from the electric field to the intensity since the intensity is the magnitude squared of the electric field. The Fresnel approximation is a small angle approximation. Thus, for high aperture situations it is

inaccurate, but it will suffice for the current discussion. Eq. 2.6 can be written in the form of a convolution integral:

$$u_i(u,v) = \iint_{-\infty}^{\infty} h(u-\xi, v-\eta)\, u_O(\xi,\eta)\, d\xi d\eta \,. \tag{2.7}$$

By the Fourier convolution theorem, this can be recast in frequency space as

$$\tilde{u}_i(k_x,k_y) = \tilde{h}(k_x,k_y)\,\tilde{u}_o(k_x,k_y), \tag{2.8}$$

where $\tilde{u}$ represents the Fourier transform of u and $\tilde{h}$ is called the Amplitude Transfer Function (ATF). This is an important result which greatly simplifies the relation between the image plane amplitude distribution and the object plane amplitude distribution.

A similar relation holds for an incoherent source, such as a fluorophore used in fluorescent imaging. In this case, however, we say that the system is linear in intensity rather than field amplitude. This is quite practical since we measure light intensity rather than field amplitude. For an incoherent system, the following two equations are valid:

$$I_i(u,v) = \iint_{-\infty}^{\infty} H(u-\xi, v-\eta)\, I_O(\xi,\eta)\, d\xi d\eta \;, \tag{2.9}$$

$$\tilde{I}_i(k_X,k_Y) = \tilde{H}(k_X,k_Y)\,\tilde{I}_O(k_X,k_Y) \;, \tag{2.10}$$

where I represents intensity, $H = |h(u-\xi, v-\eta)|^2$ is known as the intensity impulse response and $\tilde{H}$ is the Optical Transfer Function (OTF). There is a particularly interesting relationship between the coherent ATF and the incoherent OTF. Specifically,

$$\tilde{H} = \mathcal{F}\{H\} = \mathcal{F}\left\{|h(u-\xi, v-\eta)|^2\right\} = \tilde{h} * \tilde{h} \;, \tag{2.11}$$

where $\mathcal{F}$ is the Fourier transform and $*$ is the convolution operation. We see that the OTF is the autocorrelation of the ATF.

In either the coherent or incoherent limit, we can treat a microscope as a linear system. In the coherent case, the system is linear with respect to electric field amplitude. In the incoherent limit, the system is linear with respect to intensity. The linear system approach allows us to analyze the microscope in frequency space where real-space convolution operations are converted to frequency space multiplication (Eqs. 2.8, 2.10).

2.3 Frequency Space Analysis of Single Objective Techniques

Here we will analyze a general single objective microscopy technique in frequency space. Consider a partially coherent widefield setup (Fig. 2.3).

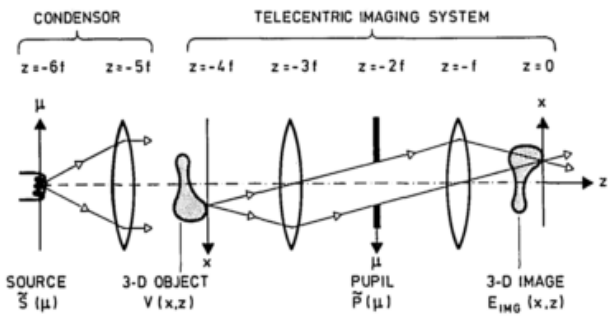

Fig. 2.3 Partially coherent widefield setup. Each point at the source produces a spherical wavefront which can be decomposed into multiple plane waves of magnitude k. Object is an elementary diffraction grating described in frequency space by $\vec{\rho}_o = [\vec{\mu}_o, \eta_0]$. The frequency space extent of the pupil determines the maximum diffracted vector accepted by the system. Figure from Streibl.[5]

Assume that the object is an elementary 3D grating described in frequency space by $\vec{\rho}_o = [\vec{\mu}_o, \eta_0]$. $\vec{\mu}_o$ is the transverse frequency component and η_0 is the axial frequency component. Consider the source as a point source producing a spherical wavefront. This wavefront can be decomposed into many superimposed plane waves. Each of these plane waves can be represented as a frequency space vector of constant magnitude, $k = 1/\lambda$. Each source vector takes the form $\vec{\rho}_s = \left[\vec{\mu}_s, \sqrt{k^2 - |\vec{\mu}_s|^2}\right]$. A source frequency vector and an object frequency vector will interact at the sample according to Bragg's law (Fig. 2.4) to produce a diffracted frequency vector.

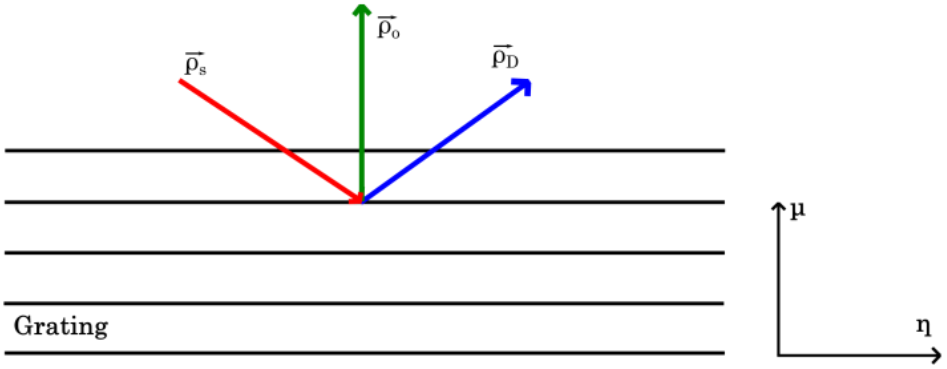

Fig. 2.4 Bragg diffraction at object. The source frequency vector adds to the frequency vector of the grating. The resultant vector is the diffracted frequency space vector. We can combine the equations for these vectors with the constraints imposed by the system, namely the finite source frequency and the finite frequency space extent of the pupil, to trace out the transfer function for the given system.

The diffracted frequency vector is

$$\vec{\rho}_D = \vec{\rho}_o + \vec{\rho}_s \ . \tag{2.12}$$

This implies that $\vec{\rho}_D = \left[\vec{\mu}_s + \vec{\mu}_o, \sqrt{k^2 - \left|\vec{\mu}_s + \vec{\mu}_o\right|^2} \right]$. Additionally, the finite frequency of the source ($\vec{\rho}_s$) and the finite extent of the system's entrance pupil ($\vec{\rho}_p$) impose constraints on $\left|\vec{\mu}_s\right|$ and $\left|\vec{\mu}_D\right|$. Gathering these constraints together with the constraints imposed by the Bragg relationship, we have the following system of equations:

$$\left|\vec{\mu}_s\right| \le \left|\vec{\rho}_s\right| \text{ and } \left|\vec{\mu}_D\right| \le \left|\vec{\rho}_p\right| \tag{2.13}$$

$$\left|\vec{\mu}_o\right| = \left|\vec{\mu}_D - \vec{\mu}_s\right| \le \left|\vec{\rho}_s\right| + \left|\vec{\rho}_p\right| = \left(1 + \frac{\left|\vec{\rho}_s\right|}{\left|\vec{\rho}_p\right|}\right)\left|\vec{\rho}_p\right| \tag{2.14}$$

$$\eta_0 = \left[\left(\lambda^{-2} - \left|\vec{\mu}_o + \vec{\mu}_s\right|^2\right)\right]^{1/2} - \left(\lambda^{-2} - \left|\vec{\mu}_s\right|^2\right)^{1/2} , \tag{2.15}$$

where the substitution $k^2 = \lambda^{-2}$ was made in Eq. 2.15. We can use these equations to trace out all of the object frequency vectors which are picked up by the system for varying degrees of illumination coherence (Fig. 2.5).

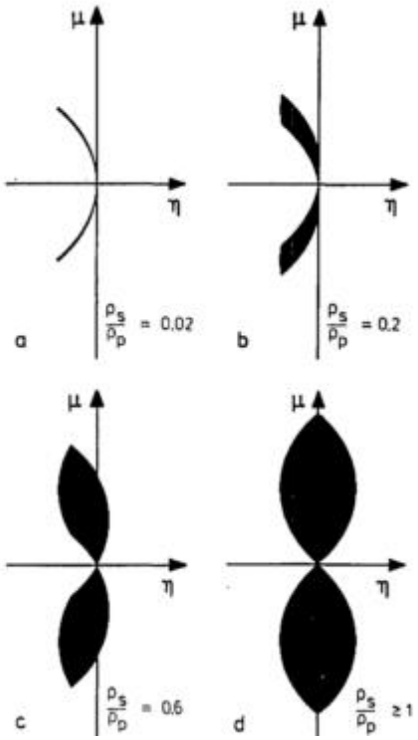

Fig. 2.5 Transfer functions for varying degrees of coherence. The degree of coherence is determined by the ratio $\left|\vec{\rho}_s\right| / \left|\vec{\rho}_p\right|$ where $\left|\vec{\rho}_s\right|$ is the source frequency vector magnitude and $\left|\vec{\rho}_p\right|$ is the frequency space extent of the entrance pupil. The limit of perfectly coherent light occurs as the ratio approaches 0. This leads to the amplitude transfer function (ATF) as shown in (a). As the ratio approaches 1, the light approaches perfect incoherence which leads to the optical transfer function (OTF) shown in (d). Figure from Streibl.[5]

These plots show all of the vectors in frequency space for which the OTF of the given system is non-zero. This is the support of the OTF. The degree of illumination coherence is determined by the ratio of the maximum illumination source lateral spatial frequency to the extent of the entrance pupil, $\left|\vec{\rho}_s\right| / \left|\vec{\rho}_p\right|$. When this quantity is approximately 0, then the illumination light is approximately coherent. From the figure we see that as the light source becomes increasingly incoherent, the system's OTF support changes shape and increases in volume (imagine rotating these 2D plots about the η axis to see

that they represent a volume). This holds up until the ratio reaches unity. This cutoff point is a result of the fact that the system's aperture cannot accept frequency vectors with a magnitude greater than the frequency extent of the aperture itself. Note that Fig. 2.5(a) shows an ATF and (d) shows an OTF. We see here graphically that the OTF is the autocorrelation of the ATF. The intensity impulse response is the inverse Fourier transform of the OTF and is the Point Spread Function (PSF). This intensity impulse response looks like Fig. 1.1. It should be noted that the term "PSF" is often used interchangeably throughout the literature to describe both the coherent PSF and the incoherent intensity impulse response.

The single objective PSF has an axial extent which is about 3 times greater than its lateral extent (Fig. 1.1). This is a direct result of the OTF in Fig. 2.5 having a much greater extent in the lateral direction than in the axial direction. The so called "missing cone" is the region of axial frequency space that is missing from the OTF at low lateral frequencies. The missing cone leads to the light fringes surrounding the central bright peak of the impulse response. Physically, this is due to the system's inability to reject out of focus light.

Of particular interest is the aperture size, $\vec{\rho}_p$. For a constant degree of coherence and increasing aperture size, the system OTF maintains its shape but grows in volume. From this, it is evident that increasing the aperture of a system is an effective way to increase the extent of its OTF support.

Increasing the aperture of the system will increase the resolution of the system. Since the OTF is the reciprocal space representation of the system impulse response (PSF), a larger OTF is equivalent to a smaller PSF. When a system has access to higher frequency information about the sample (large OTF support), it is able to resolve finer details. The aperture of a system is described by the numerical aperture, $NA = n\sin\theta$ where n is the index of refraction of the medium being imaged and θ is the semi-aperture angle. Microscope objective lenses are physically limited to a semi-aperture angle of $\pi/2$ but in reality the highest NA objectives today achieve about $0.8\times\pi/2$.

We can draw a few conclusions from the frequency space analysis above. First, in general, the resolution of a system will improve as the aperture increases. Second, we see that single objective arrangements will always be plagued by the missing cone problem due to Eq. 2.15. For low lateral object frequencies, the accepted axial frequencies will be almost zero, regardless of any other parameters. This missing cone manifests itself as fringes surrounding the PSF. These are due to the microscope's inability to reject light emitted from above and below the focal plane. This out of focus light degrades the PSF and results in large background intensity when imaging 3D samples. This makes 3D imaging particularly difficult.

2.4 Out of Focus Light and 3D Imaging

There are two popular approaches to reducing the effect of out of focus light. Computational deconvolution is a process applied most often to widefield microscopy in which out-of-focus light is computationally re-assigned to the correct position[6,7] and confocal microscopy is an approach which physically blocks out of focus light.[8]

In computational deconvolution, the focal plane is translated through the sample and images are taken at each position. The resulting stack of images is then computationally deconvolved and combined into a 3D image. The first step in computational deconvolution is characterization of the microscope's PSF.[7] Typically, this is done by first calculating the theoretically expected PSF based on the relevant parameters of the microscope (NA, wavelength of light, index of refraction just to name a few). This is helpful as a consistency check. Experimental PSF determination is necessary to account for imperfections in the microscope which theory does not account for. The PSF is experimentally determined by imaging microspheres with diameters smaller than the diffraction limit. The microspheres are imaged under conditions which approximate the imaging conditions as closely as possible. Once the PSF is determined, imaging begins. Following the Nyquist criterion, the focal plane should be translated in increments of one half the axial extent of the PSF per image. Deconvolution and

combination of the images involves solving the inverse of the convolution operation shown in Eq. 2.9. So in computational deconvolution, we know the quantities I_i and H (the measured intensity and the PSF respectively), and we want to solve Eq. 2.9 for I_o, the intensity distribution in the object space. There are many iterative techniques which solve this problem in slightly different ways. The most commonly used method, is a least-squares approach to solving Eq. 2.9 for I_o but in three dimensions instead of two.[6,7] Another group of techniques uses statistical models to relate the stack of images to the most probable distribution of point sources.[7] These techniques account for the PSF of the microscope as well as sources of noise in the imaging process, such as shot noise and background noise. Wiener deconvolution is a textbook example of one of these statistical methods. We can write Eq. 2.9 in shorthand and introduce a term which accounts for noise like so: $I_i = H \otimes I_o + n$ where n is the noise function. The Wiener deconvolution filter produces a function g such that $I_o = g \otimes I_i$. The function g has the frequency-space representation

$$\tilde{g} = \frac{\tilde{H}^* Y}{\left|\tilde{H}\right|^2 Y + Z}\ , \tag{2.16}$$

where the tilde denotes the Fourier Transform of the respective variable as usual, and $Y = \left\langle \left|\tilde{I}_0\right|^2 \right\rangle$ and $Z = \left\langle \left|\tilde{n}\right|^2 \right\rangle$ are the mean power spectral densities of I_0 and n. Eq. 2.16 can be rearranged such that

$$\tilde{g} = \frac{\tilde{H}^* Y}{\left|\tilde{H}\right|^2 Y + Z} = \frac{1}{\tilde{H}}\left(\frac{\left|\tilde{H}\right|^2}{\left|\tilde{H}\right|^2 + \frac{Z}{Y}}\right) = \frac{1}{\tilde{H}}\left(\frac{\left|\tilde{H}\right|^2}{\left|\tilde{H}\right|^2 + \frac{1}{SNR}}\right)\ , \tag{2.17}$$

where the ratio of the signal mean power spectral density to the noise mean power spectral density is called the signal to noise ratio (*SNR*), i.e. $Z / Y = SNR$. Written in this form, it is clear that the Weiner deconvolution filter attenuates frequencies which have low signal-to-noise ratios. For a high *SNR*, the transfer function is not attenuated. The net effect of this filter is that the noise contributions to the resulting reconstructed image stack are minimized.

Scanning confocal microscopy is a point-scanning technique which takes a more direct approach towards eliminating out of focus light. Rather than illuminating with a uniform plane of incoherent light like widefield microscopy, the confocal microscope uses a laser excitation source which is focused to the point to be imaged (Fig. 2.6). This illumination spot is determined by the PSF.[8] The fluorophore emission from within this illumination voxel is then imaged by the objective onto a pinhole aperture/photomultiplier detector combination. The pinhole aperture physically blocks out of focus light rays from hitting the photomultiplier. The photomultiplier then assigns an intensity value to this voxel and the system moves on to the next voxel. Once the volume is scanned, the image is created computationally using the intensity values assigned to the different voxels.

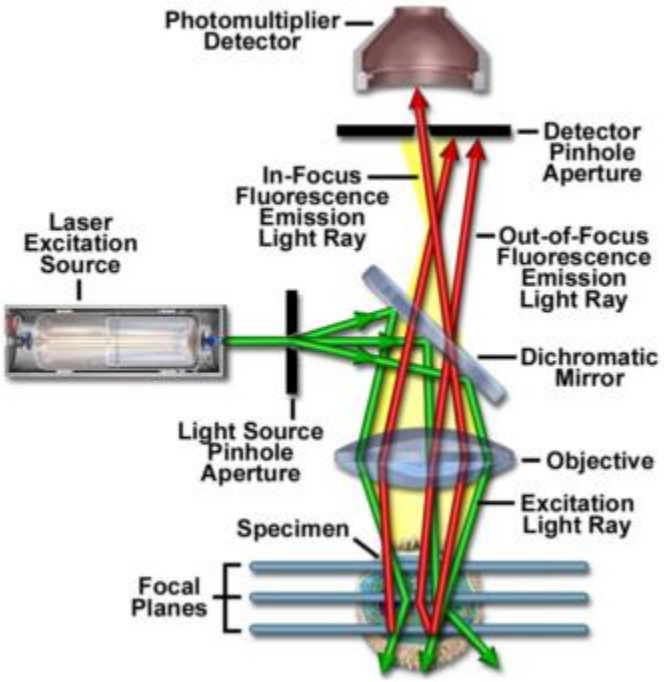

Fig. 2.6 Diagram of a scanning confocal microscope. This uses a laser excitation source instead of an extended incoherent source like widefield techniques use. The pinhole at the photomultiplier eliminates light from out of focus planes. Figure from Claxton, et al.[8]

The primary advantage of widefield techniques using computational deconvolution is that image acquisition is much faster than scanning confocal microscopy. Each focal plane image taken using a widefield technique requires many point scans in a similar confocal setup. This difference is

even more apparent in 3D imaging versus 2D imaging. Additionally, widefield microscopy has a higher signal to noise ratio than scanning confocal microscopy due to the absence of a pinhole at the detector. Scanning confocal microscopy on the other hand exhibits less photobleaching as compared to widefield because it does not illuminate the entire sample for every image. The physical elimination of out of focus light in confocal microscopy also eliminates the necessity of computational deconvolution. It should be mentioned that computational deconvolution is not exclusive to widefield techniques. Similar algorithms can be applied to the data sets created by scanning confocal microscopy.

Both widefield deconvolution microscopy and scanning confocal microscopy are attempts to eliminate out of focus light from optical sections. In widefield deconvolution, the microscope is not fundamentally different than a standard widefield microscope, so there is no change in the PSF. Confocal microscopy is fundamentally different and does have a different PSF than widefield (Fig. 2.7). The illuminating laser is focused to a point by the objective. The distribution of this illumination light will be the PSF of the objective. The effective PSF of the system is then the detection PSF multiplied with this modified excitation PSF. The result is that the effective confocal PSF is the standard widefield PSF squared ($I_i = |H|^2 \otimes I_o$). This squaring removes the sidelobes and reduces the lateral and axial extent of the confocal PSF as compared to the widefield PSF. Note that the central peak of this PSF is still anisotropic.

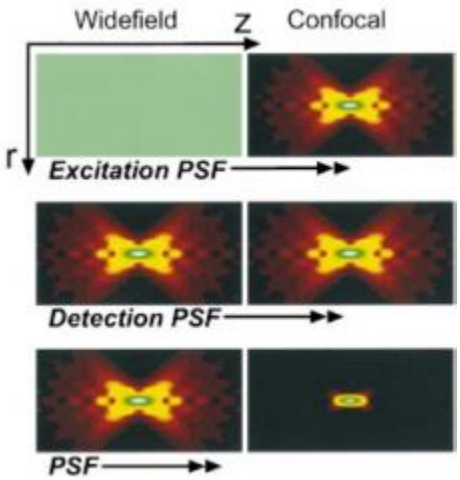

Fig. 2.7 Comparison of widefield and confocal detection, excitation and effective PSFs. The effective PSF is simply the illumination PSF multiplied by the detection PSF. Widefield illuminates with a uniform sheet of light, whereas confocal illuminates with a focused version of the excitation laser. The resulting confocal effective PSF is then the widefield PSF squared. This removes the sidelobes from the PSF and slightly reduces the extent of the central peak. Figure from Nagorni and Hell.[9]

Neither widefield deconvolution nor scanning confocal microscopy make the effective PSF more isotropic. A more isotropic PSF would allow the computational methods which underlie both techniques to achieve higher, more isotropic resolutions.

2.5 The PSF as a Measure of Performance

The PSF is used as a measure of the resolution capabilities of a microscope. Assuming a system with a circular aperture, as any microscope will have, the PSF described by Eq. 2.6 will have an Airy disk pattern in the image plane (Fig. 2.8). We rewrite Eq. 2.6 with a couple changes:

$$h(u,v;\xi,\eta)=\frac{A}{\lambda z_2}\int_{\Sigma} P(x,y)\exp\left\{-j\frac{2\pi}{\lambda z_2}[\alpha x+\beta y]\right\}dxdy \ , \tag{2.18}$$

where $\alpha=u-\xi$, $\beta=v-\eta$ and $P(x,y)$ is the transmittance function of the pupil. It was omitted originally because $P(x,y)=1$ on the entire pupil surface for a uniform circular aperture. We will convert Eq. 2.18 to cylindrical coordinates such that $f(x,y)=f(r,\theta)$ and $g(\alpha,\beta)=g(\rho,\phi)$ where r,θ are the radial and azimuthal coordinates in the pupil plane and ρ,ϕ are the radial and azimuthal

coordinates in the image plane. Also, since the pupil transmittance is circularly symmetric, we can say $P(x,y)=P(r,\theta)=P(r)$. Now,

$$h(u,v;\xi,\eta)=h(p,\phi)=\frac{A}{\lambda z_2}\int_0^a P(r)r\left(\int_0^{2\pi}\exp\left\{-j\frac{2\pi\rho r}{\lambda z_2}\left[\cos(\theta-\phi)\right]\right\}d\theta\right)dr\ , \tag{2.19}$$

where a is the radius of the pupil. Next we use the Bessel function identity,

$$\mathcal{J}_0(\chi)=\frac{1}{2\pi}\int_0^{2\pi}\exp\left[-j\chi\cos(\theta-\phi)\right]\,d\theta, \tag{2.20}$$

$$\Rightarrow h(\rho,\phi)=h(\rho)=\frac{A}{\lambda z_2}\int_0^a P(r)r2\pi\mathcal{J}_0\left(2\pi\rho r/\lambda z_2\right)dr\ , \tag{2.21}$$

where $\mathcal{J}_0$ is the 0^{th} order Bessel function of first kind. Eq. 2.21 is a 0^{th} order Hankel transform of the pupil function. A 2D Fourier Transform of a circularly symmetric function (Eq. 2.18/2.19) can be solved with a 1D Hankel transform of that same function. It can also be shown that any function separable in polar coordinates can be represented as a weighted infinite sum of Hankel transforms.[4] Rather than refer to a Hankel transform table here, we will continue with Eq. 2.21. Since $P(r)$ is a uniform circular aperture, it is unity over the entire domain of integration. We will take advantage of this and another Bessel function identity to continue:

$$\begin{aligned} &h(\rho)=\frac{A2\pi}{\lambda z_2}\int_0^a r\mathcal{J}_0\left(2\pi\rho r/\lambda z_2\right)dr \text{ and } \varepsilon \mathrm{J}_1(\varepsilon)=\int_0^{\varepsilon}\delta\mathcal{J}_0(\delta)d\delta \\ &\Rightarrow h(\rho)=\frac{A2\pi}{\lambda z_2}\left(\frac{\lambda z_2}{2\pi\rho}\right)^2\int_0^{\frac{2\pi\rho a}{\lambda z_2}} r'\mathcal{J}_0(r')dr'=\frac{Aa}{\rho}\mathcal{J}_1\left(\frac{2\pi\rho a}{\lambda z_2}\right) \end{aligned}\ , \tag{2.22}$$

where $r'=2\pi\rho r/\lambda z_2$. Eq. 2.22 can be further reduced to

$$h(\rho)=\frac{Aa\pi}{\lambda z_2 2}\frac{2\mathcal{J}_1\left(2\pi\rho a/\lambda z_2\right)}{2\pi\rho a/\lambda z_2}=C\times\frac{2\mathcal{J}_1(\chi)}{\chi}\ , \tag{2.23}$$

where $\mathcal{J}_1$ is the first order Bessel function of first kind, C absorbs constant terms and $\chi = 2\pi\rho a/\lambda z_2$. The Airy disk intensity distribution is given by $|h(\rho)|^2$. $2\mathcal{J}_1(\chi)/\chi$ is the "jinc" function or the "sombrero" function normalized so that it has value unity at the origin. To understand the effect of the numerical aperture on the width of the Airy disk, we focus on the argument of the jinc function. Note that $NA \approx n(a/z_2)$ in the paraxial case (which was already assumed in Eq. 2.6) and $\lambda_0 = n\lambda$ is the vacuum wavelength of the light. We can now write the distribution as

$$h(\rho) = C \times jinc\left(\pi \frac{2NA}{\lambda_0}\rho\right). \tag{2.24}$$

When $\rho = \lambda_0/2NA$, $h(\rho) = jinc(\pi) = .180$ and $|h(\rho)|^2 = .032$. This is essentially the first minimum of the Airy disk. This relation is called the Abbe diffraction limit. The radius of the central peak of the Airy disk is diffraction limited to $\rho = \lambda_0/2NA$. More precisely, the first minimum of the jinc function occurs at $jinc(3.8317) = 0$. This implies that $\rho = 0.61\lambda/NA$ is the more precise measure of the Airy disk radius.

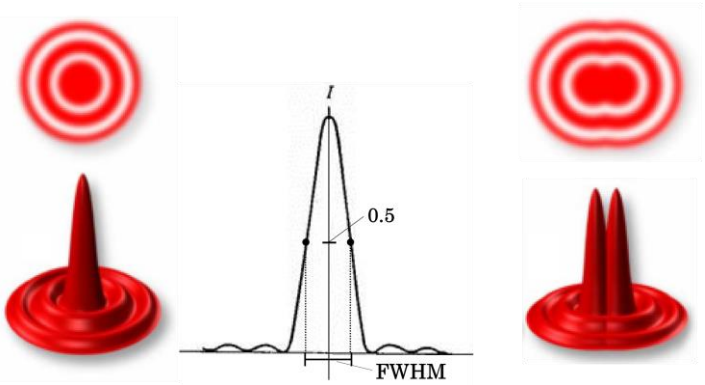

Fig. 2.8 The Airy disk pattern associated with a circular aperture and its full width at half maximum (FWHM) as well as an illustration of the Rayleigh criterion of resolution. Figure adapted from Davidson and Abramowitz.[10]

The Airy disk distribution is shown in Fig. 2.8. Notice how the pattern is point-like, but spread laterally. The size of this distribution directly determines the resolution capabilities of the system. Often

the metric of choice for describing the extent of the PSF is the full width at half maximum (FWHM). Assuming the airy disk has a maximum value of 1, the FWHM is the distance from diametrically opposed points of 0.5 relative intensity (Fig. 2.8). There are different ways to define the minimum distance which two point sources must be separated in order for the system to resolve them as distinct, but they all do it in terms of the extent of the PSF. One such example is the Rayleigh criterion which states that two points are resolved when the maximum of one overlaps the first minimum of the other; In other words, when $\rho = 0.61\lambda/NA$ as indicated in Eq. 2.24. Another such example is the somewhat vaguely defined Sparrow criterion which states that two points are resolved when the intensity between them dips below some chosen threshold. Regardless of the chosen criterion, the PSF is the fundamental quantity for measuring a system's resolution capabilities.

We see from Eq. 2.5 that the ideal PSF would be $h(u,v;\xi,\eta) = \delta(u-\xi, v-\eta)$. A PSF of this form would be able to map infinitely small points from the object space to the image space. This system would have infinite resolution – a characteristic which cannot be achieved in reality due to the diffraction limit of light. As shown above, the Abbe diffraction limit states that the minimum radius of the central peak of the Airy disk is $d = \lambda/2NA$. The diffraction limit is the physical limit to the resolution attainable by a microscope. Modern microscopes reach numerical apertures as high as 1.4. With this NA, the diffraction limit of visible light ranges from 136 nm for violet light to 268 nm for red light. This means the lateral extent of these PSFs would be 272 nm and 536 nm respectively. Note that this is the extent from one minimum to another, not to be confused with the FWHM.

A similar resolution limit exists for the axial direction. For a standard single objective arrangement, the minimum axial PSF extent is approximately $2\lambda/NA^2$. For this analysis, we can no longer use the approximation of Eqs. 2.6. These equations neglect the phase shift of a wave due to defocus (displacement from the focal plane). This approximation is valid if the system obeys the lens equation (as assumed in Eq. 2.6) or if the image space is sufficiently far enough away that the wavefront

curvature is negligible (the so-called "far field" regime). In order to describe the axial distribution of the PSF, we begin with the Fresnel approximation in its most general form:

$$h(u,v;\xi,\eta) = C \times \exp\left[j\frac{2\pi}{\lambda}\frac{\left(u^2+v^2\right)}{2z_2}\right]\iint_{\Sigma} P(x,y)\exp\left[j\frac{2\pi}{\lambda}\frac{\left(x^2+y^2\right)}{2}\left(\frac{1}{z_1}+\frac{1}{z_2}-\frac{1}{f}\right)\right]\exp\left[-j\frac{2\pi}{\lambda}\left(\alpha' x+\beta' y\right)\right]dxdy \quad (2.25).$$

Here C again absorbs constants, $\alpha' = (u/z_2) - (\xi/z_1)$, $\beta' = (v/z_2) - (\eta/z_1)$, z_1 and z_2 are the distances from object plane to first principal plane and from the second principal plane to the image plane respectively (Fig. 2.2). In order to clean up the expression, we will drop C and the first phase term. This is justified because the intensity PSF, which is what is measured by a CCD or photomultiplier tube in an actual microscope, is the magnitude squared of this function. Additionally, we make some modifications for the axial PSF analysis. We define a defocus term, $z_D = z_2 - f$. z_D is the axial displacement from the focal plane. Also, we assume that the point source is sufficiently far away from the pupil that the incident waves are plane waves. Thus, $1/z_1 = 0$. Finally, we will confine this analysis to points on the optical axis. This results in $\alpha' = \beta' = 0$. With these changes, Eq. 2.25 becomes:

$$h(u,v;\xi,\eta) = h(z_D) = \iint_{\Sigma} P(x,y)\exp\left[-j\frac{2\pi}{\lambda}\frac{\left(x^2+y^2\right)}{2}\left(\frac{z_D}{f\left(f+z_D\right)}\right)\right]dxdy. \quad (2.26)$$

Next we define the term $W' = z_D/\left[2\lambda f\left(f+z_D\right)\right]$ and convert to polar coordinates using the same convention as earlier:

$$h(z_D) = \int_0^a P(r) r \exp\left(-j2\pi W' r^2\right)\left(\int_0^{2\pi} P(r,\theta)\,d\theta\right)dr. \quad (2.27)$$

Since the pupil is circularly symmetric, the equation becomes (neglecting the factor of 2π from the integration):

$$h(z_D) = \int_0^a P(r) r \exp\left(-j2\pi W' r^2\right) dr . \tag{2.28}$$

This can be converted to a Fourier transform with the substitutions $P(r) = q(\xi)$ and $\xi = (r/a)^2 - (1/2)$. Note that $d\xi = \left(2r/a^2\right) dr$. Throughout the domain of integration, $P(r) = q(\xi) = 1$. Eq. 2.28 becomes :

$$h(z_D) = \frac{a^2}{2} \exp\left(-j2\pi W' \frac{a^2}{2}\right) \int_0^a \exp\left(-j2\pi W' a^2 \xi\right) d\xi . \tag{2.29}$$

If we again neglect constants and phase terms, the integral works out to be

$$h(z_D) = \frac{\sin\left(\pi W' a^2\right)}{\pi W' a^2} = \operatorname{sinc}\left(W' a^2\right). \tag{2.30}$$

This is the normalized sinc function which has roots at integer values of the argument. Hence, the first minimum occurs at $W' a^2 = 1$. If we define $NA = (a/f) n$, then z_D at the first minimum is

$$z_D = \frac{1}{\frac{NA^2}{2\lambda n^2} - \frac{1}{f}} \ . \tag{2.31}$$

If $f \gg \lambda$ and $n \approx 1$, as is typically the case, then $z_D \approx 2\lambda_0 / NA^2$. Comparing this to the Abbe diffraction limit, we see that the PSF will be about $4 / NA$ times larger in the axial direction than in the lateral direction. This means that with the highest numerical aperture lenses available today, the axial extent of the PSF is still about 3 times greater than its lateral extent. This anisotropy is shown in Fig 1.1.

This chapter began with a brief introduction to fluorescence microscopy and some of the basic parameters which define the performance of a microscope. This was followed with a linear systems interpretation of the microscope. Next, was a brief frequency space analysis of single objective microscopy where we discussed the limitations of single objective techniques and the relationship between the missing cone in the OTF and out of focus light. This lead into a discussion of the two primary techniques used today for 3D imaging and how they try to mitigate the effect of out of focus

light on the PSF. Finally, we took an in depth, quantitative look at the structure and extent of the lateral and axial diffraction-limited PSFs. We conclude that in order to overcome resolution anisotropy, we must depart from traditional single objective techniques. We now continue on to Chapter 3 where we review existing attempts to overcome resolution anisotropy.

Chapter 3

Literature Review

Here we review several different approaches to improving resolution isotropy. The first few sections focus on some techniques which work on achieving large *NA* s. This includes mirror based techniques which have aperture angles exceeding $\pi/2$ and a class of multiple objective techniques which combine the information from each objective either interferometrically or computationally. We finish with a review of some apodization techniques which selectively transmit high frequencies over low frequencies in the pupil plane, thereby achieving moderate resolution improvement.

3.1 Mirror Techniques

Some microscopy techniques using parabolic and elliptical mirrors with very high numerical apertures have been proposed.[11-15] Mirror based techniques are attractive because they do not suffer from chromatic aberration and they are capable of aperture angles exceeding $\pi/2$. The basic geometries of parabolic and elliptical mirrors are shown in Fig. 3.1. In theory, these techniques offer impressive resolution. These systems are capable of more isotropic diffraction-limited PSFs than lens based techniques because of their increased aperture.[12] A parabolic mirror has been used in a confocal arrangement to focus the illumination beam down to a lateral area of $0.134\lambda^2$ as compared to a minimum area of $0.16\lambda^2$ using an aplanatic objective[13] - a 17% improvement.

While mirror techniques are an interesting concept, they have one major shortcoming. Both elliptical and parabolic techniques suffer from significant coma aberration.[12] Parabolic mirrors focus incoming rays parallel to the optic axis to an interior focal point. For incoming rays which deviate

slightly from parallel, parabolic mirrors exhibit significantly more coma aberration than lens based techniques handling similar ray deviations. It has been shown that for effective confocal imaging using a parabolic mirror, the incoming parallel rays must be parallel to the optic axis within $0.006°$.[12] Elliptical mirrors have an interior and an exterior focal point. Rays emitted from either of these focal points will form an image at the conjugate focal point with little to no aberration. However, rays emitted from a position slightly displaced from a focal point will form a highly aberrated image at the position's conjugate point.

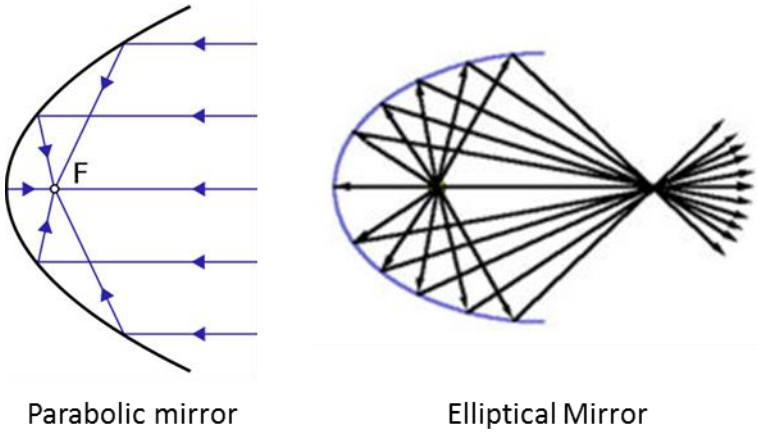

Fig. 3.1 Comparison of parabolic and elliptical mirrors. Parabolic mirrors focus incoming collimated light to the focal point, F. Elliptical mirrors focus the rays at a focal point interior to the mirror to a focal point outside of the mirror. Conversely, a point source at the exterior focal point will produce rays which are focused at the mirror's interior focal point.

Mirror techniques are best suited for investigating nanometer-sized single molecules due to their tightly confined focal point and high resolution. These same traits make mirror based techniques ill-suited for fluorescence microscopy. Their inability to handle off axis or off focal point light relegates them to point scanning techniques in which the sample is scanned. This comes with its own set of disadvantages such as increased agitation of the sample due to movement, increased imaging time and resultant photobleaching, and decreased signal to noise ratio. These disadvantages are compounded in 3D imaging due to the scaling of the amount of points in a volume versus a plane in 2D imaging.

The literature for these mirror techniques does offer an interesting observation. Fig. 3.2 compares lateral and axial slices of two different PSFs. One is from a parabolic mirror of angular aperture $\pi/2$. The other is an elliptical mirror of angular aperture $2\pi/3$. The higher aperture elliptical mirror outperforms the parabolic mirror in both the axial and the lateral direction. The biggest improvement, however, is in the axial direction. This illustrates the importance of the backward diffracted field in increasing axial resolution and creating a more isotropic PSF.

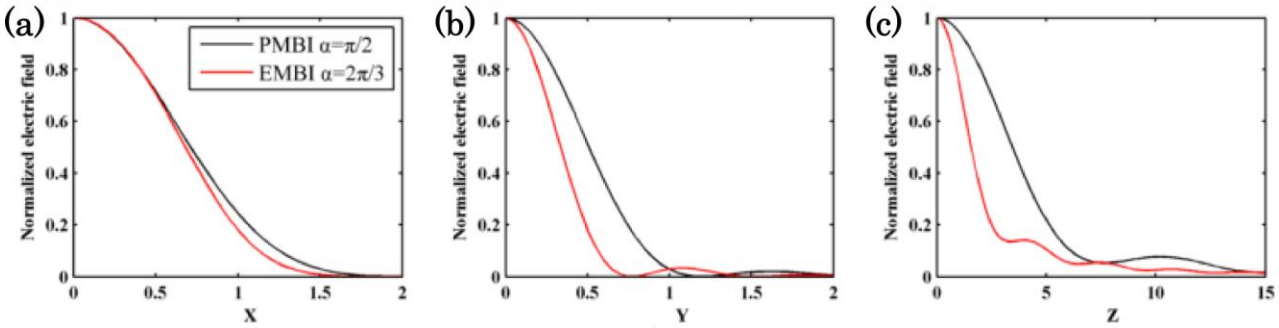

Fig. 3.2 Plots (a) and (b) compare the lateral PSF distribution for a parabolic mirror (PMBI) with angular aperture $\pi/2$ (black plot) to the PSF distribution for an elliptical mirror (EMBI) with angular aperture $2\pi/3$ (black plot). Light is polarized in the x-direction. Plot (c) compares the axial extent of the PSFs. Note that the elliptical mirror outperforms the parabolic mirror by a larger margin in the axial direction than in the lateral direction. This indicates the importance of the so-called backward diffracted field in improving axial resolution and ultimately achieving isotropic resolution. Here the axes are in units of wavelength. Figure from Liu, et al.[15]

3.2 Multiple-Objective Techniques

3.2.1 I^{5}M and 4pi Microscopy

Another approach to increasing the aperture involves two high numerical aperture, coaxial objectives. The two most prominent two-objective approaches are 4pi microscopy[9,16-19] and I^{5}M microscopy.[9,18-21] 4pi is a confocal, point-scanning method and I^{5}M is a widefield technique.

It can be shown[20] that a system's ATF is characterized by the finite acceptance angle of the aperture. We know from the linear system approach that the OTF of the system is the autocorrelation of the ATF. This is illustrated in Fig. 3.3. Note the additional lobes in the k_z direction due to the addition of a coaxial objective. This additional frequency extent leads to as much as a factor of 7

improvement of axial resolution.[21] There is no improvement in lateral resolution. Both I^{5}M and 4pi microscopy increase their effective aperture in this way.

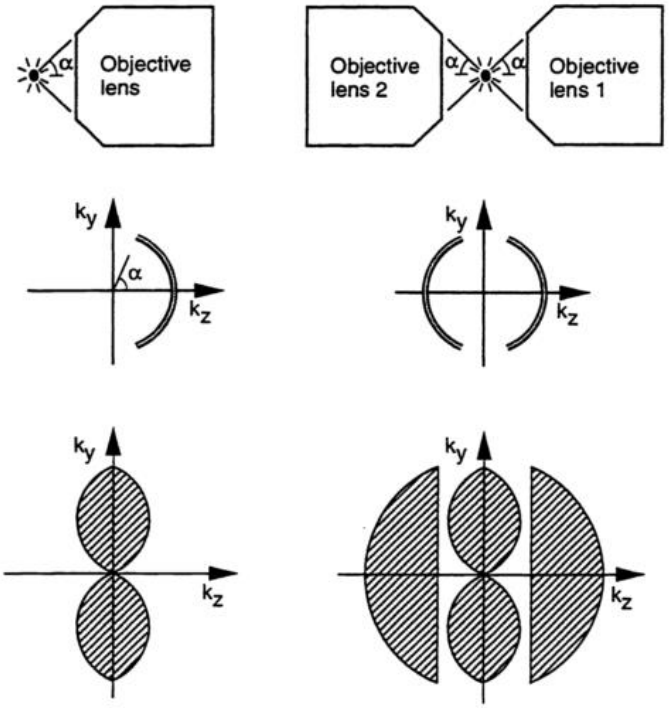

Fig. 3.3 It can be shown that the ATF of a system can be directly determined by the angular extent of that system. The OTF is then the autocorrelation of the ATF. The second row shows amplitude transfer functions corresponding to the objective arrangements above them. The bottom row shows the resulting detection OTF. Figure from Gustafsson, et al.[20]

In both I^{5}M and 4Pi microscopy, the excitation light and emission light from the two objectives are combined interferometrically in order to combine the information from both objectives and increase the effective aperture. The optical arrangement for 4pi microscopy is illustrated in Fig. 3.4. First, there is interference at the sample plane between the illumination beams. Both objectives focus the illumination laser wavefront into portions of a spherical wavefront which converge to the focal point.[16] The resulting illumination PSF is that of two counter-propagating spherical wavefronts. Every point on each wavefront has the same phase since the illumination is coherent. We can decompose each of these spherical wavefronts into many plane waves. All of the plane waves from one spherical wavefront will interfere with the plane waves of the opposite spherical wavefront anywhere they superimpose –

regardless of the angle they make with each other. The resulting illumination PSF is shown in Fig. 3.6. The axial extent of the central peak of this PSF is about a factor of 7 less than that of standard confocal or widefield techniques. Additionally, the field emanating from a point in the sample propagates through each objective back through the system. The two wavefront portions obtained by the two objectives are then interferometrically combined at the pinhole in front of the photomultiplier tube. This results in a detection PSF which is again the PSF of the interfering objective lenses. The effective 4pi PSF is then the illumination PSF multiplied with the detection PSF. This is the same as either the square of the illumination PSF or the square of the detection PSF, similar to standard confocal microscopy as discussed in Chapter 2.

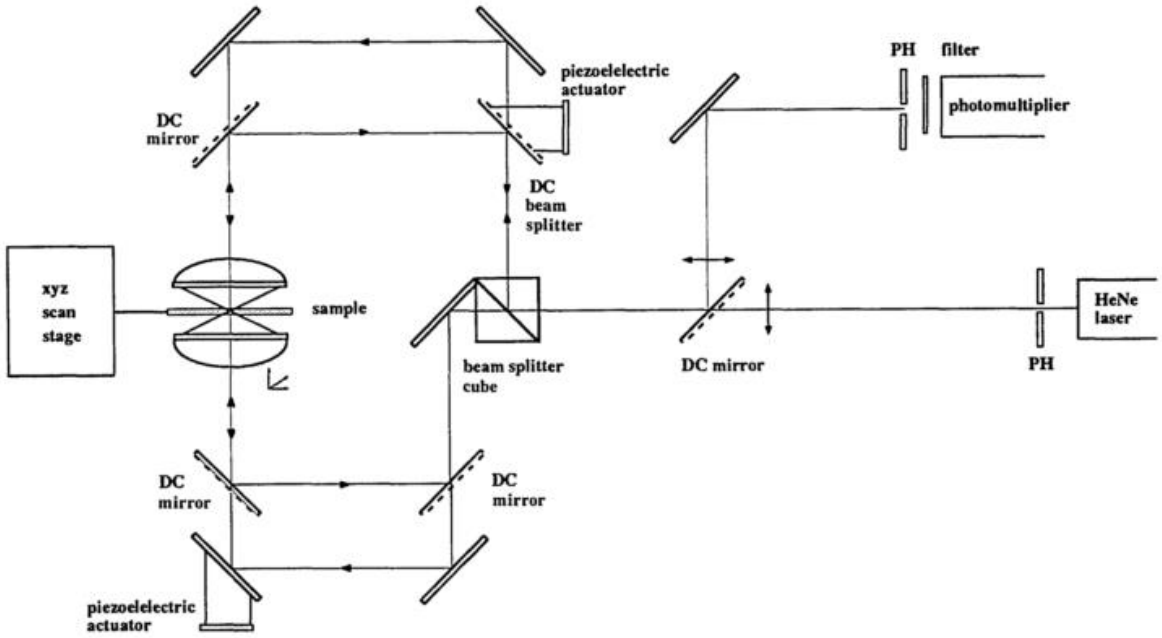

Fig. 3.4 This is the optical arrangement of a 4pi microscope. The system utilizes interferometry to increase resolution. First, there are interferometric effects about the sample space. An illuminating beam from the HeNe laser is split and then travels two equidistant paths before being focused to the same point in the sample. Due to the interference of the opposing waves, the region of intensity is significantly more confined axially than in standard confocal microscopy. A similar effect occurs when considering the detection path. Emission from a point in the sample is gathered by both objectives. The wavefronts gathered by both objectives are then interferometrically combined on the pinhole at the detector, again resulting in an interferometrically confined detection PSF. Figure from Hell and Stelzer.[16]

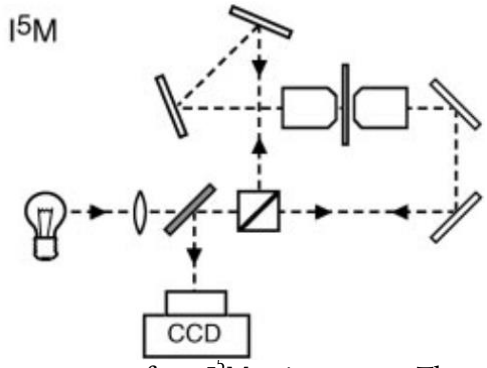

Fig. 3.5 This is the optical arrangement of an I^{5}M microscope. The microscope increases resolution through interferometry similar to 4pi. Whereas 4pi is a confocal technique, I^{5}M is a widefield technique. In I^{5}M, the illumination source is incoherent and a CCD is used in the detection path rather than a photomultiplier tube. Figure from Gustafsson, et al.[21]

I^{5}M is a widefield technique rather than a point scanning technique (Fig. 3.5). As such, illumination is performed by an extended, spatially incoherent light source without a pinhole and detection is performed by a CCD instead of a pinhole and photomultiplier combination. The detection PSF for I^{5}M is identical to that of 4pi microscopy. The illumination PSF is significantly different. The sample is illuminated with counter propagating incoherent waves. Therefore the phase relationship across any one wavefront is completely uncorrelated. These wavefronts can be decomposed into many different plane waves which all start at the aperture of the objective, but their k-vectors intersect the optical axis at different angles. Again, because the light source is incoherent, the phases of the plane waves composing a particular spherical wavefront are uncorrelated. Throughout the sample space, only perfectly counter-propagating plane waves will interfere (i.e. the plane wave from one aperture perfectly counter-propagates the equivalent plane wave from the other aperture). The result is that constructive interference occurs strongly only within approximately a depth of focus around the common focal plane of the objectives. Beyond this distance, the light intensity drops off rapidly to the incoherent sum of the intensities. As the aperture of the objectives is increased, this distance decreases. Fig. 3.6 shows the relevant PSFs for both 4pi and I^{5}M microscopy. The I^{5}M illumination PSF was calculated using the integral presented in Bewersdorf et al.[19] The 4pi illumination/detection PSF was calculated using the vectorial theory of Richards and Wolf.[22]

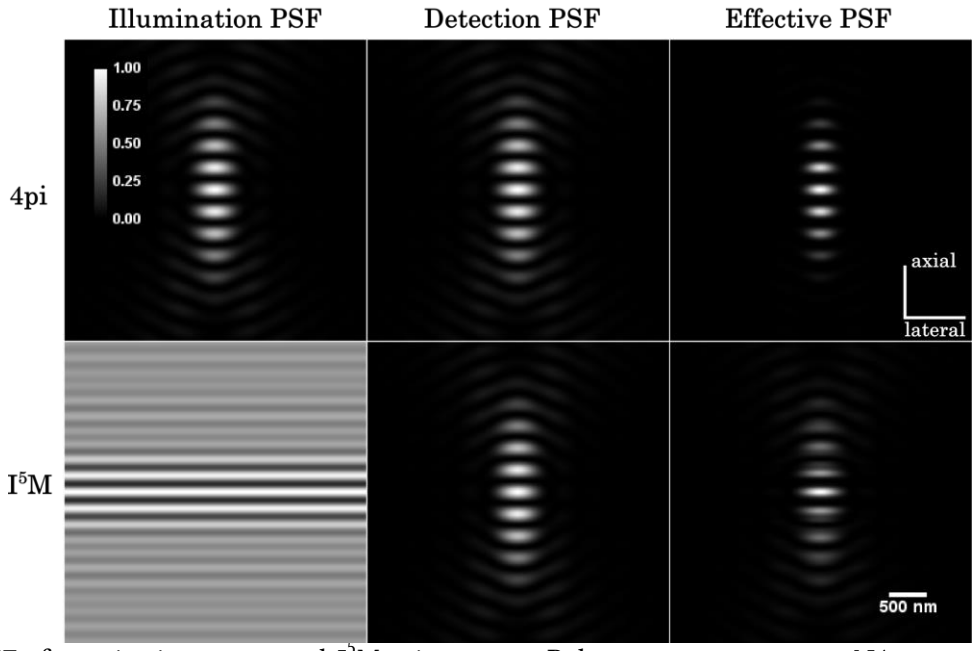

Fig. 3.6 PSFs for 4pi microscopy and I^{5}M microscopy. Relevant parameters are $NA = 0.9, \lambda = 515\ nm$. This is at a significantly lower numerical aperture than presented in the literature. This introduces substantially more lobes to the PSFs. The general behavior is still the same. Note the anisotropic central lobe in both techniques. Axial resolution is greatly improved while lateral resolution is unaffected compared to regular confocal or widefield microscopy.

4pi and I^{5}M use objective lenses with numerical apertures as high as 1.4. This maximizes the total aperture of the system but requires a very small working distance. This small working distance greatly restricts the sample volume – there is only a distance of about 300 microns between the two objectives — in which a sample can be imaged. So while two-objective techniques greatly improve axial resolution, they still suffer from resolution anisotropy and they require a very small sample volume.

3.2.2 Selective Plane Illumination Microscopy

Selective Plane Illumination Microscopy[23-27] (SPIM) is a technique which achieves optical sectioning by illuminating only in the focal plane. A cylindrical lens orthogonal to the objective creates a narrow sheet of light which illuminates only the focal plane of the objective. By doing this, the system overcomes photobleaching issues faced by standard techniques which illuminate the entire sample for each image. This efficient use of fluorescence emission allows SPIM to image deep inside sample

tissues.[26,27] The illuminating light sheet also increases SPIM's optical sectioning ability. For a 0.3 numerical aperture imaging objective, the SPIM PSF has a lateral extent of about 1.0 micron and an axial extent of microns. Compare this to the widefield PSF at this same numerical aperture which has extents of 1.0 microns and 15.17 microns in the lateral and axial directions respectively. SPIM is ultimately limited by the illuminating light sheet. For a given imaging objective, Huisken et al.[26] suggest that the thinnest part of the sheet within the field of view (fov) should be no less than 70% of the thickest part of the sheet within the fov. Say that the region which satisfies this constraint is w and t is the axial thickness within this region (Fig. 3.7). If NA is the numerical aperture of the light sheet forming cylindrical lens, then $t \propto 1/NA$ and $w \propto 1/NA^2$.[26] Thus, SPIM must compromise between strong optical sectioning and a large field of view. For a low NA objective, the axial thickness of the light sheet is less than the axial extent of the objective's PSF. This reduces the axial extent of its effective PSF as compared to widefield and confocal techniques with equivalent imaging objectives.[24] As the numerical aperture of the imaging objective increases, SPIM performs less favorably compared to other techniques at the same aperture. At about 0.8 numerical aperture, confocal microscopy outperforms SPIM axially and SPIM only reduces the regular widefield PSF by 15% in the axial direction.[24] This trend continues as the NA increases. At all numerical apertures, SPIM lateral resolution is equivalent to widefield resolution. Better resolution can be obtained by rotating the sample and taking multiple images from different angles.[27] This is, however, time consuming and not ideal. While the benefit of reduced photobleaching is constant in SPIM, it does not actually increase axial resolution for high numerical aperture imaging.

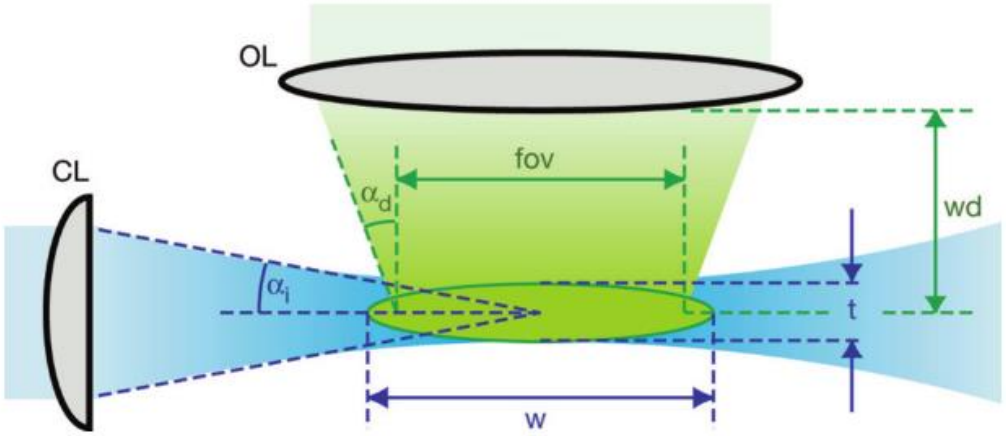

Fig. 3.7 Relationship between light sheet thickness and the field of view in SPIM. CL, cylindrical lens; $NA_{ill} = n\sin\alpha_i$; t, light sheet thickness; w, light sheet width; OL, objective lens; $NA_{\text{det}} = n\sin\alpha_d$; fov, field of view; wd, working distance. Figure from Huisken, et al.[26]

3.2.3 Multiple Imaging Axis Microscope

The Multiple Imaging Axis Microscope (MIAM)[28] is yet another approach to overcoming the anisotropy problem. It uses four objective lenses in a tetrahedral geometry with a common focal point. The sample is translated through the sample volume such that it passes through the focal plane of each objective. Each objective arm has the necessary optics and CCD to form its own image of the sample. Four widefield images are formed for each sample position. The microscope does not utilize interferometry like I^5M or 4pi. Instead, each objective forms its own, independent stack of images. Each of the four resulting image stacks must then be rotated, sheared and scaled to compensate for the objective orientations. Finally a registration step and an arithmetic or weighted average are used to combine the four stacks. This is time consuming compared to interferometric combination of the pupils of each objective. The MIAM produces a symmetric PSF, but does so at a significant cost. The necessary optics and CCDs for each of the four objective arms are expensive and the required image processing increases acquisition time.

3.3 PSF Improvement with Pupil Filters

A field of research exists which seeks to improve microscope resolution using specially designed pupil filters.[29-33] Since the exit pupil plane of the microscope objective is the Fourier transform of the focal plane, a filter in the exit pupil can modulate the degree to which different frequencies are passed through the system. The exit pupil can be filtered in such a way that some attribute of the microscope is improved. This is almost always at the expense of other attributes. For example, some filters can cause a slight narrowing of the central peak of the Airy disk at the expense of increased side-lobes.[32] Some other filters can lead to an increase in axial resolution at the expense of lateral resolution, or an improvement in lateral resolution at the expense of axial resolution.[31]

Gu et al.[29] showed that annular pupils can be used to improve axial resolution in confocal microscopy.[29] Whether or not this is possible depends on the radius of the pinhole at the detector. Calculations showed that if the radius of the pinhole, r_d, is greater than some undetermined critical value, an annular pupil produces higher axial resolution than a standard circular pupil at the same pinhole radius. This was then verified experimentally. In terms of a normalized, dimensionless radius, $v_d = \left(2\pi r_d NA\right)/\lambda$, they determined that the critical value is somewhere between $v_d = 0.65$ and $v_d = 9.87$.

It should be emphasized that axial resolution improvement due to the annular pupil is *relative* to the axial resolution of a circular pupil at that same detector pinhole radius. A circular pupil in conjunction with a pinhole radius below the critical value produces higher resolution than the annular pupil is capable of at any pinhole radius. For this reason, a confocal microscope is most often operated with the pinhole radius below the critical value. The primary reason for ever leaving this regime, i.e. widening the detection aperture, would be to increase the detection signal. However, using an annular pupil reduces detection signal because it only passes a fraction of the light that a circular pupil does. So, while the annular pupil is of theoretical interest, it offers no practical improvement in image quality.

Martinez-Corral et al. proposed a confocal microscope which modifies the detection PSF and the illumination PSF in different ways in order to achieve a more isotropic PSF.[31] They use a pupil function which improves axial resolution on either the illumination or the detection path while simultaneously using a lateral resolution improving filter on the other path. They then plot and compare a normal confocal microscopy effective PSF to the effective PSF obtained by combining the laterally and axially modified PSFs. They claim a 21% reduction of lateral PSF extent and a 34% reduction of axial extent. These results do not tell the full story. Each PSF shown is normalized to its maximum value. Here I show that their method would have a much lower signal than the normal arrangement due to the amount of light filtered by their pupil functions. Consider an objective exit pupil with a rotationally symmetric pupil function, $P(\rho)$, and a uniform intensity distribution, $I_{in}(\rho)=1$, incident upon it. The ratio of energy transmitted by the pupil to the amount of energy incident upon the pupil is a good measure of the effect of a given pupil function on the signal. In this case,

$$T=\frac{E_t}{E_i}=\frac{\int_0^1 I_{in}(\rho)P(\rho)\rho d\rho}{\int_0^1 I_{in}(\rho)\rho d\rho}=2\int_0^1 P(\rho)\rho d\rho\,, \tag{3.1}$$

where T is a measure of how much incident light the pupil function transmits. For a single circular pupil, $P(\rho)=1\Rightarrow T=1$. All light incident upon the pupil is transmitted. For a confocal setup where both the detection and illumination paths use a circular pupil, this becomes $T_1T_2=1$. Compare this to a confocal arrangement using the pupil functions chosen by Martinez-Corral et al:

$$P_1(\rho)=\rho^2\Rightarrow T_1=\frac{1}{2};\qquad P_2(\rho)=4\rho^4-4\rho^2+1\Rightarrow T_2=\frac{1}{3}. \tag{3.2}$$

Combined in the confocal arrangement, this gives $T_1T_2=0.17$. So the pupils used in their arrangement transmit only 17% of the amount of light transmitted by a regular confocal microscope. This greatly reduced signal adversely affects image quality. To compensate, you could scan each point for a longer

period of time, but this obviously increases overall image acquisition time as well as photobleaching. Additionally, the disadvantages of increased point scanning time are compounded in 3D imaging as compared to 2D imaging. Particularly in confocal microscopy which already can have signal to noise issues, the outlook for any technique which reduces signal so drastically is not favorable.

In this chapter, we have reviewed several approaches to improving resolution isotropy and reducing the effect of out of focus light. We have seen that mirror based techniques are only stigmatic at their focal points. This limits these approaches to point scanning techniques in which the sample is scanned. This approach comes with several disadvantages as we discussed. Existing multiple objective techniques also have shortcomings. I^5M and 4pi microscopy do not increase lateral resolution and they both have a very small sample volume. SPIM only offers axial resolution improvement for $NA \leq 0.8$ because of the properties of the illuminating light sheet. MIAM is slow and expensive compared to interferometry based multiple objective techniques. Finally, techniques which modify the transmission of the pupil offer theoretical resolution improvement, but they are practically useless because they greatly reduce signal strength – a particular issue for the confocal arrangements in which they are most common. Due to the shortcomings of the techniques presented in this chapter, we are motivated to pursue a new approach to improving resolution isotropy and reducing the effect of out of focus light. In the next chapter, we introduce our proposed system and the methods we will employ to quantitatively describe its performance in a confocal approach.

Chapter 4

Confocal Analysis Methods

In this chapter we will outline the methods used for analyzing the performance of a three-objective confocal microscope. Our proposed arrangement has $120°$ separation between three coplanar objectives (Fig. 4.1). Throughout the chapter, we will refer to the angular displacement between the objectives in more general terms, using the variables θ and ϕ (Fig. 4.4**)** to allow for different angular displacements between the objectives. This allows us to investigate other angular displacements which will illustrate the effect of pupil clipping, which will be introduced in this chapter. For the three-objective arrangement, we have chosen an existing objective (W N-Achroplan 63x by 0.9 M27, Carl Zeiss, Inc., Thornwood, NY) which satisfies the constraints of our system. We will use the numerical aperture, working distance and physical dimensions of this objective for various parts of the analysis in this chapter. These parameters are $NA = 0.9$, $WD = 2.4\,\text{mm}$ and the dimensions are included in the appendix (A.1).

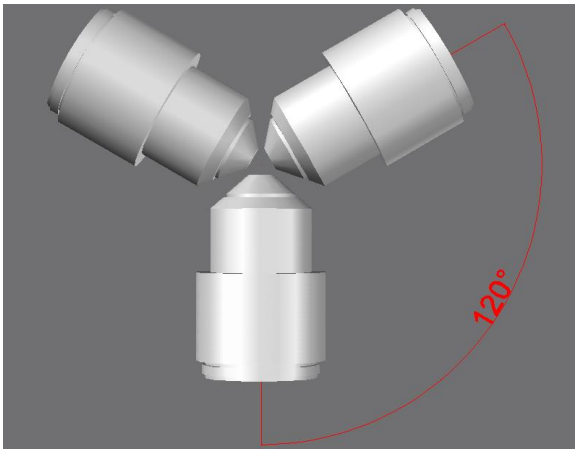

Fig. 4.1 Geometry of our proposed arrangement using the recommended objectives (W N-Achroplan 63x by 0.9 M27, Carl Zeiss, Inc., Thornwood, NY).

4.1 Confocal Illumination

4.1.1 Vectorial Method

We begin analysis of our proposed system by modeling the electric field distribution in the sample space for simultaneous coherent illumination from all three objectives. The PSF and OTF are trivially calculated from this distribution. This is the illumination PSF for the proposed system in a confocal arrangement. Contrary to single and double objective techniques, however, it does not fully describe the detection PSF for the proposed system. The reason for this is discussed in detail in the next section.

Since our system has a very high NA, a vectorial approach is necessary to precisely explain the field distribution.[34,35] As illustrated in Fig. 4.2, an incoming, linearly polarized plane wave incident on a high NA objective gains a considerable axial electric field component upon passing through the objective. The incident wave is perfectly polarized in the x-direction. The refracted wave no longer has a uniform polarization. As the NA increases, the deviation of the refracted wave polarization vector from the x-axis increases and a scalar approach becomes an increasingly poor approximation of the electric field magnitude. Additionally, scalar approximations give no information about the orientation of the electric field vector. This is also important in some applications. For example, the orientation of

the field vector relative to a fluorophore's transition dipole moment determines the rate of photon absorption of the fluorophore.

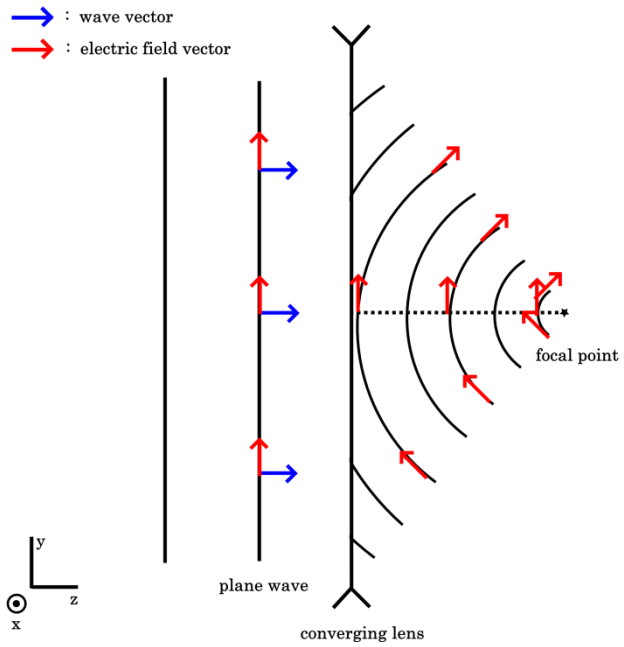

Fig. 4.2 For high NA objectives, the scalar approximation becomes increasingly inaccurate as illustrated here. Consider a point source far away from a converging lens. For the incoming plane wave, note that the electric field vector has the same magnitude and direction at all points on the wave. As the wave passes through the converging lens it is focused to the focal point. At a given point on the resulting spherical wavefront sufficiently far from the optic axis, the direction of the electric field vector differs considerably from the uniform, original direction associated with the incident plane wave. Using this simple geometrical argument, it is clear that as the numerical aperture increases (this corresponds to an increase in the angle from the focal point to the margin of the converging lens in the figure), the scalar approximation becomes increasingly poor.

To this end, we will use the well-known vectorial method of Richards and Wolf.[22] The assumptions are as follows: Assume a very distant, coaxial point source on the back side of the objective. This leads to a plane wave normally incident on the back side of the objective. This plane wave is focused to the system focal point (O) by the objective.

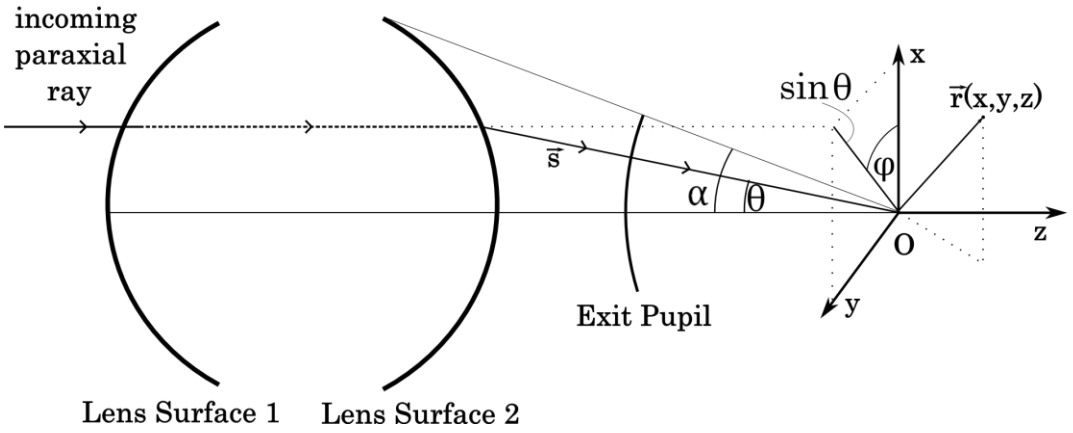

Fig. 4.3 Geometrical representation of the vectorial theory of Richards and Wolf.[22] α is the semi-angular aperture of the lens. θ and φ are the integration variables over the pupil surface. α is the semi-aperture angle. $\vec{r}$ is the vector from the origin of the coordinate system (O) to a point in image space. $\vec{s}$ is the path of a ray after refraction at the lens. All incident rays are focused to the point O. All of these rays will also be normal to the exit pupil.

The derivation of Richards and Wolf assumes incident light polarized linearly in the x-direction and a perfectly aplanatic lens. Using Fig. 4.3 as a reference, the electric field takes the following form:

$$\begin{aligned} E_x &= -\frac{iA}{\pi}\int_0^{\alpha}\int_0^{2\pi}\sqrt{\cos\theta}\sin\theta\left[\cos\theta+(1-\cos\theta)\sin^2\phi\right]\exp\left(ik\vec{r}\cdot\vec{s}\right)d\theta d\phi \\ E_y &= \frac{iA}{\pi}\int_0^{\alpha}\int_0^{2\pi}\sqrt{\cos\theta}\sin\theta(1-\cos\theta)\cos\phi\sin\phi\exp\left(ik\vec{r}\cdot\vec{s}\right)d\theta d\phi \\ E_z &= \frac{iA}{\pi}\int_0^{\alpha}\int_0^{2\pi}\sqrt{\cos\theta}\sin^2\theta\cos\phi\exp\left(ik\vec{r}\cdot\vec{s}\right)d\theta d\phi \end{aligned} \quad , \tag{4.1}$$

where E_n is the n-component of the electric field at a point $\vec{r}(x,y,z)$ in the image space. $\vec{r}$ belongs to the Cartesian coordinate system centered at the Gaussian image point, O. $A=\pi f l_0/\lambda$ where f is the system focal length and l_0 is a constant amplitude factor for rays incident on the pupil. α is the semi-aperture angle of the objective lens. $k=2\pi/\lambda$ is the wavenumber of the incident field.

The derivation of Richards and Wolf relies on an assumption that does not hold for our application. The paper follows the exact geometry and coordinate system shown in Fig. 4.3. Clearly, $\vec{r}\cdot\vec{s}=xs_x+ys_y+zs_z$. In the paper, $\vec{s}=\sin\theta\cos\phi\hat{x}+\sin\theta\sin\phi\hat{y}+\cos\theta\hat{z}$. This is not strictly true.

Following the geometry, the correct form is $\vec{s} = -\sin\theta\cos\phi\hat{x} - \sin\theta\sin\phi\hat{y} + \cos\theta\hat{z}$. The components E_x and E_y must be similarly modified. The form of Richards and Wolf is acceptable for analyzing a single objective because the single objective intensity distribution has the symmetry $\left|\vec{E}(x,y,z)\right|^2 = I(x,y,z) = I(-x,-y,z) = I(x,y,-z)$. So even though the field at a point in image space will have incorrect signs for its real and imaginary components, it isn't an issue because the magnitudes are correct and taking the intensity negates the necessity of correct signs. However, for our purposes, maintaining the correct sign relative to the coordinate system is important because we are superimposing the fields from multiple objectives. Incorrect signs will lead to incorrect PSF calculation in this situation. Thus, for our purpose, we will use a modified and more strictly correct version of the Richards and Wolf approach:

$$\begin{aligned} E_x &= \frac{iA}{\pi}\int_0^{\alpha}\int_0^{2\pi}\sqrt{\cos\theta}\sin\theta\left[\cos\theta + (1-\cos\theta)\sin^2\phi\right]\exp\left(ik\vec{r}\cdot\vec{s}\right)d\theta d\phi \\ E_y &= -\frac{iA}{\pi}\int_0^{\alpha}\int_0^{2\pi}\sqrt{\cos\theta}\sin\theta(1-\cos\theta)\cos\phi\sin\phi\exp\left(ik\vec{r}\cdot\vec{s}\right)d\theta d\phi \\ E_z &= \frac{iA}{\pi}\int_0^{\alpha}\int_0^{2\pi}\sqrt{\cos\theta}\sin^2\theta\cos\phi\exp\left(ik\vec{r}\cdot\vec{s}\right)d\theta d\phi \end{aligned}, \tag{4.2}$$

where $\vec{r}\cdot\vec{s} = -x\sin\theta\cos\phi - y\sin\theta\sin\phi + z\cos\theta$. The illumination PSF at some point (x,y,z) is then

$$PSF_{ill}(x,y,z) = \left|E_x(x,y,z)\right|^2 + \left|E_y(x,y,z)\right|^2 + \left|E_z(x,y,z)\right|^2. \tag{4.3}$$

The illumination OTF is simply the Fourier Transform of the PSF.

4.1.1 Coordinate Transforms for Three Objectives

For the three-objective arrangement, the electric field distribution from all three objectives must be superimposed before calculating the PSF. The field contribution from all of the objectives must account

for their relative positions as well. We define the "a" objective as the base objective and set its coordinates as the absolute coordinates, (x_A, y_A, z_A), for the system (Fig. 4.4).

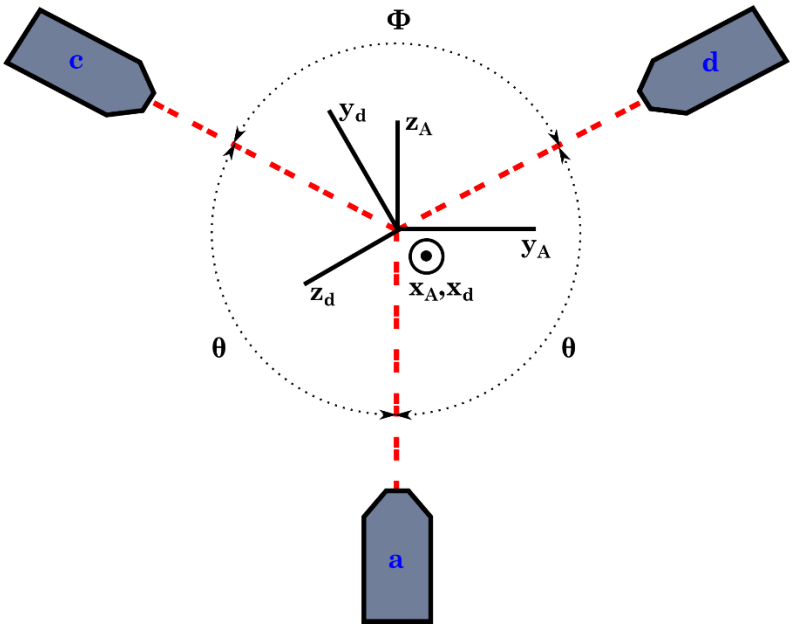

Fig. 4.4 Three-objective geometry. This illustrates the absolute coordinate system and the relative position of the d objective coordinate system. Note that $2\theta + \phi = 360°$ is always true for this arrangement.

Since the "a" objective's coordinate system and the absolute coordinate system are defined to be the same, the electric field contribution from the a objective is determined by a straightforward application of Eqs. 1. The field from objectives c and d require coordinate transformations to account for their rotations about the origin of the absolute coordinate system. Fig. 4.4 shows the absolute coordinates and the coordinate system for the d objective. The rotation is measured in the counter-clockwise direction from the base objective. So objective d is rotated θ degrees and objective c is rotated $\theta + \phi$ degrees. Note that for the three-objective geometry, $2\theta + \phi = 360°$ is always true. To determine the field at a point in the absolute coordinate system due to the d objective, $\overrightarrow{E^d}(x_A, y_A, z_A)$, the following transforms and calculations are necessary:

$$\begin{bmatrix} x_d \\ y_d \\ z_d \end{bmatrix} = \begin{bmatrix} 1 & 0 & 0 \\ 0 & \cos\theta & \sin\theta \\ 0 & -\sin\theta & \cos\theta \end{bmatrix} \begin{bmatrix} x_A \\ y_A \\ z_A \end{bmatrix} \tag{4.4}$$

$$\overrightarrow{E^d}\left(x_A, y_A, z_A\right) = \begin{bmatrix} E^d{}_{x_A} \\ E^d{}_{y_A} \\ E^d{}_{z_A} \end{bmatrix} = \begin{bmatrix} 1 & 0 & 0 \\ 0 & \cos\theta & -\sin\theta \\ 0 & \sin\theta & \cos\theta \end{bmatrix} \begin{bmatrix} E_x\left(x_d, y_d, z_d\right) \\ E_y\left(x_d, y_d, z_d\right) \\ E_z\left(x_d, y_d, z_d\right) \end{bmatrix}. \tag{4.5}$$

A similar transform occurs for the c objective, but the angle is $\theta+\phi$ instead of θ. The resulting illumination PSF is then

$$PSF_{ill}\left(x_A, y_A, z_A\right) = \left|E^a{}_{x_A} + E^c{}_{x_A} + E^d{}_{x_A}\right|^2 + \left|E^a{}_{y_A} + E^c{}_{y_A} + E^d{}_{y_A}\right|^2 + \left|E_{z_a} + E_{z_c} + E_{z_d}\right|^2 \tag{4.6}$$

The illumination OTF is again the Fourier transform of this PSF.

4.2 The Phase at Pupils

In order to employ a confocal, point-scanning technique we should quantify the relationship between a point source at an arbitrary location in sample space and the electric field distribution across the back pupil planes of the system objectives. This is important because, by quantifying these relationships, we can use deformable mirrors (DMs) or spatial light modulators (SLMs) to scan the focal points of the objectives throughout the sample space. The goal of this analysis is to quantitatively determine the phase at the back pupil plane of each objective for a given point source position and to determine how these pupils should be combined at the tube lens for imaging. We call the combination of the three pupils the “system pupil.”

The Fourier Transform relationship between the back pupil plane and the image plane lends itself to two interpretations. A qualitative, physical interpretation is that a reciprocal relationship exists between the illumination and detection paths when considering these two planes. In the illumination path, a unique field distribution in the pupil plane will focus to a unique point in image space. In the detection path, a point source at that same position will create an identical distribution across the pupil.

Thus, quantitatively describing the relationship between an arbitrary point source and the field distribution across the exit pupil is important because it allows us to manipulate the phase across the exit pupil to cause a real-space translation in the image space. This is necessary for employing a point-scanning technique.

More specifically, the field distribution across the back pupil plane is the Fourier Transform of the field distribution of the front focal plane.[4] Due to the Fourier Shift Theorem, a point source located at point $(\xi,\eta)=(a,b)$ in the image plane will have the following field distribution across the exit pupil:

$$\mathcal{F}\{A\delta(\xi-a,\eta-b)\}=Ae^{-i\frac{2\pi}{\lambda f}(ax+by)}\mathcal{F}\{\delta(\xi,\eta)\}=Ae^{-i\frac{2\pi}{\lambda f}(ax+by)}, \tag{4.7}$$

where f is the focal length of the objective. This is visually represented in Fig. 4.5. Notice that a point source at the intersection of the object plane and the optic axis, $(a=0,b=0)$, will have a uniform phase across the exit pupil.

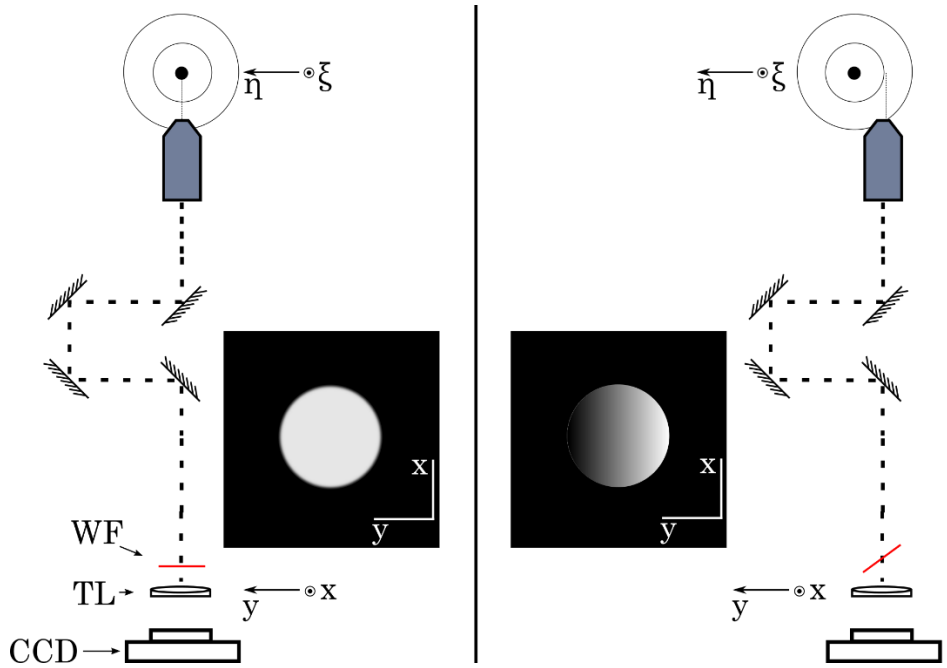

Fig. 4.5 Comparison of the phase for a perfectly centered point source and a laterally shifted point source. This is what the phase distribution across the exit pupil would look like for the two point source locations shown. A point source at the origin has a uniform phase. WF, Wavefront; TL, Tube Lens.

We can consider the Fourier transform of the object point source a decomposition of the spherical wavefront emitted by the point source into an angular spectrum of plane waves of various orientation. The phase of a particular plane wave at the exit pupil is easily determined based on the distance it travels from the point source to the entrance pupil (Fig. 4.6). The electric field at any point is simply the scalar constant field amplitude multiplied by the phase at that point. Specifically at the entrance pupil,

$$P(x,y) = A \times circ\left(\sqrt{x^2+y^2} < R_{pupil}\right) e^{ik\left(|\vec{s}|-|\vec{f}|\right)} = A \times circ\left(\sqrt{x^2+y^2} < R_{pupil}\right) e^{ik\left(|\vec{s}|-f\right)}, \tag{4.8}$$

where $\vec{f}$ is the vector from the intersection of the optic axis and the object plane to the point (x,y) on the entrance pupil. $f = \left|\vec{f}\right|$ is the front focal length of the objective, which is constant. $\vec{s}$ is the vector from the point source to the point (x,y) and k is the wavenumber of the point source emission. $circ\left(\sqrt{x^2+y^2} < R_{pupil}\right)$ constrains this relationship to the points (x,y) which are within the entrance pupil radius. $P = 0$ elsewhere.

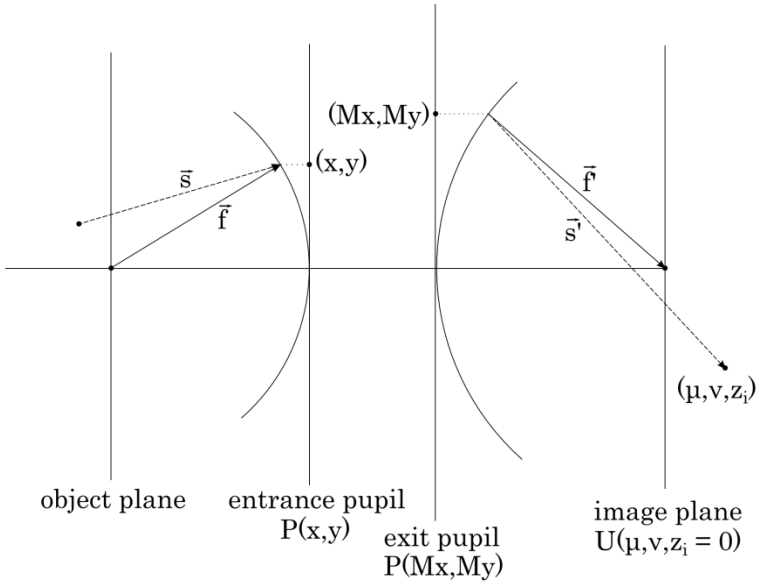

Fig. 4.6 The angular spectrum method approximates the electric field distribution across the pupil and throughout image space for a point source location. Spherical wavefronts produced by a point source are decomposed into many scalar plane waves. The field is determined by multiplying the constant, scalar field amplitude with the phase as determined geometrically in this setup. The important parameters for determining the phase at the pupil are $f = \left|\vec{f}\right|$, which is the front focal length and is constant at all points on the pupil, and $\left|\vec{s}\right|$, which is the distance from the point source to the point (x, y) on the pupil. The relationship between the entrance and exit pupils is fully described by geometrical optics. The field at a point in image space depends on the back focal length, $f' = \left|\vec{f}'\right|$, and $\left|\vec{s}'\right|$, which is the distance from point (Mx, My) on the exit pupil to the image point to be calculated. M is the magnification of the pupil.

The pupil radius is

$$R_{pupil} = \left(\frac{\alpha}{\pi/2}\right) nf \ , \tag{4.9}$$

where α is the semi-aperture angle of the objective and n is the index of refraction of the medium at the objective. It is convenient to describe the pupil radius of an objective as a fraction of the pupil for an entire hemisphere of sample space. We call nf the hemisphere radius. This value comes from $NA \times f$ with an angular aperture of $\pi/2$. The relation between the entrance and exit pupils is fully described using geometrical optics.

The resulting field distribution across the exit pupil can then be used to calculate the field distribution in image space. The field at a point in image space is

$$u(\mu,\nu,z_i)=\iint_{\Sigma}P(Mx,My)\exp\left[jk\left(|\vec{s}\,'|-|\vec{f}\,'|\right)\right]dxdy=\iint_{\Sigma}P(Mx,My)\exp\left[jk\left(|\vec{s}\,'|-f'\right)\right]dxdy \quad (4.10)$$

where $\vec{f}\,'$ is the vector from the point (Mx,My) on the exit pupil to the intersection of the optic axis and the image plane. M is the magnification of the pupil. For a single lens, $M=1$, whereas objective lenses will have magnify the pupil to some degree. $\vec{s}\,'$ is the vector from the point (Mx,My) on the exit pupil to the image point (μ,ν,z_i). $f'=|\vec{f}\,'|$ is the tube lens focal length in this case. In the physical system, the tube lens is placed at the exit pupil and focuses to the plane $u(\mu,\nu,z_i=0)$ (Fig. 4.6). Because this is a scalar approximation and our system has a high effective aperture, Eq. 4.10 is a rough approximation. It is useful in this analysis because we can use it to calculate the image field from the pupil. For the single-objective arrangement, Eq. 4.10 will directly calculate the PSF if $P(x,y)$ is the distribution due to a point source at the origin. This is not the case for the two and three-objective arrangements. A direct application of Eq. 4.10 does not account for the interferometry which occurs in these arrangements. We will discuss the consequences of this in the next section after we introduce the system pupil.

4.3 System Pupil

For the three-objective case, the three exit pupils must be combined at the tube lens in a specific way which depends on their respective objectives' orientations relative to the system focal point. We call the resulting superposition of these three pupils the system pupil. Fig. 4.7 illustrates the system pupil and how the positions of the individual objective pupils within it are determined. The sample volume is split into two hemispheres. In our computation, each hemisphere starts as an empty circular array of radius nf. The individual objective pupils are placed within this placeholder array and shifted within it. This

shift is $\delta_{pupil} = \left[(\phi/2)/(\pi/2)\right] nf$ for objectives c and d and is shown in Fig. 4.7. This is the angular displacement of the objective from a line which passes through the centers of both hemispheres and objective a. This process is done for both hemispheres and the two resulting circular arrays are superimposed to give the system pupil. The phase across each pupil is determined using the angular spectrum method shown in Fig. 4.6.

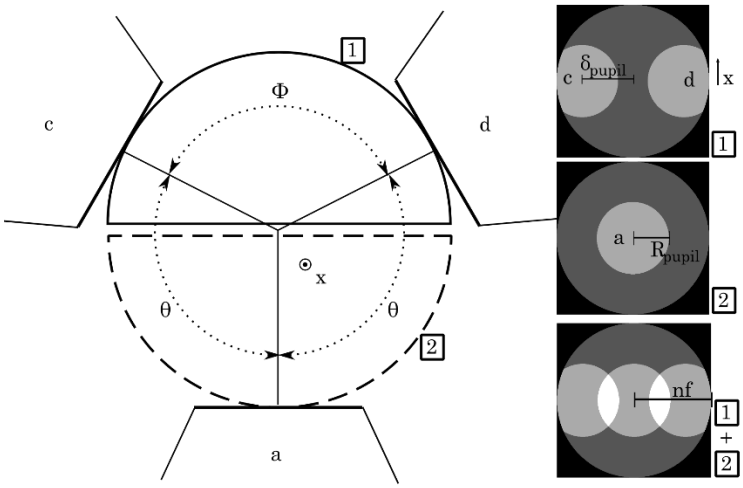

Fig. 4.7 Illustration of system pupil construction. Images correspond to a $\phi = 120°, \theta = 120°$ arrangement. The sample space is divided into two hemispheres (1 and 2). δ_{pupil} is determined by the angular displacement of the objective from the centerline relative to the dimensions of the hemisphere. R_{pupil} is Eq. 4.9 from the text. Finally, nf is the radius of each hemisphere. In the bottom inset image we see the system pupil. It is the superposition of the two hemispheres. Note the clipping of pupils c and d.

As a verification that the individual pupils within the system pupils are oriented correctly and the phase across the pupils is being calculated correctly, it is useful to calculate the PSF by using the system pupil as an intermediate step. For a multiple-objective arrangement, we cannot directly determine the confocal PSF directly from a single application of Eq. 4.10 with a point source at the object space focal point. This approach neglects the interference between the multiple objective paths which increases the effective resolution of a multiple-objective technique. Instead, the PSF is determined by iteratively moving a point source throughout the object space volume, calculating the

resulting pupil for each position (Eq. 4.8), then calculating $u(\mu=0,\nu=0,z_i=0)$ (Eq. 4.10) from each of these pupils.

Here we will look at the two-objective arrangement as the simplest example of this phenomenon. For two coaxial objectives (4pi microscope setup) and a point source at (α,β,γ), the system pupil is

$$P_2(x,y)=A\times circ\left(\sqrt{x^2+y^2}<R_{pupil}\right)e^{-ikf}\left[e^{-ik|\vec{s}_a|}+e^{-ik|\vec{s}_b|}\right], \tag{4.11}$$

where

$$\begin{aligned}|\vec{s}_a|&=\left\{[x-\alpha]^2+[y-\beta]^2+\left[\left(f^2-x^2-y^2\right)^{1/2}-\gamma\right]^2\right\}^{1/2}\\ |\vec{s}_b|&=\left\{[x-\alpha]^2+[-y+\beta]^2+\left[\left(f^2-x^2-y^2\right)^{1/2}+\gamma\right]^2\right\}^{1/2}\end{aligned}. \tag{4.12}$$

Assuming a magnification of $M=1$ (single lens), the resulting image space field distribution is

$$u(\mu,\nu,z_i)=\iint_{\Sigma}P_2(x,y)\mathrm{e}^{jk\left(|\vec{s}'|-\vec{f}'\right)}dxdy=\iint_{\Sigma}A\times circ\left(\sqrt{x^2+y^2}<R_{pupil}\right)e^{-ikf}\left[e^{-ik|\vec{s}_a|}+e^{-ik|\vec{s}_b|}\right]\mathrm{e}^{jk\left(|\vec{s}'|-\vec{f}'\right)}dxdy, \tag{4.13}$$

where constant terms have been neglected and

$$|\vec{s}'|=\left\{[u-x]^2+[v-y]^2+\left[\left(f^2-x^2-y^2\right)^{1/2}+z_i\right]^2\right\}^{1/2}. \tag{4.14}$$

The two approaches to creating the PSF are: (1) direct application in which $u(\mu,\nu,z_i)$ is determined for $(\alpha=0,\beta=0,\gamma=0)$ or (2) the iterative method in which $u(\mu=0,\nu=0,z_i=0)$ is determined for each point (α,β,γ) in the object space. Following Eq. 4.13, we see that these two approaches will yield different results. Method (2) is the correct approach because it accounts for the interference between the two objective lenses and, in a confocal microscope, it is the point $u(\mu=0,\nu=0,z_i=0)$ which is detected by the photomultiplier tube for each focal point position. While this analysis is for a two-objective arrangement, the principle holds for the three-objective arrangement

as well. For consistency, we will determine the one, two and three-objective PSFs using this same iterative approach.

4.4 Pupil Clipping

The system pupil introduces a problem which we will call clipping. In the three-objective arrangement we have discussed up until now, $\phi = 120°$ and θ=120° as shown in Fig. 4.4. This means that objectives c and d are 30° from the border of the two hemispheres (1 and 2 shown in Fig. 4.7). The 0.9 *NA* water-immersion objective which we consider has a semi-aperture angle of approximately 43°. If objectives c and d are located in hemisphere 1, this means that a portion of the c and d pupils come from hemisphere 2. Properly arranging these clipped portions onto the system pupil would be highly impractical. They would need to be isolated from their respective objective pupils and transformed using a series of mirrors and lenses on the optical table. Then they would need to be correctly positioned and superimposed onto the system pupil. This process would be quite tedious. In practice, these clipped portions would simply be discarded. Clipping is evident in the system pupil example shown in Fig. 4.7 We see that objectives c and d do not form a perfect circle within the system pupil. This lost frequency information reduces the resolution of the system. In Chapter 6 we quantify this effect with a method which we will introduce in the next section.

Another more practical way of overcoming clipping is to reduce ϕ until the entire pupils of both the c and d objectives fit within the system pupil. In practice, the minimum attainable ϕ value will depend on the dimensions of the objectives. For our chosen objectives, the optimum attainable configuration is $\phi = 98.4°$ and θ=130.8°. Assuming our chosen objectives, it is at these dimensions that the c and d objectives are in contact, as shown in Fig. 4.8.

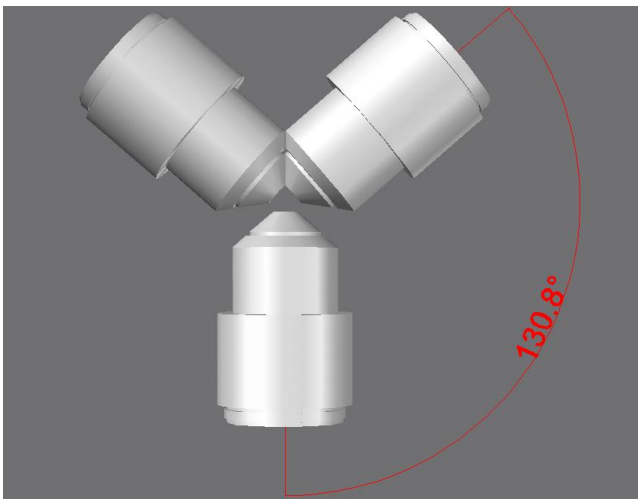

Fig. 4.8 Dimensions at which our chosen objective (W N-Achroplan 63x by 0.9 M27, Carl Zeiss, Inc., Thornwood, NY) minimizes clipping in the three-objective arrangement.

4.5 Confocal Detection

In this analysis we will take advantage of the reciprocal nature of ray optics to describe the confocal detection PSF. Originally, we interpreted the vectorial method as describing the electric field in the image space of an aplanatic lens due to a plane wave from a point source far away incident upon it in the object space. Considering this same setup, a point source in the image space will produce an identical distribution in the object space (neglecting magnification for both interpretations). Along these same lines, we can use the vectorial method to calculate the detection PSF for an objective.

In single objective and double objective (4pi) confocal techniques, the detection PSF and the illumination PSF are identical. The three-objective case is slightly different. For the detection PSF, we must account for clipping at the two pupils which overlap the hemisphere borders. To do this we will again employ the vectorial method of Richards and Wolf, but this time we must be able to perform these calculations for an asymmetrical, clipped pupil. Eqs. 4.1 allow for this. We will follow the geometry of Fig. 4.9. θ and ϕ are related to the coordinate system in the same way that they are in the original vectorial method.

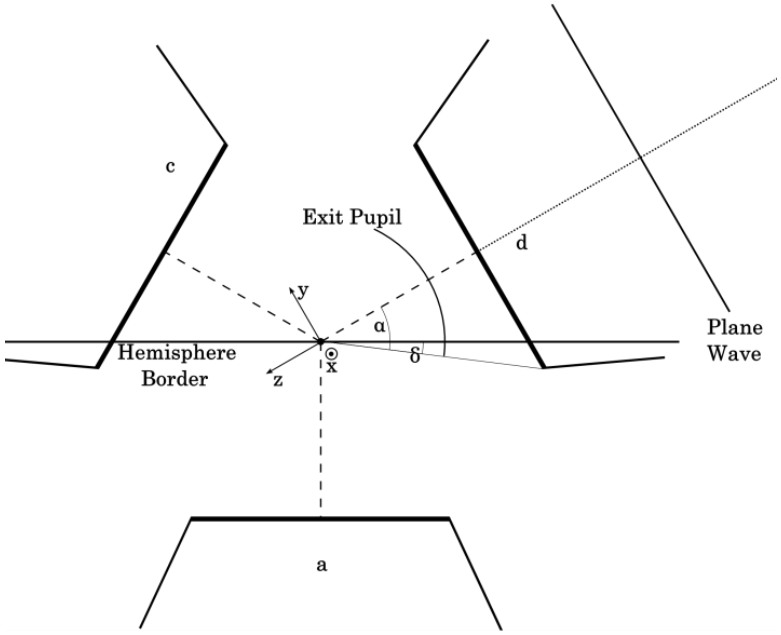

Fig. 4.9 Geometry of the clipping pupil. The pupil is labeled as the exit pupil here for consistency with the original vectorial method's interpretation of a plane wave converging to the focus. Due to the conjugate nature of optics, the result of this calculation is identical to the PSF resulting from a point source at the focus (the detection PSF).

In Eqs. 4.1, it is implicitly assumed that the exit pupil distribution is described as

$$P(\theta,\phi)=\begin{cases}1, \text{ if } 0\le\theta\le\alpha \text{ and } 0\le\phi\le 2\pi\\ 0, \text{ elsewhere}\end{cases}. \tag{4.15}$$

For the clipping pupil, the clipped portion of the objective aperture is the angle, δ (Fig. 4.9). If we define the quantity $\gamma=\alpha-\delta$ and note that $y=\sin\theta\sin\phi$, then the clipping pupil is described by

$$P_{clip}(\theta,\phi)=\begin{cases}1, \text{ if } 0\le\theta\le\alpha \text{ and } 0\le\phi\le 2\pi \text{ and } \sin\theta\sin\phi\ge-\sin\gamma\\ 0, \text{ elsewhere}\end{cases}. \tag{4.16}$$

Now Eqs. 1 take the following form for the clipping case:

$$\begin{aligned}
E_x &= -\frac{iA}{\pi}\int_0^{\alpha}\int_0^{2\pi} P_{clip}(\theta,\phi)\sqrt{\cos\theta}\sin\theta\left[\cos\theta+(1-\cos\theta)\sin^2\phi\right]\exp\left(ik\vec{r}\cdot\vec{s}\right)d\theta d\phi\\
E_y &= \frac{iA}{\pi}\int_0^{\alpha}\int_0^{2\pi} P_{clip}(\theta,\phi)\sqrt{\cos\theta}\sin\theta(1-\cos\theta)\cos\phi\sin\phi\exp\left(ik\vec{r}\cdot\vec{s}\right)d\theta d\phi\\
E_z &= \frac{iA}{\pi}\int_0^{\alpha}\int_0^{2\pi} P_{clip}(\theta,\phi)\sqrt{\cos\theta}\sin^2\theta\cos\phi\exp\left(ik\vec{r}\cdot\vec{s}\right)d\theta d\phi
\end{aligned}. \tag{4.17}$$

Using these equations we can describe the confocal detection PSF. The confocal detection PSF must again account for the relative positions of the three objectives using the transforms (Eqs. 4.4, 4.5) described in the first section of this chapter.

In this chapter we introduced the geometry of the three-objective arrangement and the mathematical framework which we will use to analyze its performance and compare it to single and double-objective confocal techniques. The confocal illumination PSF, the confocal detection PSF and the pupil phases from the angular spectrum method fully describe the primary quantities of interest of our three-objective arrangement employed in a confocal technique. This data is presented in Chapter 6. In the next chapter, we will introduce a similar framework for analyzing the proposed arrangement employed in a widefield technique.

Chapter 5

Widefield Analysis Methods

In this chapter we will outline the methods used for analyzing the performance of a three-objective widefield microscope. Our proposed arrangement has 120° separation between three coplanar objectives (Fig. 5.1). For the three-objective arrangement, we have chosen an existing objective (W N-Achroplan 63x by 0.9 M27, Carl Zeiss, Inc., Thornwood, NY) which satisfies the constraints of our system. We will use the numerical aperture, working distance and physical dimensions of this objective for various parts of the analysis in this chapter. These parameters are $NA = 0.9$, $WD = 2.4$ mm and the dimensions are included in A.1.

5.1 Widefield Illumination

The widefield illumination PSF for the three-objective arrangement is undetermined at this time. For single-objective microscopy using Köhler illumination, the illumination PSF is uniform throughout sample space and offers no resolution enhancement. For this type of illumination, the microscope's effective PSF is equivalent to its detection PSF. In I^5M microscopy, interference effects at the focal plane give an illumination which greatly improves axial resolution but has no effect on lateral resolution (Fig. 3.6). Similar interference effects would be present in the three-objective widefield illumination PSF, but the calculation of this distribution is not as straightforward as the I^5M illumination because the objectives are not perfectly normal to each other in this arrangement. Certainly the three-objective PSF would have some structure due to interference effects which, when multiplied with the detection PSF,

would improve the isotropy of the effective PSF. A quantitative description of this distribution is yet a work in progress.

5.2 Widefield Detection

Here we investigate the widefield detection PSF in the three-objective arrangement. The widefield technique combines entire planes of light rather than single points from each objective. In the case of I^5M microscopy, this is a straightforward problem to solve- the two objectives have perfectly overlapping focal planes. For our proposed three-objective arrangement, however, the focal planes of each objective do not overlap. This is illustrated in Fig. 5.1.

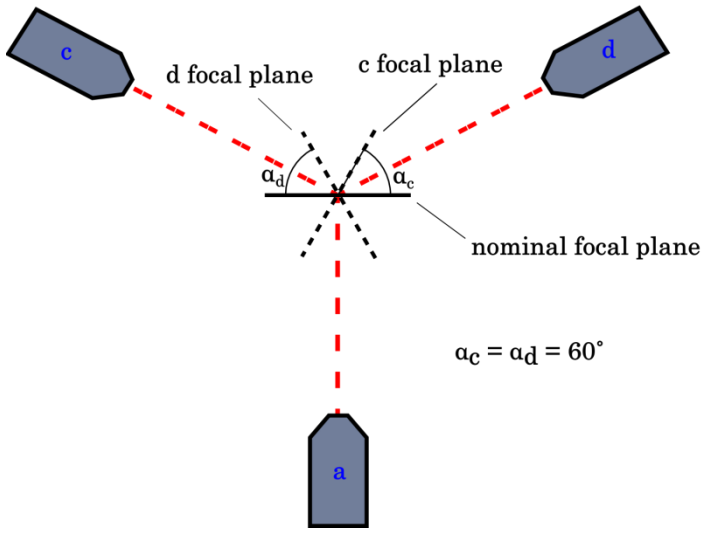

Fig. 5.1 Non-overlapping focal planes of the proposed arrangement. This example has $\theta = \phi = 120°$. We take the focal plane of the a objective as the system focal plane. This is the plane that is imaged by the widefield setup. Note that the focal planes for the c and d objectives are oblique to the nominal focal plane by angles of α_c and α_d respectively. These are both $60°$ for this arrangement.

5.2.1 Oblique Plane Microscopy

A technique called oblique plane microscopy (OPM) gives insight into how to overcome the oblique imaging problem. OPM is a relatively new microscopy technique which images planes that are oblique to an objective's nominal focal plane.[36] The technique illuminates an oblique focal plane and images that same oblique plane along the same optical path. The setup for OPM is shown in Fig. 5.2.

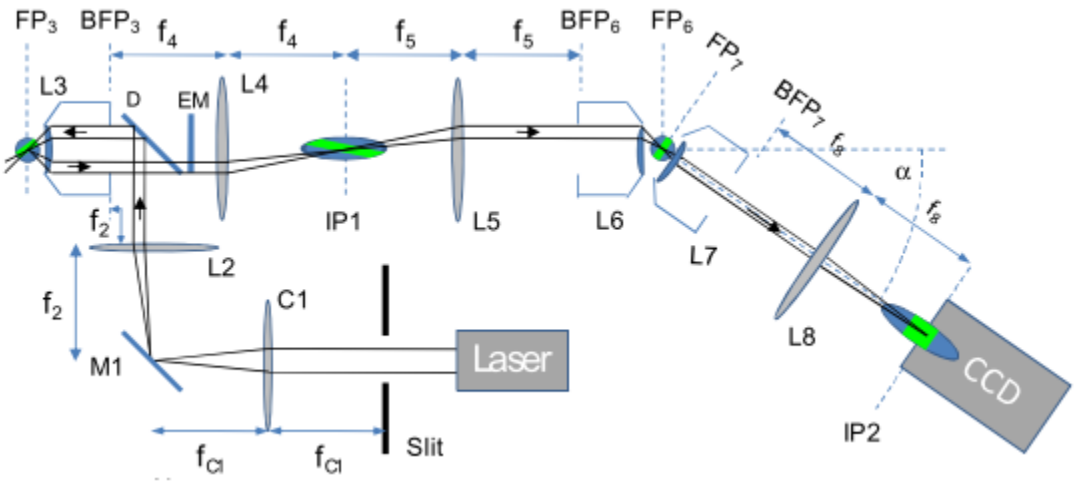

Fig. 5.2 Oblique plane microscopy setup. M, mirror; L, spherical lens; C, cylindrical lens; f_i, focal length of lens i; FP_i, focal plane of lens i; BFP_i, back focal plane of lens I; D, dichroic filter; EM, emission filter; IP, imaging plane for CCD. Figure from Dunsby.[36]

OPM requires a total of three objectives in series to image the oblique plane. Referencing Fig. 5.2, objective L3 illuminates with an oblique light sheet and simultaneously detects. Here we are only concerned with the detection path of OPM and will neglect the specifics of oblique illumination. The detection path from the object through to FP_6 lends itself to two identical interpretations. First, L3 and L4 form an infinity corrected microscope. Lateral magnification at IP1 is M, but axial magnification of points about IP1 goes as M^2. L5 and L6 form a second infinity-corrected microscope which undoes this asymmetric magnification and produces an isotropic image between L6 and L7. Alternatively, the exit pupil of L3 is transferred to the nominal exit pupil (now entrance pupil since the microscope is reversed) of L6 by a 4f system which comprises L4 and L5. In either interpretation, the goal is for all image points between L6 and L7 to be stigmatic- all of the aberrations in the image at IP1 are to be removed. By definition, this means that the system comprising L3, L4, L5 and L6 is a perfect imaging system. This allows L7 and L8 to be translated through the isotropic image at FP6. In OPM, they are oriented such that they image the oblique illumination plane through the object at FP_3.

We can use OPM to enable widefield imaging with our three-objective arrangement. If we use an OPM setup for the “c” and “d” objectives, we can image the system focal plane with all three

objectives in the three-objective arrangement – the necessary condition for a widefield microscope. The primary component of the OPM is the perfect imaging system which eliminates aberrations in the image of the oblique plane. For the three-objective arrangement in widefield, we would need to create perfect imaging systems along the "c" and "d" objective arms. This imposes magnification constraints on the lenses and objective which follows the detection objective. In the next section we discuss the properties of a perfect imaging system and these constraints in more detail.

5.2.2 Perfect Imaging System

In a perfect imaging system, any point object forms a stigmatic point image. Fig. 5.3(a) is an example of a perfect imaging system. It has been shown[37] that a perfect imaging system requires that $|M| = n_1/n_2$ where M is the system magnification and n_1 and n_2 are the object space and image space indices of refraction respectively. This in turn implies that $\gamma_1 = \pm\gamma_2$ where γ_1 is the angle the ray going from the object point into the system makes with the optic axis and γ_2 is the angle that same ray makes with the optic axis at the image. This is also evident in the top diagram of Fig. 5.3(a).

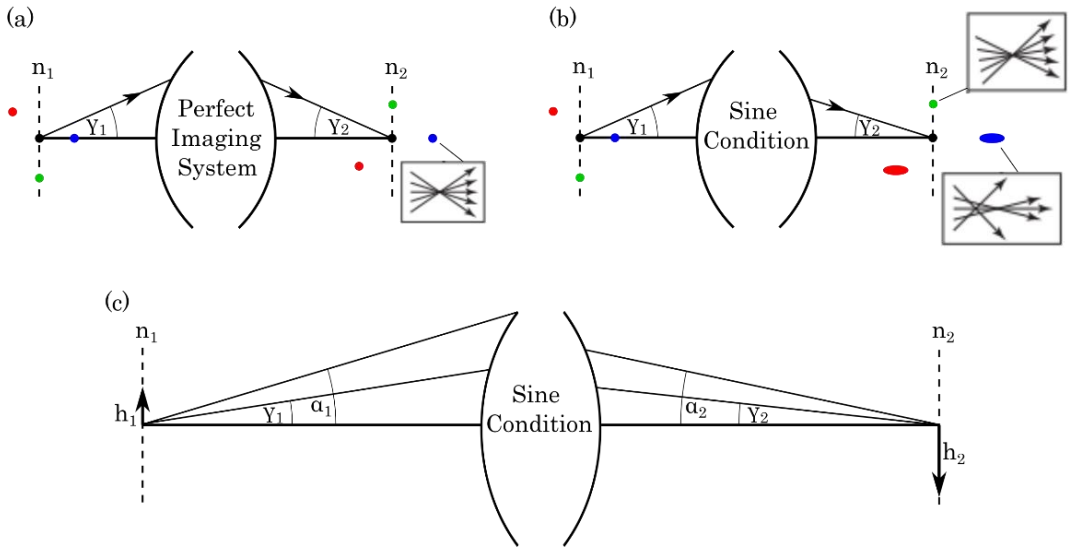

Fig. 5.3 (a) Example of a perfect imaging system. Note how each object point forms a stigmatic image point. (b) Example of an imaging system which obeys the sine condition. Object points in the focal plane form stigmatic images, but object points axially displaced from the focal plane form spherically aberrated images. (c) Imaging system which obeys the sine condition. This illustrates the mathematical implications of the sine condition and the Lagrange invariant.

Microscopes necessarily break the magnification constraint on a perfect imaging system. Most microscopes today obey the Abbe sine condition. Therefore we should explore how to convert a microscope which obeys the sine condition into a perfect imaging system. Qualitatively, the sine condition means that object points in the focal plane are stigmatically imaged at the image space focal plane at great magnification. The tradeoff for this magnification is that object points axially displaced from the focal plane suffer from strong spherical aberration. This is shown Fig. 5.3(b). Note the manner in which the rays converge for images on and off the axis. The ray pattern for the blue point is characteristic of spherical aberration.

Fig. 5.3(c) gives more insight into the sine condition as well as the Lagrange invariant. With respect to this diagram, the sine condition states

$$\frac{\sin\gamma_2}{\sin\gamma_1} = \frac{\sin\alpha_2}{\sin\alpha_1}\ , \tag{5.1}$$

where α_1 is the semi-aperture angle in this case. This relation holds for *any* two rays produced by the same point and passing through the system however. This diagram also highlights another important

relationship. The Lagrange invariant is a fundamental law of optics which states that the product of the ray angle and image height from the optical axis is a constant of the system, or invariant. Specifically,

$$n_1 h_1 \alpha_1 = n_2 h_2 \alpha_2 , \tag{5.2}$$

where h_1 and h_2 are the object height and image height respectively. Combining Eqs. 5.1 and 5.2, we can say

$$\frac{\sin\gamma_2}{\sin\gamma_1} = \frac{\sin\left(\frac{n_1}{n_2}\frac{h_1}{h_2}\alpha_1\right)}{\sin\alpha_1} \approx \frac{n_1}{n_2}\frac{1}{M} \Rightarrow \sin\gamma_2 = \frac{n_1}{n_2}\frac{\sin\gamma_1}{M} , \tag{5.3}$$

where $M = h_2/h_1$ is the magnification of the system. From Eq. 5.3, it is clear that the system can be a perfect imaging system if and only if $M = n_1/n_2$.

There is an alternative and more thorough interpretation of this perfect imaging system. It can be shown with a quick geometrical argument[38] that the phase across the exit pupil of an objective is

$$\psi\left(\rho,\varphi;\vec{r}\right) \approx nk\sin\alpha\left[x\rho\cos\varphi + y\rho\sin\varphi + z\sqrt{\frac{1}{\sin^2\alpha} - \rho^2}\right] , \tag{5.4}$$

where n is the index of refraction, k is the wavenumber, α is the semi-angular aperture of the objective, x, y and z are the coordinates of a point object, ϕ is the azimuthal angle in the pupil plane, defined in the usual way in terms of the Cartesian coordinates, and ρ is the radial coordinate of the pupil plane normalized to the pupil radius angular aperture of the objective (i.e. $0 \le \rho \le 1$). The remote focusing technique takes advantage of the conjugate nature of optics by relaying this same pupil distribution from the exit pupil of the first objective to the nominal exit pupil (now entrance pupil) of the second objective via the 4f imaging system between them (L4 and L5 in Fig. 5.2). The constraint here is on the 4f system. It must relay the pupil with no magnification. This then forms a point image with the same displacement as the point object.

5.2.3 Modified Oblique Plane Microscopy and its PSF

The three-objective arrangement will use a modified version of the OPM presented in the prior sections. The perfect imaging system is present in this modified version, just as in the OPM arrangement discussed earlier. Here, however, instead of an additional objective arm to image the remote object created by the perfect imaging system, a mirror is tilted such that the rays coming from the oblique plane in the object space pass back through the objective and are imaged onto the CCD by L3 in Fig. 5.4(a). This method of OPM is more economical than the original one because it only requires two objectives instead of 3. For our three-objective arrangement, we will assume that the “c” and “d” (Fig. 5.1) objectives image the oblique focal plane using this setup.

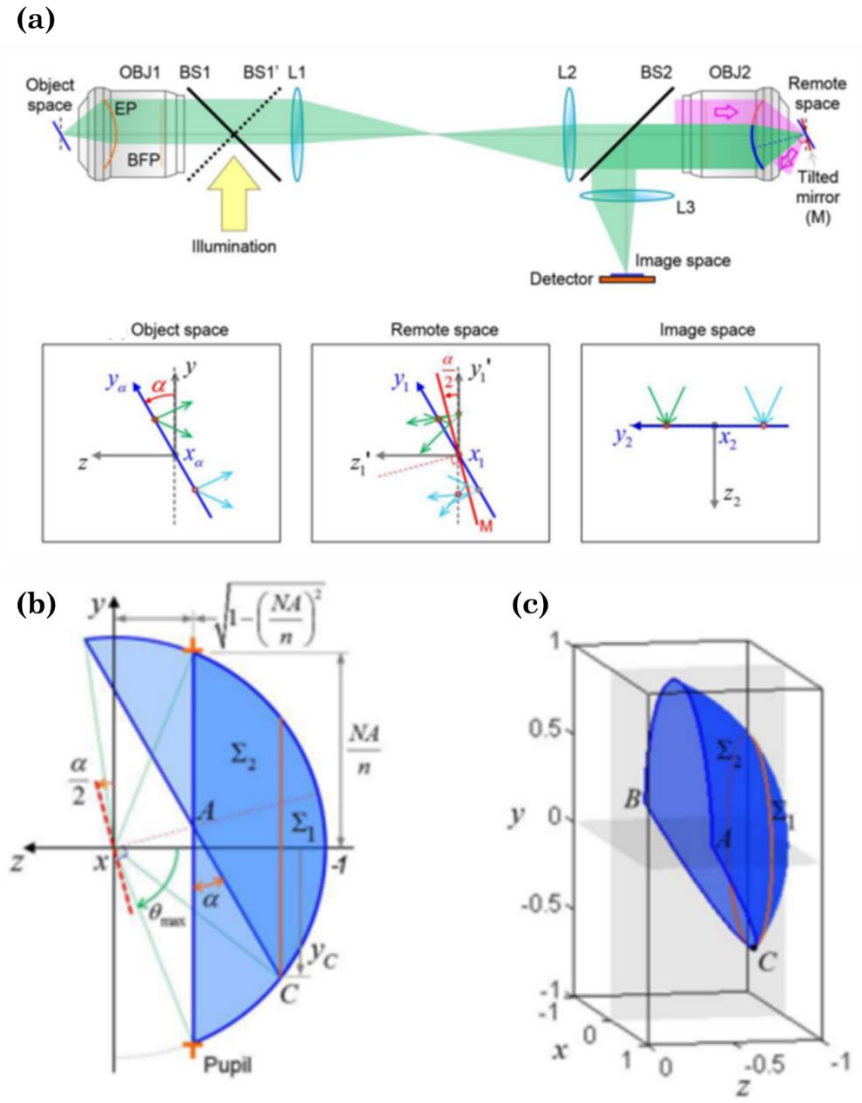

Fig 5.4 (a) OPM setup using two objectives and a tilted mirror rather than three objectives. Note the light clipping at OBJ2 due to reflection off of the tilted mirror. The PSF for imaging an oblique plane can be modeled using the vectorial method of Richards and Wolf for an arbitrary pupil by accounting for the shape of this pupil. (b) This figure leads to the geometrical derivation of the pupil for an oblique plane of angle α (c) 3D representation of the effective pupil. Note that the pupil is divided into Σ_1 (a circularly symmetric portion) and Σ_2 (the remaining asymmetrical portion). Figure from Kim, et al.[39]

Kim et. al[39] were the first to accurately describe the PSF for this type of OPM. In Fig. 5.4(a) we see that, for a focal plane which is rotated relative to the nominal focal plane, the pupil at OBJ2 is clipped. In the paper, they geometrically derive the effective pupil function for an oblique plane of angle α (Fig. 5.4(b)). The pupil is divided into two portions: Σ_1 is a circularly symmetric portion and Σ_2 is the remainder (Fig. 5.4(c)). The resulting pupil function is

$$P(\theta,\phi) = P_{\Sigma_1}(\theta,\phi) + P_{\Sigma_2}(\theta,\phi) \ , \tag{5.5}$$

where

$$\begin{aligned} P_{\Sigma_1}(\theta,\phi) &= \begin{cases} 1, \text{ if } 0 \le \theta \le \theta_C \text{ and } 0 \le \phi \le 2\pi \text{ and } y_C < 0 \\ 0, \text{ elsewhere} \end{cases} \\ P_{\Sigma_2}(\theta,\phi) &= \begin{cases} 1, \text{ if } \theta_C \le \theta \le \theta_{\max} \text{ and } \phi_1(\theta) \le \phi \le \phi_2(\theta) \\ 0, \text{ elsewhere} \end{cases} \end{aligned} \ . \tag{5.6}$$

The parameters for the piecewise functions are determined from the geometry to be:

$$(x_C, y_C, z_C) = \left(0, -\frac{NA}{n}\cos\alpha + \sqrt{1-\left(\frac{NA}{n}\right)^2}\sin\alpha, -\frac{NA}{n}\sin\alpha - \sqrt{1-\left(\frac{NA}{n}\right)^2}\cos\alpha \right) \tag{5.7}$$

$$\theta_C = \cos^{-1}|z_C| \tag{5.8}$$

$$\theta_{\max} = \sin^{-1}\left(\frac{NA}{n}\right) \tag{5.9}$$

$$\phi_1(\theta) = \sin^{-1}\left(\frac{y}{\sin\theta}\right)\Bigg|_{y = z\cot\alpha + \frac{\sqrt{1-(NA/n)^2}}{\sin\alpha}} \tag{5.10}$$

$$\phi_2(\theta) = \pi - \phi_1(\theta) \ . \tag{5.11}$$

The electric field distribution resulting from imaging the oblique plane is then determined by plugging Eq. 5.5 into the vectorial method of Richards and Wolf (Eqs. 4.1).

This derivation for the OPM PSF only allows for $0 \le \alpha \le \pi/2$ where α is the angle between the nominal focal plane and the oblique plane as defined in Fig. 5.4(a). In the three-objective arrangement, this form works for describing the d objective, but not the c objective. We must create a modified version that will accept $-\pi/2 \le \alpha \le 0$ in order to describe the field from the c objective and simultaneously maintain our coordinate system. To do this, modifications must be made to Eqs. 5.6, 5.7, 5.10 and 5.11. For the negative rotation, these become:

$$\begin{aligned} P_{\Sigma_1}(\theta,\phi) &= \begin{cases} 1, \text{ if } 0 \le \theta \le \theta_C \text{ and } 0 \le \phi \le 2\pi \text{ and } y_C > 0 \\ 0, \text{ elsewhere} \end{cases} \\ P_{\Sigma_2}(\theta,\phi) &= \begin{cases} 1, \text{ if } \theta_C \le \theta \le \theta_{\max} \text{ and } \phi_1(\theta) \le \phi \le \phi_2(\theta) \\ 0, \text{ elsewhere} \end{cases} \end{aligned} \tag{5.12}$$

$$\left(x_C, y_C, z_C\right) = \left(0, \frac{NA}{n}\cos\alpha - \sqrt{1-\left(\frac{NA}{n}\right)^2}\sin\alpha, -\frac{NA}{n}\sin\alpha - \sqrt{1-\left(\frac{NA}{n}\right)^2}\cos\alpha \right) \tag{5.13}$$

$$\phi_1\left(\theta\right) = \pi - \sin^{-1}\left(\frac{y}{\sin\theta}\right)\Bigg|_{y=-z\cot\alpha-\frac{\sqrt{1-\left(NA/n\right)^2}}{\sin\alpha}} \tag{5.14}$$

$$\phi_2\left(\theta\right) = 3\pi - \phi_1\left(\theta\right) \ . \tag{5.15}$$

For the three-objective case, the same transformations covered in the confocal illumination case (Eqs. 4.4 and 4.5) are again applied to account for the rotations of the three objectives relative to the origin of the absolute coordinate system.

In this chapter we introduced the mathematical framework for analyzing the proposed three-objective arrangement operated in a widefield technique. We are able to describe the single and double objective widefield illumination PSFs, but at this time we are unable to quantitatively describe the three-objective widefield illumination PSF. The widefield detection path of the three-objective arrangement utilizes a technique called oblique plane microscopy (OPM) which allows the "c" and "d" objectives to image the system focal plane. A key component of OPM is the formation of a perfect imaging system. This was discussed in detail in this chapter. We use a modified version of the OPM PSF calculations derived by Kim et al.[39] to describe the three-objective detection PSF. Now we proceed to Chapter 6, in which we present the quantitative analysis of the three-objective arrangement in both a confocal and a widefield arrangement.

Chapter 6

Results

In this chapter we use the methods outlined in Chapters 4 and 5 to quantitatively describe the performance of the proposed system and compare it to existing single and double objective techniques. The chapter is divided into two sections. Section 6.1 describes the three-objective arrangement in a confocal microscope. We show the illumination, detection and effective PSFs and OTFs for confocal arrangements of one, two and three objectives. In Section 6.2, we show what the phase at each of the pupils of the three-objective arrangement looks like for various point source positions throughout the sample space. Section 6.3 describes the proposed arrangement in a widefield setup. For the three-objective arrangement, we show only the detection PSF and OTF. Illumination, detection and effective PSFs and OTFs for one and two-objective widefield arrangements are shown in Section 6.3.

Fig. 6.1 shows the geometry of the one, two and three- objective arrangements relative to the absolute coordinate system. The origin of the coordinate system is at the common focal point of all of the objectives. We assume that each objective is the W N-Achroplan 63x by 0.9 M27 (Carl Zeiss, Inc., Thornwood, NY). This is a water-immersion objective with the following parameters: Numerical aperture, $NA = 0.9$; index of refraction, $n = 1.33$ (water); working distance; $WD = 2.4$ mm. Working distance is the distance from the surface of the objective lens to the focal plane. Throughout the analysis, it is assumed that the illumination and detection light are both polarized in the x-direction with a wavelength of $\lambda = 515$ nm. These assumptions are constant throughout this entire chapter.

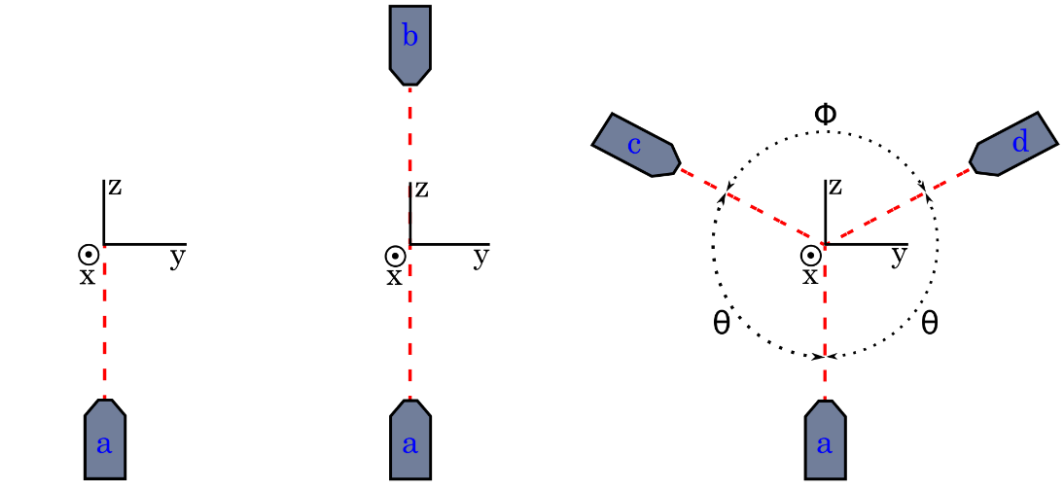

Fig. 6.1 Geometry of one, two and three-objective arrangements. The origin of the coordinate system is at the common focal point of all of the objectives in each of the arrangements. For most of the analysis in this chapter, $\theta = \phi = 120°$ in the three-objective arrangement. The lone exception to this is an investigation into the effect of pupil clipping in section 6.1.3.

All PSF volumes are $(4\times4\times4)(\mu\text{m})^3$ and $(256)^3$ pixels. Each volume is normalized such that the maximum intensity is unity. The PSF figures throughout the chapter show slices taken from the normalized PSF volume. These are the three orthogonal planes passing through the origin, i.e. $(0,y,z)$, $(x,0,z)$ and $(x,y,0)$. Some of the figures show line plots in addition to the slices. These plots compare the PSFs of the one, two and three- objective arrangements along the coordinate axes.

For the OTF volumes, PSFs with the dimensions $(11.52\times11.52\times11.52)(\mu\text{m})^3$, comprising $(256)^3$ pixels were created. The OTF is then the Fourier transform of this volume. Each OTF volume is normalized such that the maximum value is unity. The planes $(0,k_y,k_z)$, $(k_x,0,k_z)$ and $(k_x,k_y,0)$ are shown in the OTF figures. The PSFs from which the OTFs are created have a pixel size of $11.52\ \mu\text{m}/256 = 45\ \text{nm}$ in the three directions $\hat{x}$, $\hat{y}$ or $\hat{z}$. Therefore, the Fourier Transforms of these new PSFs have a Nyquist frequency of $k_{\max} = (2\pi/90)\text{nm}^{-1}$ along the directions $\hat{k}_x$, $\hat{k}_y$ and $\hat{k}_z$. Each

OTF figure also shows line plots along the k_x, k_y and k_z axes for the one, two and three- objective arrangements. These line plots show the base 10 logarithm of the OTF values plotted against the normalized spatial frequency.

All calculations were done in Python^{TM} version 2.7. The various modules which apply the methods of Chapters 4 and 5 are reproduced in the appendix of this text and are referenced throughout this chapter. The Python module "numpy" (NumPy Developers, http://www.numpy.org/) is used for array operations and mathematical constants and functions. The module "pp" (Parallel Python Software, http://www.parallelpython.com) is called in several of these modules. This module allows parallel computation across multiple cpu cores. It significantly reduced computation times and was quite easy to use. It is highly recommended that the interested reader visit the website to learn more.

6.1 Confocal Results

6.1.1 Confocal Illumination Results

We begin with a quantitative description of the intensity in the object space for coherent illumination in the one, two and three- objective arrangements. Here, every objective in each arrangement utilizes its full pupil. These PSFs and OTFs were created with the "evec_clipping" module (see appendix, A.1.1). This is the same module used for calculating the clipped pupil PSF. Setting the parameter "delta" to 0 reduces the code to the standard vectorial method of Richards and Wolf in which the full pupil is utilized.

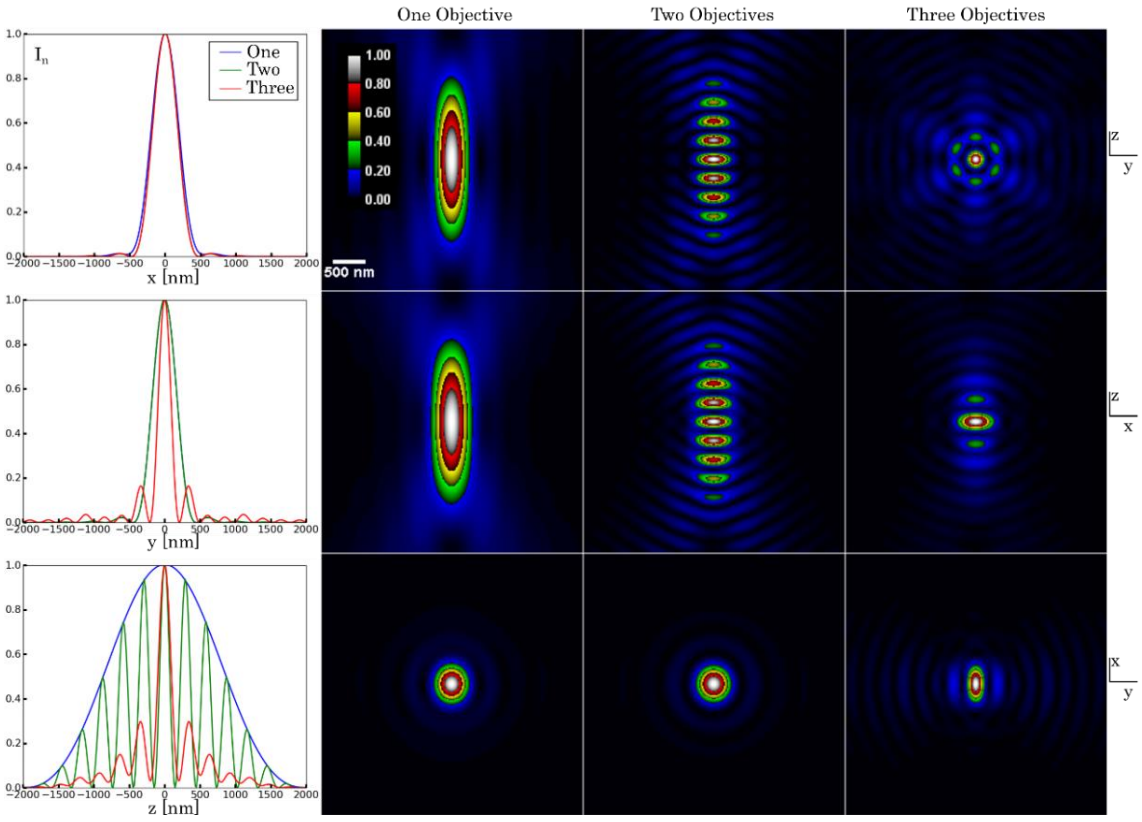

Fig. 6.2 Confocal illumination PSFs for one, two and three- objectives. I_n is the normalized intensity. The coordinate system is shown in Fig. 6.1. In the data presented here, $\theta = \phi = 120°$ for the three-objective arrangement.

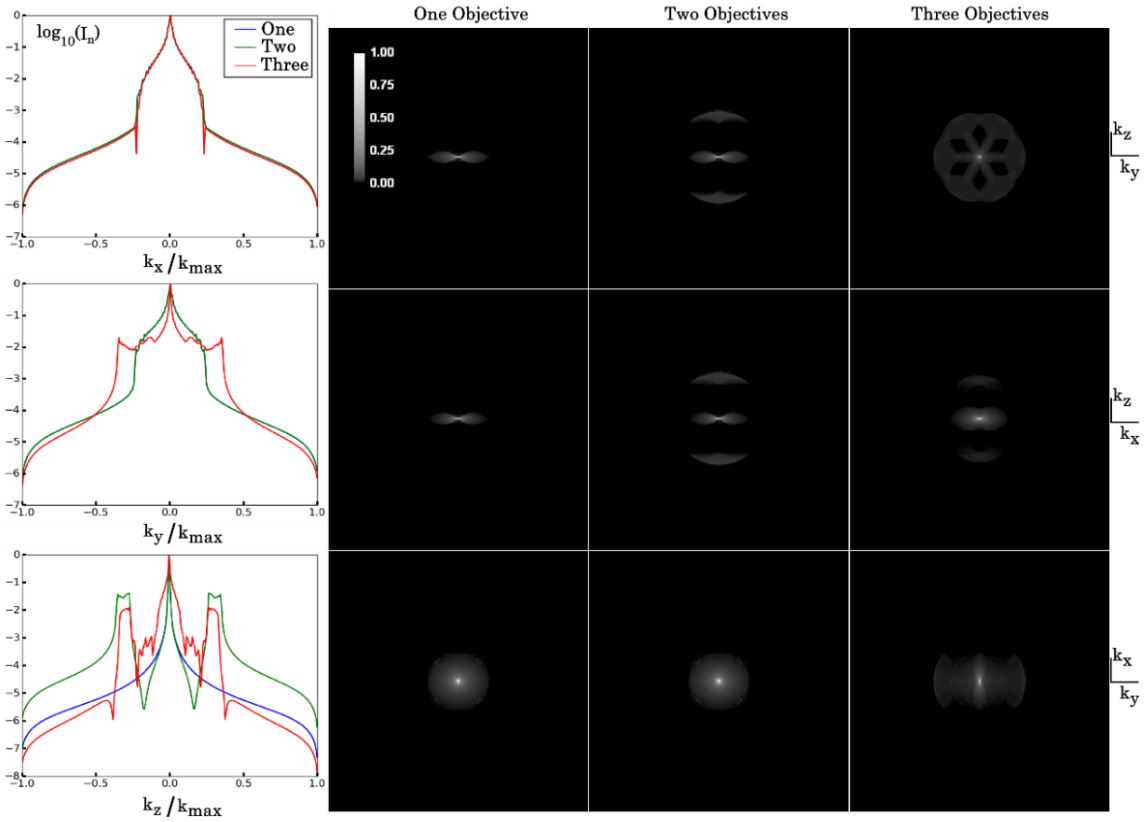

Fig. 6.3 Confocal illumination OTFs for one, two and three- objectives. I_n is the normalized intensity. The Nyquist frequency is $k_{\max} = (2\pi/90)n\text{m}^{-1}$.

In Fig. 6.2, note the isotropy of the three-objective case in the plane of the objectives ($x = 0$). The central peak has an isotropic full width at half maximum (FWHM) of 196 nm in this plane. Note that relative intensities above 0.4 are confined to the small, circular region in the center. This is superior to the single objective transverse and axial FWHMs of 382 nm and 1736 nm in the $\hat{y}$ and $\hat{z}$ directions respectively. The two-objective case has impressive axial performance, but with a caveat. There are several high intensity lobes along the z-axis and in close proximity to the central lobe. The FWHM of adjacent lobes are only about 120 nm apart. So, while it does have an isolated central peak with impressive axial extent, the proximity of the central peak to the adjacent lobes and the high intensity of these lobes increases the likelihood that imperfections in a real microscope and/or multiple fluorophores in close proximity will cause the central peak to be indistinguishable from the adjacent lobes. In contrast, the three-objective PSF has a well isolated central peak. There are six equal intensity

lobes surrounding the central peak and separated by $60°$. The line plot along the z-axis in Fig. 6.2 passes through two of these lobes. These lobes have the same displacement from the central peak as the first set of lobes in the two-objective arrangement – but in the two-objective arrangement these lobes have a relative intensity of about 0.9, whereas in the three-objective arrangement they have a relative intensity of about 0.3. Also note that single and double objective arrangements have identical resolution in the $z = 0$ plane. The three-objective arrangement has improved resolution in the y-direction in this plane. The three-objective arrangement has better resolution than the single and double objective arrangements along the y and z axes. Its worst resolution is along the x-axis, and even then it has marginally better resolution than the single and double objective arrangements.

Fig. 6.3 shows the OTFs for these arrangements. The most striking features of the three-objective OTF are the symmetry and continuity of the $k_x = 0$ slice and the filled-in missing cone in the $k_y = 0$ slice. In the $k_x = 0$ slice, the three-objective OTF reaches higher frequencies than the other OTFs in all directions except for directly along k_z where it is marginally outperformed by the two-objective arrangement. Additionally, the non-supported areas within this extent are relatively small compared to the large gaps between the central and outer lobes of the two-objective OTF. This shows that the three-objective arrangement is more conducive to computational deconvolution techniques which try to bridge the gaps in the OTF. In the $k_y = 0$ slice, it is apparent that the three-objective technique has filled in the missing cone which hampers the single and double-objective arrangements. This indicates that the three-objective arrangement has greater optical sectioning ability and is less affected by out of focus light than the other arrangements.

6.1.2 Confocal Detection Results

For confocal detection, the single and double objective arrangements have identical PSFs and OTFs as their confocal illumination paths. The three-objective case, however, differs slightly due to clipping.

This was discussed in Chapter 4. These PSFs and OTFs were calculated with the “evec_clipping” module (A.1.1). The code in the appendix is commented to explain how to account for clipping in the calculations.

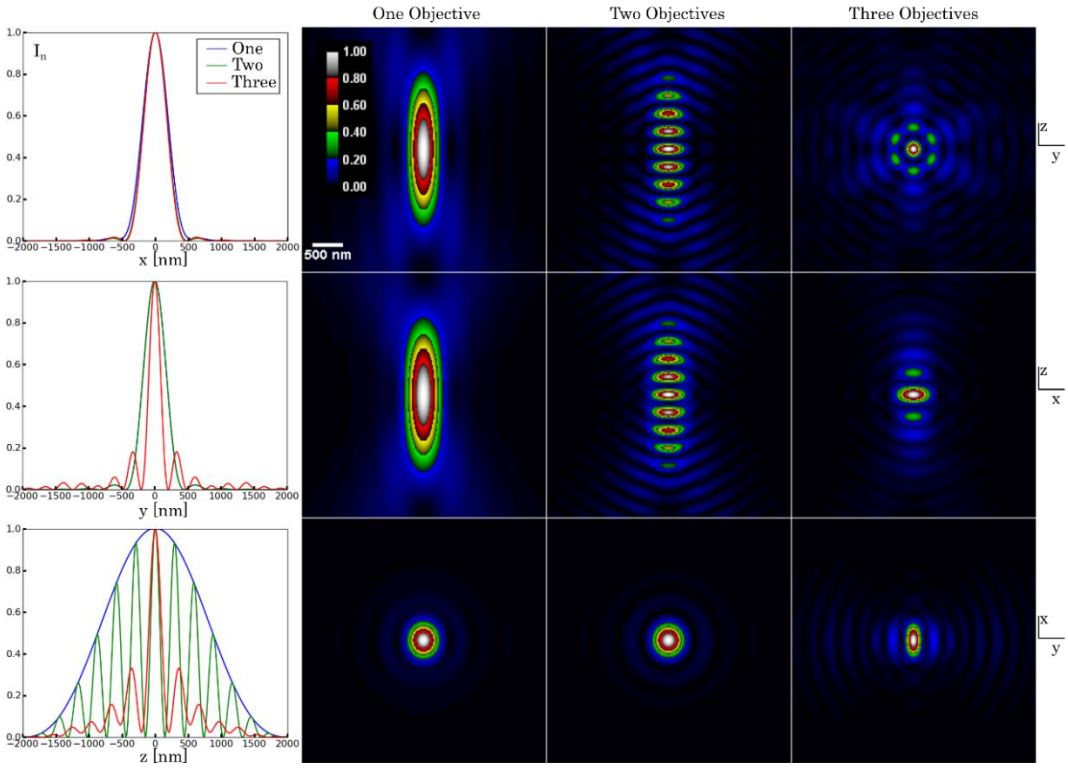

Fig. 6.4 Confocal detection PSFs for one, two and three- objective arrangements. I_n is the normalized intensity. The coordinate system is shown in Fig. 6.1. In the data presented here, $\theta = \phi = 120°$ for the three-objective arrangement.

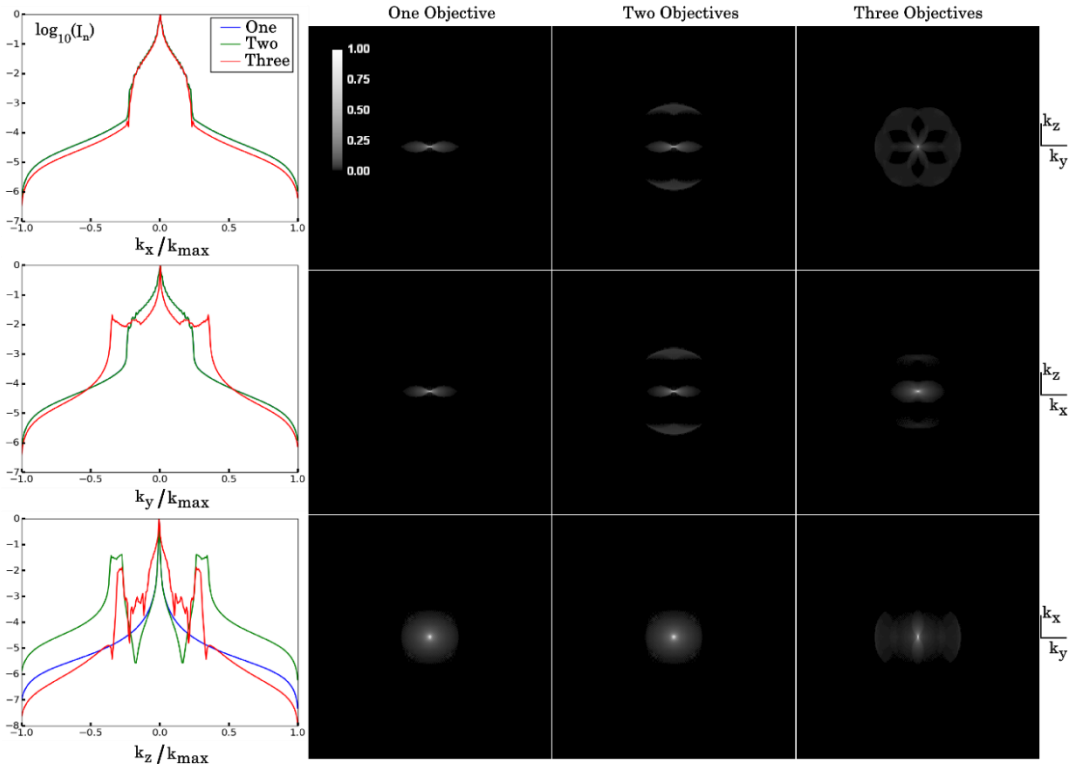

Fig. 6.5 Confocal detection OTFs for one, two and three- objectives. I_n is the normalized intensity. The Nyquist frequency is $k_{\max} = (2\pi/90)n\text{m}^{-1}$.

From Fig. 6.4, it is clear that the clipping pupil has a minimal effect on the detection PSF in the three-objective arrangement. As compared to the illumination PSF, the detection PSF is degraded the most in the x-direction. Even so, the FWHM is only increased by 6 nm. The three-objective detection PSF is essentially identical to the illumination PSF. The OTF, seen in Fig. 6.5, is also essentially identical to the illumination OTF. It seems that we are justified in maintaining $\theta = \phi = 120°$ in our three-objective arrangement and simply discarding the clipped portions of the "c" and "d" pupils when creating the system pupil. We will investigate the resulting confocal effective PSF and the pupil clipping assumption in more detail in the next section.

6.1.3 Confocal Effective PSFs and OTFs and Pupil Clipping Investigation

The effective PSF of a confocal microscope is the excitation PSF multiplied with the detection PSF (Chapter 2). This is the quantity which determines the resolution capabilities of a confocal microscope.

Analyzing the illumination and detection paths separately is important for our analysis because the illumination and detection paths of the three-objective microscope are not identical. In practice though, the effective PSF is the quantity of interest for analyzing and comparing the performance of the different arrangements.

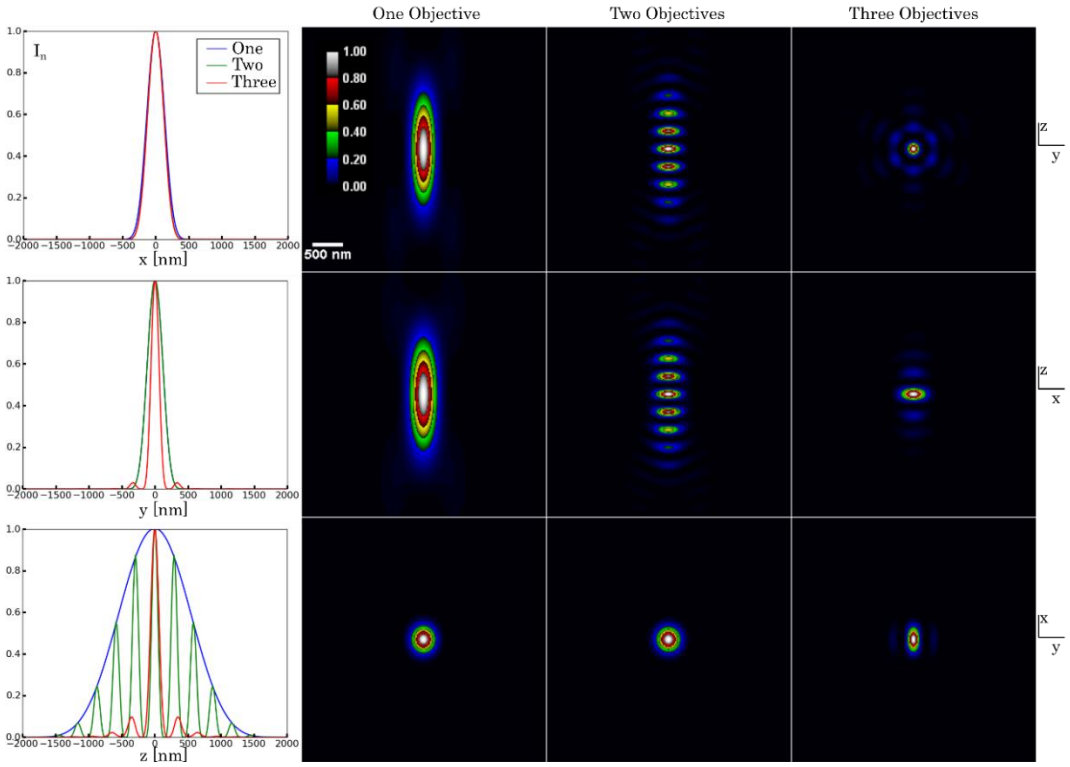

Fig. 6.6 Confocal effective PSFs for one, two and three- objectives. I_n is the normalized intensity. The coordinate system is shown in Fig. 6.1. In the data presented here, $\theta = \phi = 120°$ for the three-objective arrangement.

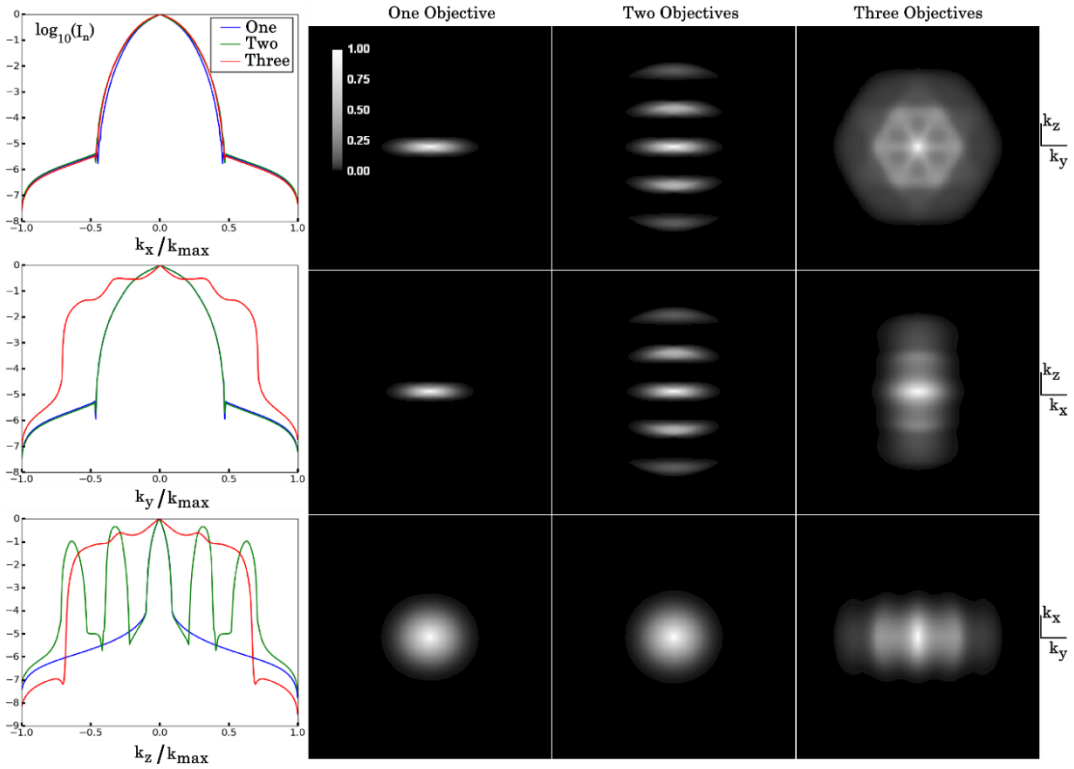

Fig. 6.7 Confocal effective OTFs for one, two and three- objectives. I_n is the normalized intensity. The Nyquist frequency is $k_{\max} = (2\pi/90)n\text{m}^{-1}$.

In the single and double-objective arrangements, the effective PSF is the square of the illumination or the identical detection PSF. In the three-objective case, this is essentially true, since we showed that the illumination and detection PSFs are nearly identical. The squaring of the PSF reduces the extent of the central peak and all sidelobes. The effective PSFs are shown in Fig. 6.6. The single objective PSF has FWHMs of 274 *n*m and 1250 *n*m along the y and z axes respectively. The three-objective approach compares favorably to this with FWHMs of 140 *n*m and 132 *n*m along the y and z axes. Perhaps an even more significant modification due to PSF squaring is the suppresion of the sidelobes relative to the central peak. This phenomenon is quite prominent in the three-objective arrangement. Along the z-axis in the illumination and detection PSFs, the first set of sidelobes had maximum intensities of about 0.3. For the effective PSF, the first set of sidelobes in the three-objective arrangement have a maximum intensity of slightly less than 0.1. The reduction in sidelobes of the PSF is indicated in the OTFs by improved continuity of the OTF support. This is shown in Fig. 6.7. Note the

continuity of the three-objective OTF in all three slices. The three-objective OTF again has a greater extent in all directions except for the $\hat{k}_z$ direction where the two-objective approach has a slightly greater extent. This difference is mitigated by the large gaps in the two-objective OTF. This is a stark contrast to the three-objective approach which has a continuous support in all of the planes. This continuous support is most apparent in the line plots. Note the extent of the three-objective OTF line plots and the lack of lobes throughout the support.

Before we conclude the confocal analysis, we will briefly investigate the pupil clipping phenomenon. Recall that for the three-objective arrangement, the illumination and detection PSFs are nearly, but not strictly identical. We asserted that because of this, we are justified in maintaining the $\theta = \phi = 120°$ three-objective arrangement and discarding the clipped pupil portions. Here we compare the illumination, detection and effective PSFs for the three-objective arrangement in our standard geometry ($\theta = \phi = 120°$) to the corresponding PSFs for a clipping minimizing $\theta = 130.8, \phi = 98.4°$ geometry. Recall from Chapter 4 that this is the point at which the "c" and "d" objectives are in contact with each other.

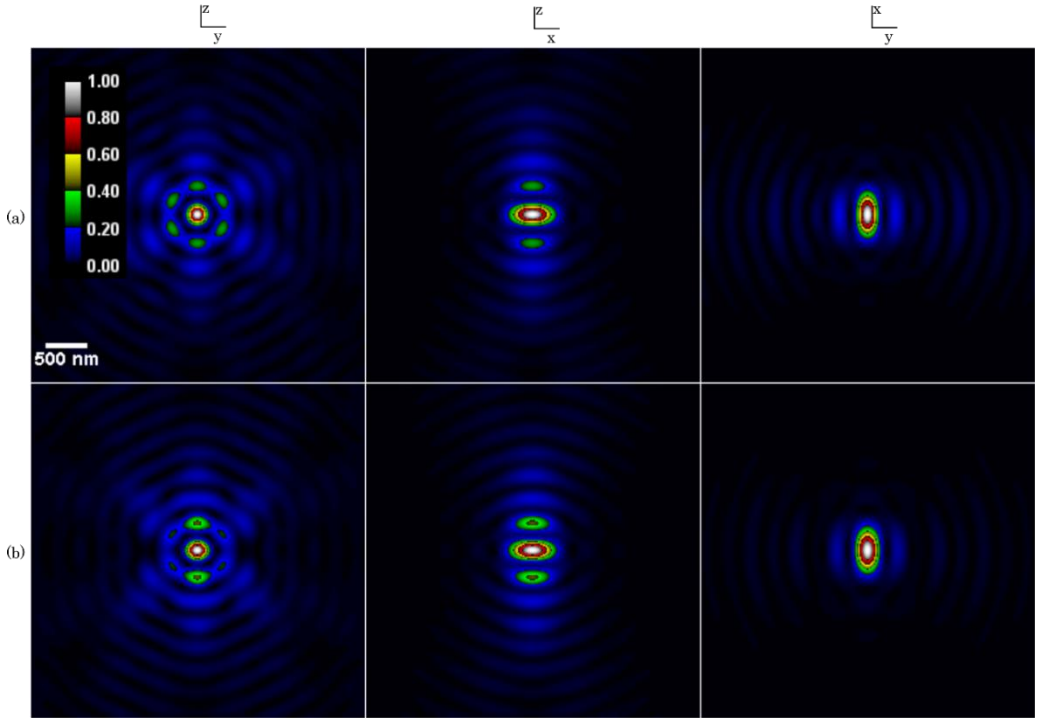

Fig. 6.8 Comparison of illumination PSFs for the three-objective arrangement with (a) $\theta = \phi = 120°$ and (b) $\theta = 130.8, \phi = 98.4°$.

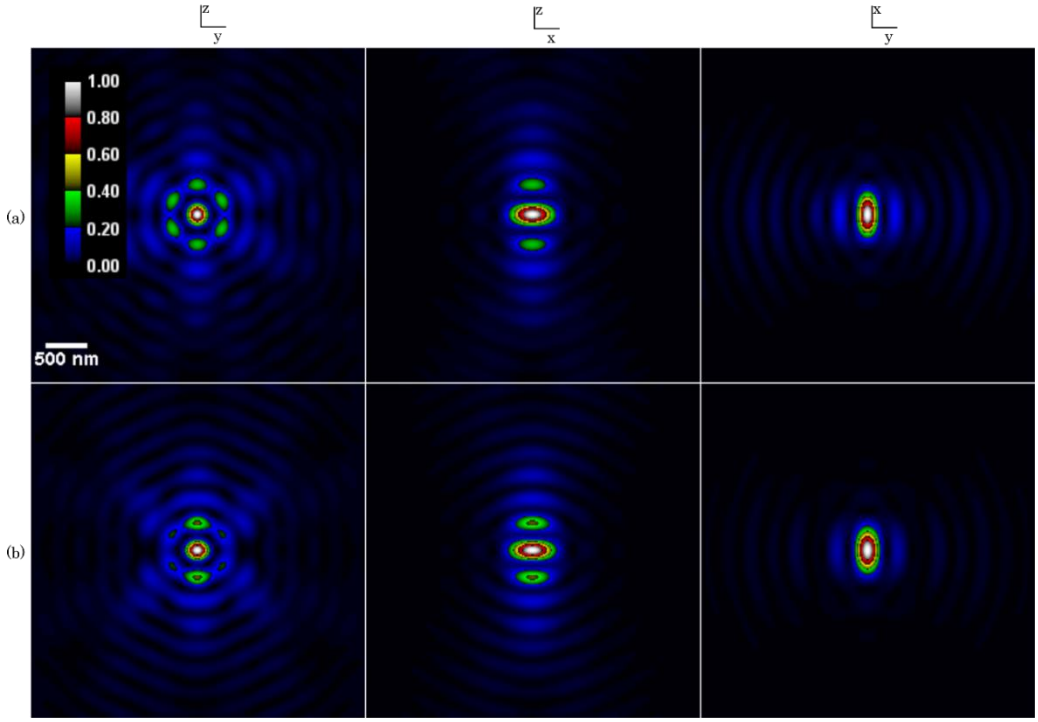

Fig. 6.9 Comparison of detection PSFs for the three-objective arrangement with (a) $\theta = \phi = 120°$ and (b) $\theta = 130.8, \phi = 98.4°$.

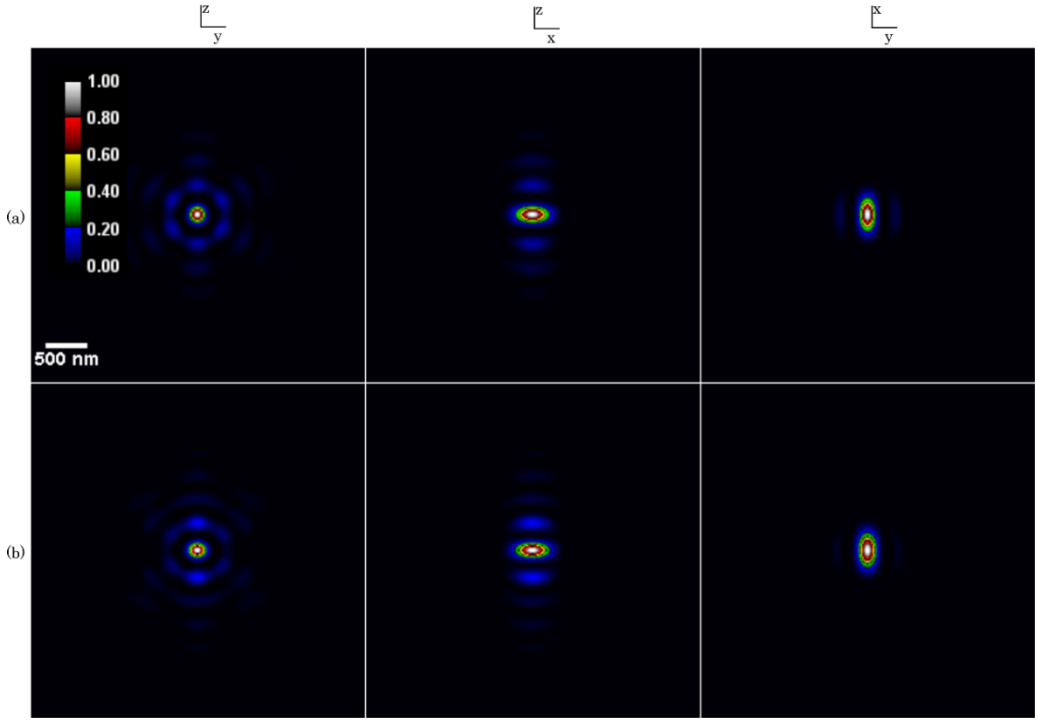

Fig. 6.10 Comparison of effective PSFs for the three-objective arrangement with (a) $\theta = \phi = 120°$ and (b) $\theta = 130.8, \phi = 98.4°$.

Note that the illumination and detection PSFs, in Fig. 6.8 and Fig. 6.9 respectively, are more similar in the clipping minimizing geometry than in the standard geometry. While there is a slight, visible difference in the standard geometry illumination and detection PSFs, the pupil minimizing geometry does not have visibly different illumination and detection PSFs. The difference is so small that it is imperceptible. Even so, the effective PSF (Fig. 6.10) from the standard $\theta = \phi = 120°$ geometry is more isotropic and therefore more favorable than the pupil minimizing effective PSF. Therefore we conclude that the three-objective confocal microscope should be operated in the $\theta = \phi = 120°$ geometry and the clipped pupil portions can simply be discarded.

We conclude the confocal arrangement analysis with a brief summary of our observations. The central peak of the three-objective effective PSF is essentially isotropic in the plane of the objectives (Fig. 6.6). Compared to single and double objective techniques, the three-objective arrangement has superior resolution along the y-axis, marginally better resolution along the x-axis and an identical central peak FWHM in the $\hat{z}$ direction, but with substantially reduced sidelobes compared to the two-

objective arrangement. The three-objective OTF is continuous in all planes shown in Fig. 6.7; this highlights the technique's sidelobe suppression and resistance to the negative effects of out of focus light. Additionally, the OTF support extends farther into frequency space in all directions than single and double objective approaches. The lone exception to this is the $\hat{k}_z$ direction where the two-objective case accesses slightly higher frequencies than the three-objective arrangement. This slight advantage is mitigated by the substantial gaps in the two-objective OTF – a problem which does not affect the three-objective arrangement. We move on now to an analysis of the phase across the pupils for different point source positions.

6.2 Pupil Phase Results and System Pupil Verification

Here we investigate the phase at the pupils of the three-objective arrangement for some different point source positions. It is important to quantify this behavior because we can manipulate the phase at the pupils to scan the focal point through the sample space. Due to the geometry of the arrangement, we must be able to apply tip/tilt and defocus to all objectives in order to scan a volume. This would be accomplished through the use of spatial light modulators (SLM) or deformable mirrors (DM). The data presented here was created with the "angspec" module (A.2.1). The code is commented in the appendix in order to explain how it is applied.

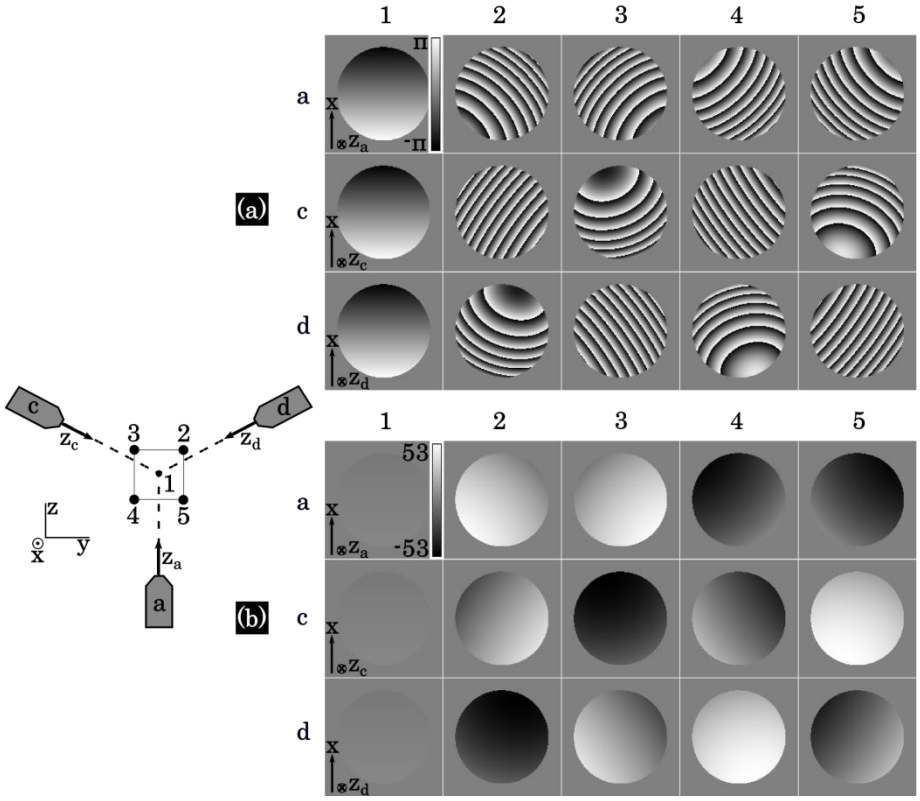

Fig. 6.11 Here we show the phase shift at the pupils for points at the extremities of a $(5\times5\times5)(\mu\text{m})^3$ volume centered at the origin. (a) shows the phase wrapped from $-\pi$ to π. (b) shows the unwrapped phase. The look up table is in units of radians in both plots. Point 1 illustrates the sign convention. It is displaced in the x-direction such that the phase across the pupils is $-\pi$ at the top and π at the bottom. Note that in the sign convention used here, a leading wavefront has a negative sign (black). This is most apparent in the top plot with wrapped phase. The remaining points are: pt. $2(2.5,2.5,2.5)$; pt. $3(2.5,-2.5,2.5)$; pt. $4(2.5,-2.5,-2.5)$; pt. $5(2.5,2.5,-2.5)$ where all units are μm. These are the four corners of the volume which lie in the $x>0$ portion of the coordinate system. The four corners in the $x<0$ mirror these points across the yz plane. For the four corners in the $x<0$ portion, the phase is just the phase of its mirror point flipped with respect to the x-axis.

	1	**2**	**3**	**4**	**5**
a	-3.13 to 3.13	-3.38 to 50.84	-3.38 to 50.84	-50.83 to 3.45	-50.83 to 3.45
c	-3.13 to 3.13	-23.79 to 41.18	-52.83 to 0	-41.16 to 23.85	0 to 52.83
d	-3.13 to 3.13	-52.83 to 0	-23.79 to 41.18	0 to 52.83	-41.16 to 23.85

Table 6.1 Here we show the range of the unwrapped phase values from Fig. 6.10(b). All units are in radians.

In Fig. 6.11 we use the angular spectrum method described in Chapter 4 to show the phase shift at the pupils due to focal points at the corners of a $(5\times5\times5)(\mu\text{m})^3$ volume. Fig. 6.11(a) shows the phase wrapped from $-\pi$ to π. Fig. 6.11(b) shows the unwrapped phase. Additionally, the maximum and

minimum unwrapped phase values are listed in Table 6.1 for each of the pupils. These values are in units of radians. In an adaptive optics device, the stroke is the range of displacements required in the device to correct a particular wavefront. For example, the stroke for pupil "a" and point 1 is $stroke = (3.13 + 3.13)\lambda/2\pi = 0.51\ \mu\text{m}$. The range of phase values shown in Fig. 6.11 corresponds to a stroke of $stroke = (53 + 53)\lambda/2\pi = 8.69\ \mu\text{m}$. This is an easily attainable stroke for today's adaptive optics elements which are capable of strokes up to $50\ \mu\text{m}$.

The pupils shown in Fig. 6.11 would be combined at the tube lens to form the system pupil (Fig. 4.7). So, for example, the system pupil due to point 2 would be the three pupils for point 2 shown in Fig. 6.10 combined in the way shown in Fig. 4.7. To verify that we are calculating the phase across each pupil correctly and that we have the geometry of the system pupil correct, we will use the angular spectrum method to calculate the PSFs for the one, two and three-objective arrangements. The process for creating the PSF from the system pupil is described in Chapter 4. The module "angspec" does this calculation as well.

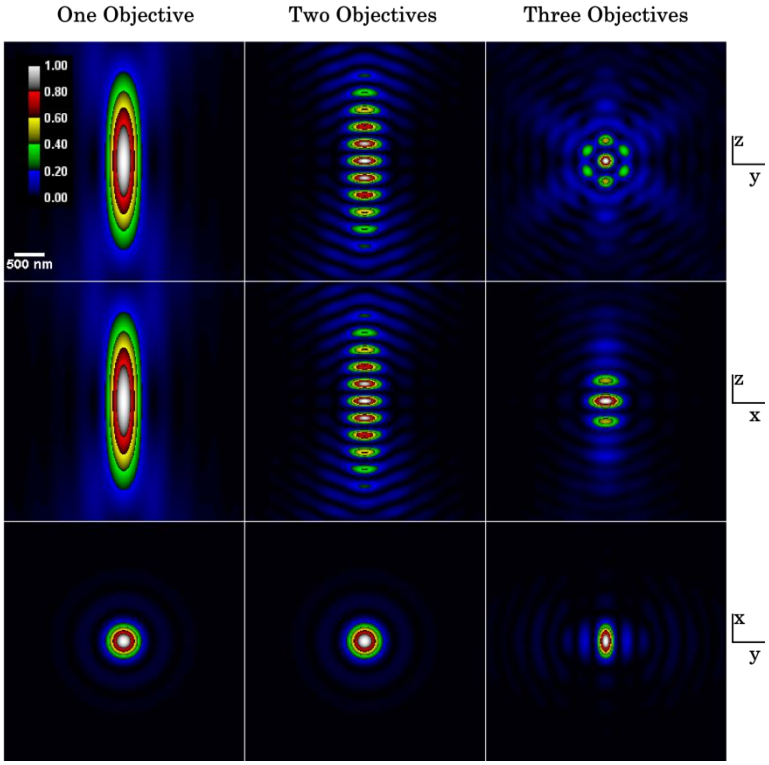

Fig. 6.12 PSFs for one, two and three-objective arrangements determined directly from the system pupil. Note that these PSFs are approximations to the actual PSF. They are displayed here as a way of checking that our system pupil geometry is correct and that we are calculating the phase at the individual objective pupils correctly.

Recall that these PSFs are scalar approximations and as such, they do not describe the PSF of these arrangements as accurately as the vectorial based methods we have employed thus far. These PSFs are shown only as verification that our system pupil is configured correctly. These PSFs look similar enough to the PSFs determined by the vectorial methods that we conclude that our system pupil is arranged correctly.

6.3 Widefield Results

6.3.1 Widefield Illumination Results for One and Two Objectives

Here we present widefield illumination PSFs for one and two-objective techniques. At this time, we have not calculated the illumination PSF for the three-objective arrangement. Certainly the three-objective PSF would have some structure due to interference effects which, when multiplied with the

detection PSF, would improve the isotropy of the effective PSF. A similar effect is seen in the two-objective illumination PSF. The calculation of the three-objective illumination PSF is not as straightforward as the two-objective case, because the objectives are not axially aligned.

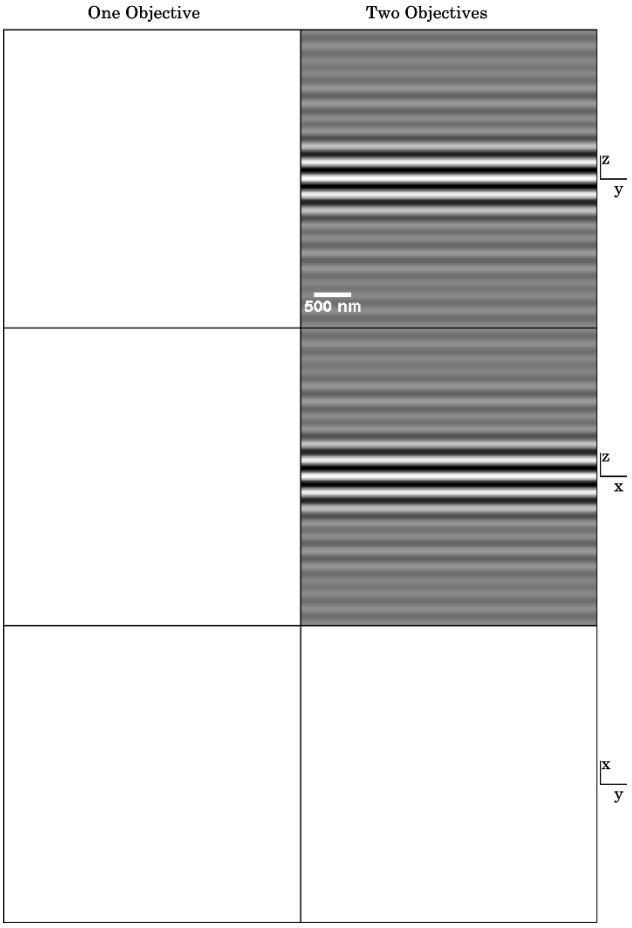

Fig. 6.13 Widefield illumination PSFs for one and two objectives. The intensity values are normalized to 1, where 0 is black and 1 is white in the images. The coordinate system is shown in Fig. 6.1. The two-objective illumination PSF comes from the equation for I^5M illumination from Bewersdorf, et al.[19]

In Fig. 6.13, we see that the widefield illumination PSF for a single objective has a relative intensity of unity everywhere. Thus, there is no resolution gain due to the illumination PSF. In the two-objective arrangement (I^5M), the illumination PSF has well-defined lateral structure which is strongest in intensity within a depth of focus surrounding the focal plane. Beyond this, the intensity drops off rapidly to half of the maximum value. This confers an axial resolution improvement to the effective PSF, but does not affect the lateral extent of the PSF. The three-objective illumination PSF would

certainly have some structure due to interference as well. Thought we do not know the exact distribution currently, we are confident that it would lead to an improved effective PSF when combined with the three-objective detection PSF.

6.3.1 Widefield Detection Results

The widefield detection PSFs for the one and two-objective cases are identical to their confocal detection and illumination counterparts. For the three-objective widefield detection PSFs, we use the vectorial method described by Kim et al.[39] and discussed in Chapter 4. This is necessary because the system focal plane is oblique to the nominal focal planes of objectives "c" and "d" in the three-objective arrangement. All calculations here were done with the "evec_wf" module (A.3). The module is commented in the appendix for a more in depth explanation of how it is applied.

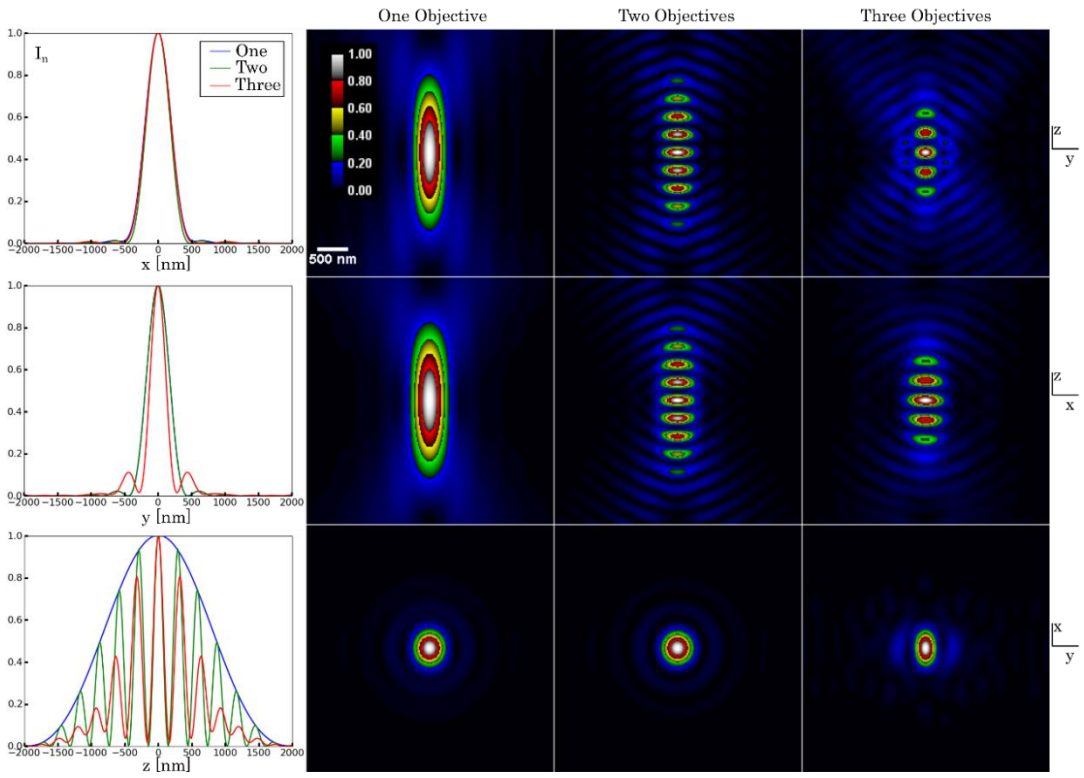

Fig. 6.14 Widefield detection PSFs for one, two and three objectives. I_n is the normalized intensity. The coordinate system is shown in Fig. 6.1. In the data presented here, $\theta = \phi = 120°$ for the three-objective arrangement.

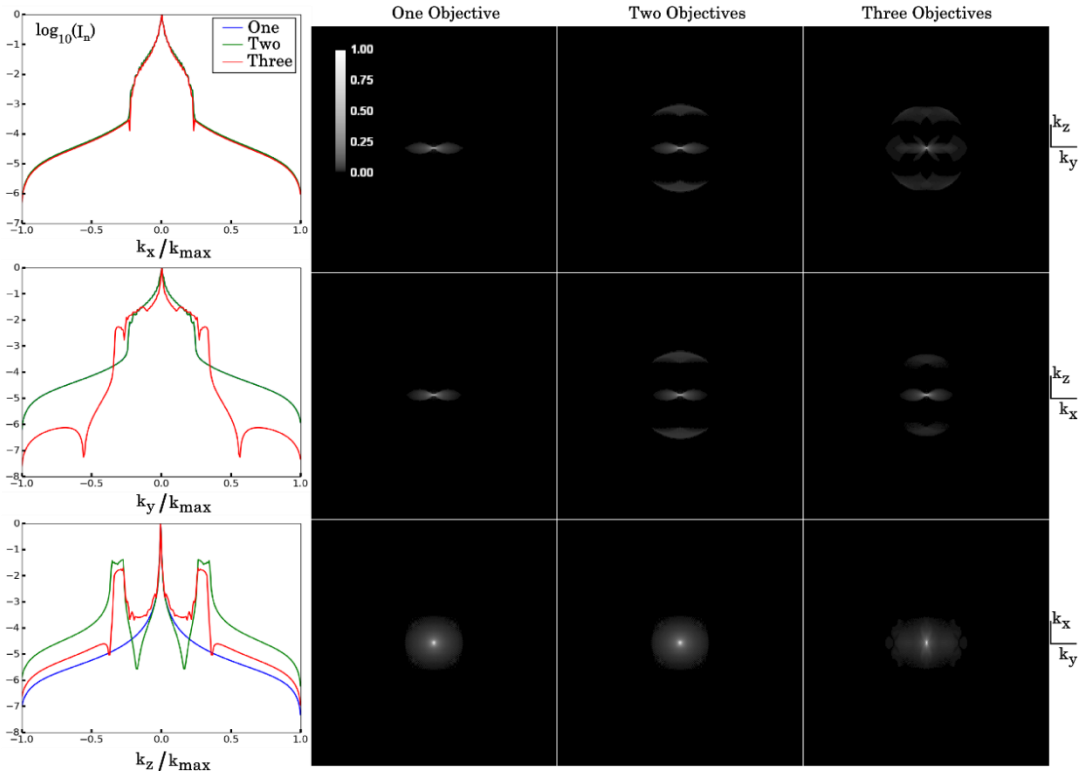

Fig. 6.15 Widefield detection OTFs for one, two and three- objectives. I_n is the normalized intensity. The Nyquist frequency is $k_{\max} = (2\pi/90)m\text{m}^{-1}$.

The single and double-objective widefield detection PSFs and OTFs are identical to the confocal illumination and detection PSFs discussed earlier in the chapter. The three-objective PSFs and OTFs are fundamentally different because of the oblique imaging at the "c" and "d" objectives. For both of these objectives, the system focal plane is oblique to their nominal focal plane by $60°$. This reduces the effective pupil utilized by each objective (Fig. 5.4) and adversely affects their contributions to the PSF (Fig. 6.14). In the confocal case, the three-objective arrangement has improved resolution isotropy and reduced central peak extent because it has three times the effective aperture of a single-objective technique. This effective aperture gain is significantly reduced in the widefield arrangement because of the reduced effective pupil of the "c" and "d" objectives due to the oblique plane imaging required along these objective arms.

The widefield detection PSFs are shown in Fig. 6.14. For the three-objective arrangement, the central peak in the $x = 0$ plane is close to isotropic. The FWHMs are 260 nm and 164 nm along the y and z axes respectively. This is not substantially different than the confocal detection PSF central lobe in the same plane. The central peak in the other two slices follows this same trend of slightly increased anisotropy. The most detrimental effect of the oblique imaging is the introduction of the high intensity lobes near the central peaks in the three-objective slices. This is most evident in the z-axis line plot. We see that the lobes in this case are at similar intensity levels to the two-objective arrangement. This effect is apparent in the OTF in Fig. 6.15 as discontinuous OTF supports in the $k_x = 0$ and $k_y = 0$. In the $k_x = 0$ slice, the lobes are no longer connected to the central portion of the OTF support. In the $k_y = 0$ slice, we see the missing cone. When employed in a widefield technique, it seems that the three-objective detection path does not have improved optical sectioning abilities compared to single or double objective approaches.

6.3.2 Widefield Effective PSFs and OTFs for One and Two Objectives

Here we briefly show and discuss the effective PSFs for single and double objective widefield techniques. The three-objective effective PSF is excluded here because we only know its detection PSF. The single-objective effective PSF is identical to its detection PSF because its illumination PSF is uniform. The two-objective effective PSF benefits from the axially varying structure of its illumination PSF. As discussed, the three-objective illumination path would certainly have some resolution improving structure as well.

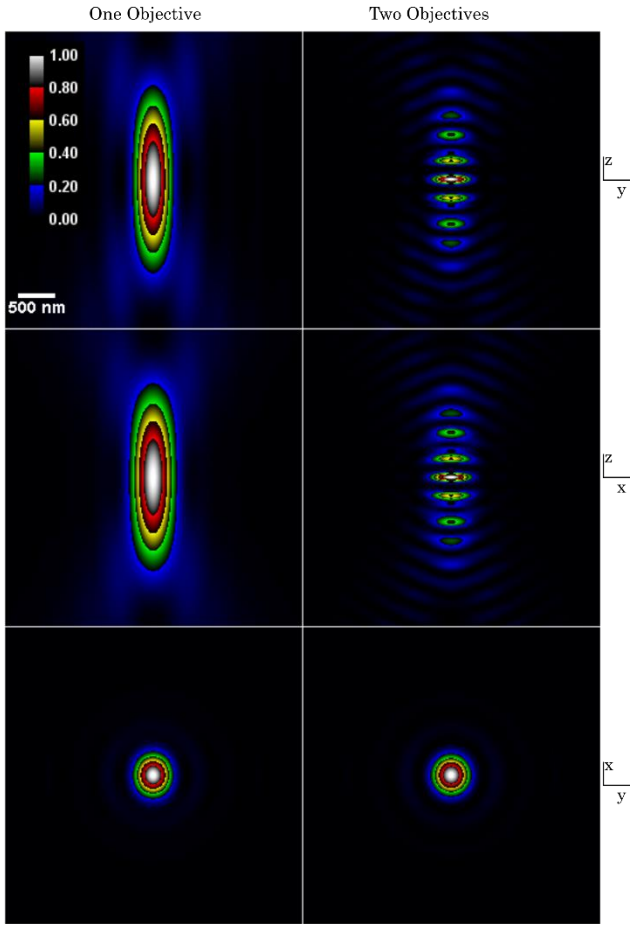

Fig. 6.16 Widefield effective PSFs for one and objectives. I_n is the normalized intensity. The coordinate system is shown in Fig. 6.1.

It should be mentioned that the three-objective arrangement could use a single objective for the illumination path and all three objectives in the detection path. In this case, the effective PSF is the detection PSF shown in Fig. 6.14. The three-objective widefield detection PSF compares favorably with the single objective effective PSF shown in Fig. 6.16. The double objective effective PSF of Fig. 6.16, however, has its sidelobes suppressed due to the confined axial structure of its illumination PSF. The three-objective approach would need to utilize interferometric effects in the illumination path in a similar way in order to be considered a viable alternative to the two-objective widefield approach.

In this chapter we have applied the methods of Chapters 4 and 5 to quantitatively describe the three-objective arrangement employed in confocal and widefield microscopy techniques and we have compared these results to single and double objective arrangements. Throughout the chapter, we

referenced the Python™ modules in the appendix which carry out the methods of Chapters 4 and 5 to produce the data shown here. This code is commented in the appendix for clarity. The intent is for the reader to be able to easily reproduce all results shown here if desired. Now we continue to Chapter 7 where we will conclude our investigation of the proposed system.

Chapter 7

Discussion and Conclusion

7.1 Additional Advantages of Three-objective Arrangement

The proposed arrangement has significantly better light collection efficiency than single objective techniques. Light collection efficiency goes as pupil area. Therefore, the three-objective arrangement will have three times the collection efficiency as a single objective technique and 3/2 times the collection efficiency of two-objective methods. This means that the proposed system can image a larger volume than prior techniques before the sample is photobleached because it needs fewer fluorophore emissions per unit volume of sample being imaged.

This additional light collection efficiency is important because it supports utilization of another one of the proposed arrangements advantages. Namely, it has a much larger imageable sample volume than other techniques with comparable resolution. An agarose gel cylinder with a radius equal to the working distance of the objectives (2.4 mm) can fit inside the sample space. The two most prominent two-objective techniques (I ^{5}M, 4pi) use two objective lenses of $NA = 1.4$. The resulting sample space is only about $300\ \mu m$ thick – a factor of 8 smaller than the proposed arrangement. It should be mentioned that the higher NA used in the literature eliminates the OTF gaps shown in the two-objective arrangements of Chapter 6 which use the same $NA = 0.9$ objective as the proposed three-objective arrangement.

7.2 Microscope Design

The proposed arrangement also presents some interesting challenges. The technique depends on interferometric effects in the illumination and detection paths for its increased resolution. Establishing and maintaining interference is therefore extremely important. There are two things to consider when doing this. First of all, maintaining path-length coherence for the three objectives is quite difficult. This is a necessary requirement because path length coherence is needed for interferometric combination of the images from each of the objectives. A quick calculation considering the commonly used fluorophore, Alexa 488, shows that the path lengths of the three objectives must all be within 2.18 microns of each other. Translation stages with this level of precision exist, but they currently cost upwards of $12,000. Additionally, biological samples naturally have varying indices of refraction throughout the sample. This can distort or destroy the phase coherence. The phase of a wave is $k_0 nd$ where k_0 is the vacuum wavenumber of the light, n is the index of refraction and d is the distance traveled. Throughout our analysis, it has been assumed that n is constant. Thus, the phase of a given disturbance depends only on the distance traveled. In an actual biological sample, this is not the case. Two equidistant but unique paths through the sample can have different phases. This effect can be mitigated by adaptive optics techniques and imaging relatively thin samples.

A possible additional challenge is the sample space itself. In order to increase NA, we would use a water filled chamber for the sample space. This is why we chose a water immersion objective as our reference objective (A.1). Selective plane illumination microscopy (SPIM) uses a water-filled box with two objectives entering through adjacent sides.[27] We envision using something similar to this in our proposed arrangement.

7.3 Conclusion

We began this thesis by motivating a search for a microscope which is better at producing high-resolution 3D images than current state-of-the art widefield and confocal methodologies. Current widefield and confocal microscopes have anisotropic PSFs. Also, widefield techniques in particular are not adept at minimizing the effect of out of focus light. This leads to substantial side lobes in the single objective PSF. We have proposed a microscope consisting of three co-planar objectives (W N-Achroplan 63x by 0.9 M27, Carl Zeiss, Inc., Thornwood, NY; See appendix, A.1) with a common focal point and 120° separation between them (Fig 1.2) as a solution to the resolution anisotropy of single objective widefield and confocal microscopes.

In Chapter 2 we introduced fluorescence microscopy and some fundamental parameters of a microscope. We also introduced the mathematical framework of the linear systems approach to optical systems and how an optical system's impulse response, or point spread function, is the fundamental measure of that system's resolution capability. Finally, we briefly discussed how widefield and confocal techniques are affected by out of focus light and methods for mitigating this effect. Namely, widefield techniques rely on computational deconvolution whereas confocal techniques physically eliminate out of focus light with a pinhole at the detection aperture. Eliminating out of focus light is important for optical sectioning.

In Chapter 3 we discussed various approaches in the literature which try to solve the resolution anisotropy problem of single objective techniques. Mirror based techniques offer impressive resolution and lack chromatic aberration, but due to strong coma aberration, they are relegated to point scanning techniques in which the sample is scanned. The two-objective techniques, 4pi and I^5M, are the most similar to our proposed solution. They both utilize interferometric effects to improve effective resolution. These techniques are quantitatively compared with single objective techniques and our proposed arrangement in Chapter 6 of the text. Finally in Chapter 3, we briefly discussed a class of

techniques which increase resolution by modifying the pupil function. These techniques greatly reduce signal strength – a significant disadvantage in the confocal microscopes in which they are employed.

We introduced the theoretical framework for modeling the proposed system in a confocal arrangement in Chapter 4 and a widefield arrangement in Chapter 5. After discussing these methods, we presented and compared PSF and OTF data for one, two and three objectives employed in confocal and widefield microscope techniques in Chapter 6. From this data, we conclude that the three-objective arrangement operated in a confocal mode is a viable solution to the resolution anisotropy of single objective techniques and poor optical sectioning of single objective widefield microscopy. The three-objective confocal microscope has one central peak in all of the slices shown and continuous OTF support which extend farther into frequency space than single and double objective confocal techniques. Additionally, we showed the phase shift at each of the pupils required for various focal point positions.

The three-objective arrangement widefield analysis does not include the illumination PSF. For the widefield detection PSF, the three-objective arrangement is not as substantial of an improvement over the single and double objective detection PSFs as it is in the confocal technique. This is due to the reduced effective pupils of the “c” and “d” objective caused by oblique plane imaging of the system focal plane. This reduces the effective aperture of the system. In Fig. 6.14, there are strong lobes in close proximity to the central peak of the three-objective arrangement. This manifests itself as a discontinuous OTF support in Fig. 6.15. Still, the three-objective arrangement has a smaller, more isotropic central peak than the single and double-objective widefield detection paths. It is probable that the three-objective illumination PSF would have an interference structure that, when combined with the detection PSF, yields a three-objective widefield effective PSF that is more isotropic and has more continuous OTF supports than its single and double objective counterparts.

In conclusion, we have shown that the proposed three-objective arrangement operated in a confocal technique has a more isotropic PSF with lower intensity sidelobes than single and double

objective confocal techniques. We have also shown the necessary phase shift at each of the pupils in order to scan the focal point throughout the sample volume, as well as the correct geometry for combining the individual pupils at the tube lens. Finally, we have shown the proposed arrangement's widefield detection PSF and are confident that combining it with the as yet undetermined illumination PSF would yield an effective PSF which compares favorably to single and double objective widefield techniques.

In the future, we hope to quantitatively describe the three-objective arrangement's illumination PSF. From that, we can make a more accurate assessment of how the three-objective arrangement compares to one and two-objective methods in a widefield technique. From there we would move on into exploring adaptive optics solutions to maintain the necessary interference effects in the proposed microscope and to allow deeper penetration into tissues. Since the hallmark of this new approach is 3D imaging, then steps must be taken to optimize its performance when dealing with thick samples. This is currently an open and active field in fluorescence microscopy[40,41] and it is the logical next step in extending the idea of the three-objective interferometric microscope proposed here.

References

1 Indovina, P., Collini, M., Chirico, G. & Santini, M. T. Three-dimensional cell organization leads to almost immediate HRE activity as demonstrated by molecular imaging of MG-63 spheroids using two-photon excitation microscopy. *FEBS letters* **581**, 719-726 (2007).

2 Lämmermann, T. *et al.* Cdc42-dependent leading edge coordination is essential for interstitial dendritic cell migration. *Blood* **113**, 5703-5710 (2009).

3 Pampaloni, F., Reynaud, E. G. & Stelzer, E. H. K. The third dimension bridges the gap between cell culture and live tissue. *Nature Reviews Molecular Cell Biology* **8**, 839, doi:10.1038/nrm2236 (2007).

4 Goodman, J. Introduction to Fourier optics. (2008).

5 Streibl, N. Three-dimensional imaging by a microscope. *JOSA A* **2**, 121-127 (1985).

6 Swedlow, J. R., Sedat, J. W. & Agard, D. A. Deconvolution in optical microscopy. *Deconvolution of images and spectra*, 284-309 (1997).

7 McNally, J. G., Karpova, T., Cooper, J. & Conchello, J. A. Three-dimensional imaging by deconvolution microscopy. *Methods* **19**, 373-385 (1999).

8 Claxton, N. S., Fellers, T. J. & Davidson, M. W. Laser scanning confocal microscopy. *Department of Optical Microscopy and Digital Imaging, Florida State University, Tallahassee, http://www. olympusconfocal. com/theory/LSCMIntro.pdf* (2006).

9 Nagorni, M. & Hell, S. W. Coherent use of opposing lenses for axial resolution increase in fluorescence microscopy. I. Comparative study of concepts. *JOSA A* **18**, 36-48 (2001).

10 Davidson, M. W. & Abramowitz, M. Optical microscopy. *Encyclopedia of imaging science and technology* (2002).

11 Drechsler, A., Lieb, M., Debus, C., Meixner, A. & Tarrach, G. Confocal microscopy with a high numerical aperture parabolic mirror. *Opt. Express* **9**, 637-644 (2001).

12 Lieb, M. & Meixner, A. A high numerical aperture parabolic mirror as imaging device for confocal microscopy. *Opt. Express* **8**, 458-474 (2001).

13 Stadler, J., Stanciu, C., Stupperich, C. & Meixner, A. Tighter focusing with a parabolic mirror. *Optics letters* **33**, 681-683 (2008).

14 Liu, J., Tan, J., Wilson, T. & Zhong, C. Rigorous theory on elliptical mirror focusing for point scanning microscopy. *Opt. Express* **20**, 6175-6184 (2012).

15 Liu, J., Zhong, C., Tan, J., Wang, T. & Wilson, T. Elliptical mirror based imaging with aperture angle greater than $\pi/2$. *Opt. Express* **20**, 19206-19213, doi:10.1364/OE.20.019206 (2012).

16 Hell, S. & Stelzer, E. H. K. Properties of a 4Pi confocal fluorescence microscope. *J. Opt. Soc. Am. A* **9**, 2159-2166, doi:10.1364/JOSAA.9.002159 (1992).

17 Hell, S., Schrader, M. & Van Der Voort, H. Far-field fluorescence microscopy with three-dimensional resolution in the 100-nm range. *Journal of microscopy* **187**, 1-7 (1997).

18 Nagorni, M. & Hell, S. W. Coherent use of opposing lenses for axial resolution increase. II. Power and limitation of nonlinear image restoration. *JOSA A* **18**, 49-54 (2001).

19 Bewersdorf, J., Schmidt, R. & Hell, S. W. Comparison of I5M and 4Pi-microscopy. *Journal of microscopy* **222**, 105-117 (2006).

20 Gustafsson, M. G., Agard, D. A. & Sedat, J. W. in *IS&T/SPIE's Symposium on Electronic Imaging: Science & Technology.* 147-156 (International Society for Optics and Photonics).

21 Gustafsson, M., Agard, D. & Sedat, J. I5M: 3D widefield light microscopy with better than 100nm axial resolution. *Journal of microscopy* **195**, 10-16 (1999).

22 Richards, B. & Wolf, E. Electromagnetic Diffraction in Optical Systems. II. Structure of the Image Field in an Aplanatic System. *Proceedings of the Royal Society A: Mathematical, Physical and Engineering Sciences* **253**, 358-379, doi:10.1098/rspa.1959.0200 (1959).

23 Reynaud, E. G., Kržič, U., Greger, K. & Stelzer, E. H. K. Light sheet-based fluorescence microscopy: More dimensions, more photons, and less photodamage. *HFSP Journal* **2**, 266-275, doi:10.2976/1.2974980 (2008).

24 Engelbrecht, C. J. & Stelzer, E. H. Resolution enhancement in a light-sheet-based microscope (SPIM). *Optics Letters* **31**, 1477-1479, doi:10.1364/OL.31.001477 (2006).

25 Ritter, J., Veith, R., Siebrasse, J.-P. & Kubitscheck, U. High-contrast single-particle tracking by selective focal plane illumination microscopy. *Opt. Express* **16**, 7142-7152 (2008).

26 Huisken, J., Swoger, J., Lindek, S. & Stelzer, E. H. in *Handbook of Biological Confocal Microscopy* 672-679 (Springer, 2006).

27 Huisken, J., Swoger, J., Del Bene, F., Wittbrodt, J. & Stelzer, E. H. Optical sectioning deep inside live embryos by selective plane illumination microscopy. *Science* **305**, 1007-1009 (2004).

28 Swoger, J., Huisken, J. & Stelzer, E. H. Multiple imaging axis microscopy improves resolution for thick-sample applications. *Optics letters* **28**, 1654-1656 (2003).

29 Gu, M., Tannous, T. & Sheppard, C. Improved axial resolution in confocal fluorescence microscopy using annular pupils. *Optics communications* **110**, 533-539 (1994).

30 Ojeda-Castañeda, J., Martínez-Corral, M., Andrés, P. & Pons, A. Strehl ratio versus defocus for noncentrally obscured pupils. *Applied optics* **33**, 7611-7616 (1994).

31 Martinez-Corral, M., Andres, P., Zapata-Rodriguez, C. & Sheppard, C. Improvement of three-dimensional resolution in confocal scanning microscopy by combination of two pupil filters. *Optik* **107**, 145-148 (1998).

32 Martinez-Corral, M., Caballero, M., Stelzer, E. H. K. & Swoger, J. Tailoring the axial shape of the point spread function using the Toraldo concept. *Opt. Express* **10**, 98-103, doi:10.1364/OE.10.000098 (2002).

33 de Juana, D. M., Oti, J. E., Canales, V. F. & Cagigal, M. P. Transverse or axial superresolution in a 4Pi-confocal microscope by phase-only filters. *JOSA A* **20**, 2172-2178 (2003).

34 Sheppard, G. & Matthews, H. Imaging in high-aperture optical systems. *JOSA A* **4**, 1354-1360 (1987).

35 Wolf, E. Electromagnetic diffraction in optical systems. I. An integral representation of the image field. *Proceedings of the Royal Society of London. Series A. Mathematical and Physical Sciences* **253**, 349-357 (1959).

36 Dunsby, C. Optically sectioned imaging by oblique plane microscopy. *Opt. Express* **16**, 20306-20316 (2008).

37 Maxwell, J. C. *Quarterly Journal of Pure and Applied Mathematics* **2**, 288 (1858).

38 Botcherby, E., Juškaitis, R., Booth, M. & Wilson, T. An optical technique for remote focusing in microscopy. *Optics Communications* **281**, 880-887 (2008).

39 Kim, J., Li, T., Wang, Y. & Zhang, X. Vectorial point spread function and optical transfer function in oblique plane imaging. *Opt. Express* **22**, 11140-11151 (2014).

40 Booth, M. J. *Adaptive optics in microscopy*. Vol. 365 (2007).

41 Schwertner, M., Booth, M., Neil, M. & Wilson, T. Measurement of specimen-induced aberrations of biological samples using phase stepping interferometry. *Journal of microscopy* **213**, 11-19 (2004).

Appendices

A.1 Objective Dimensions

W N-Achroplan 63x by 0.9 M27, Carl Zeiss, Inc., Thornwood, NY

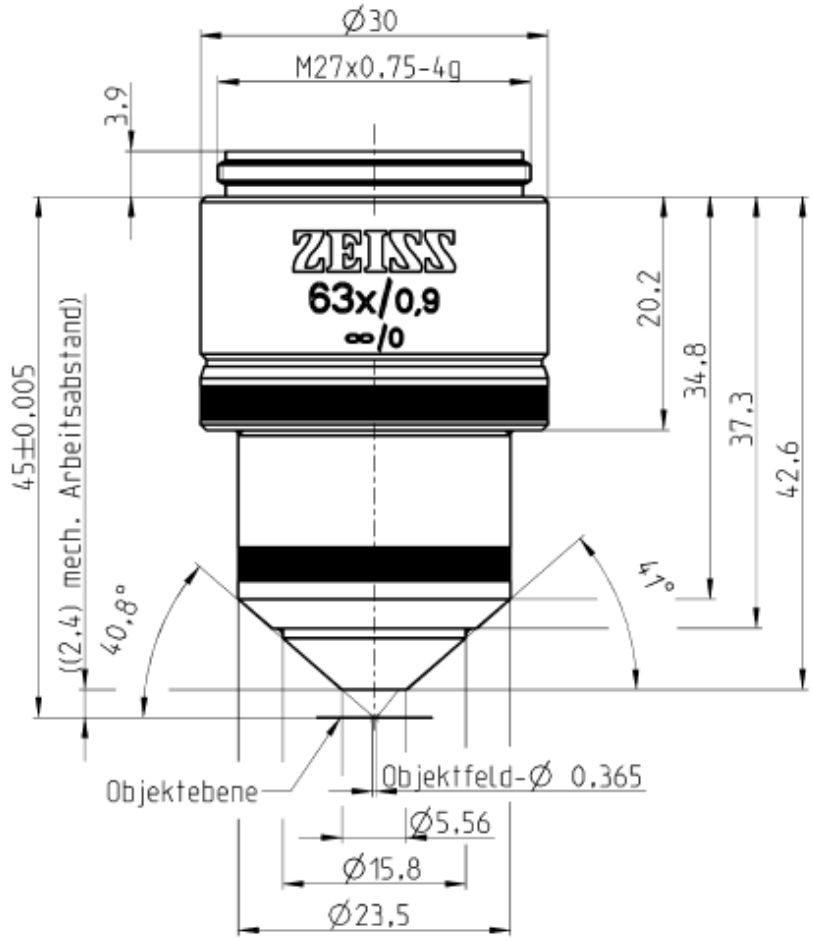

All dimensions are in mm. Image from Carl Zeiss, Inc. (https://www.micro-shop.zeiss.com/).

A.2 Confocal Code

"evec_clipping" module

```
import numpy as N
import simpson
import time
import divider


class EMatclip(object):
    '''''This returns the electric field distribution resulting from a clipped pupil (c
hapter 4).
    It is a modified version of Richards and Wolf. When delta=0.0, this returns the
    same results as Richards and Wolf (full pupil). ctype describes which side of
    the pupil is clipped. In the three-objective arrangement, both the 'c' objective
    and the 'd' objective have delta = 12.59 degrees. But the 'c' objective has
    ctype='dclip' and the 'd' objective has ctype='cclip'.'''
    def __init__(self,xin=(4.0,256),yin=(4.0,256),zin=(4.0,256),NA=0.9,n=1.33,theta=0.0
,delta=0.0,ctype='dclip',l=0.515,tnum=50,pnum=50):
        start_time = time.time()

        theta = N.deg2rad(theta)
        delta = N.deg2rad(delta)
        gamma = N.arcsin(NA/n) - delta

        xlist = N.linspace(-xin[0]/2,xin[0]/2,xin[1])
        ylist = N.linspace(-yin[0]/2,yin[0]/2,yin[1])
        zlist = N.linspace(-zin[0]/2,zin[0]/2,zin[1])

        xA,yA,zA = N.meshgrid(xlist,ylist,zlist,indexing='ij')

        def xrot(xp,yp,zp,angle):
            x = xp
            y = yp*N.cos(angle) - zp*N.sin(angle)
            z = yp*N.sin(angle) + zp*N.cos(angle)
            return x,y,z

        #Transforming coordinates from absolute coord to objective relative coord
        xc,yc,zc = xrot(xA,yA,zA,-theta)

        #Dividing calculation into three sets of points,
        X,Y,Z,mode = divider.divider(xc,yc,zc,divisions=3)

        #Defining Richards and Wolf calculation based on which side of pupil is clipped

        if ctype == 'dclip':
            def E(xarr,yarr,zarr,phi0,NA,n,l,gam,tnum,pnum):
                #Constants
                thetamax = N.arcsin(NA/n)
                k = 2*N.pi/l
                ##########################################
                #Functions of theta and phi

                #Integrands from Eq. 4.2 from text with trig substitutions to speed cal
culation
```

```
49.                 Exfunc = lambda theta,phi: N.sin(phi)**2 + (N.cos(phi)**2)*N.cos(theta)
50.                 Eyfunc = lambda theta,phi: -
    N.sin(phi)*N.cos(phi) + N.cos(phi)*N.cos(theta)*N.sin(phi)
51.                 Ezfunc = lambda theta,phi: N.cos(phi)*N.sin(theta)
52.
53.                 def P(theta,phi):
54.                     y = N.sin(theta)*N.sin(phi)
55.                     P = N.less_equal(y,N.sin(gam))
56.                     return P
57.
58.                 ##########################################
59.
60.                 xnum,ynum,znum = xarr.shape
61.                 Ex,Ey,Ez = N.zeros((xnum,ynum,znum),dtype=complex),N.zeros((xnum,ynum,z
    num),dtype=complex),N.zeros((xnum,ynum,znum),dtype=complex)
62.                 for nx in range(xnum):
63.                     for ny in range(ynum):
64.                         for nz in range(znum):
65.
66.                             part = lambda theta,phi,x=xarr[nx,ny,nz],y=yarr[nx,ny,nz],z
    =zarr[nx,ny,nz]: (N.cos(theta)**(0.5))*N.sin(theta)*N.exp(-
    1j*k*(xarr[nx,ny,nz]*N.sin(theta)*N.cos(phi) + yarr[nx,ny,nz]*N.sin(theta)*N.sin(phi) -
     zarr[nx,ny,nz]*N.cos(theta)))
67.
68.                             rExint = lambda theta,phi: N.real(Exfunc(theta,phi)*(P(thet
    a,phi))*part(theta,phi))
69.                             iExint = lambda theta,phi: N.imag(Exfunc(theta,phi)*(P(thet
    a,phi))*part(theta,phi))
70.                             rEyint = lambda theta,phi: N.real(Eyfunc(theta,phi)*(P(thet
    a,phi))*part(theta,phi))
71.                             iEyint = lambda theta,phi: N.imag(Eyfunc(theta,phi)*(P(thet
    a,phi))*part(theta,phi))
72.                             rEzint = lambda theta,phi: N.real(Ezfunc(theta,phi)*(P(thet
    a,phi))*part(theta,phi))
73.                             iEzint = lambda theta,phi: N.imag(Ezfunc(theta,phi)*(P(thet
    a,phi))*part(theta,phi))
74.
75.                             rEx = simpson.dblsimps(rExint,(0.0,thetamax,tnum),(0.0,2*N.
    pi,pnum))
76.                             iEx = simpson.dblsimps(iExint,(0.0,thetamax,tnum),(0.0,2*N.
    pi,pnum))
77.                             rEy = simpson.dblsimps(rEyint,(0.0,thetamax,tnum),(0.0,2*N.
    pi,pnum))
78.                             iEy = simpson.dblsimps(iEyint,(0.0,thetamax,tnum),(0.0,2*N.
    pi,pnum))
79.                             rEz = simpson.dblsimps(rEzint,(0.0,thetamax,tnum),(0.0,2*N.
    pi,pnum))
80.                             iEz = simpson.dblsimps(iEzint,(0.0,thetamax,tnum),(0.0,2*N.
    pi,pnum))
81.
82.                             Ex[nx,ny,nz] = N.complex(rEx,iEx)
83.                             Ey[nx,ny,nz] = N.complex(rEy,iEy)
84.                             Ez[nx,ny,nz] = N.complex(rEz,iEz)
85.
86.                 return Ex,Ey,Ez
87.
88.         elif ctype == 'cclip':
89.             def E(xarr,yarr,zarr,phi0,NA,n,l,gam,tnum,pnum):
```

```
90.                 #Constants
91.                 thetamax = N.arcsin(NA/n)
92.                 k = 2*N.pi/l
93.                 ########################################
94.                 #Functions of theta and phi
95.
96.                 Exfunc = lambda theta,phi: N.sin(phi)**2 + (N.cos(phi)**2)*N.cos(theta)
97.                 Eyfunc = lambda theta,phi: -
    N.sin(phi)*N.cos(phi) + N.cos(phi)*N.cos(theta)*N.sin(phi)
98.                 Ezfunc = lambda theta,phi: N.cos(phi)*N.sin(theta)
99.
100.                        def P(theta,phi):
101.                            y = N.sin(theta)*N.sin(phi)
102.                            P = N.greater_equal(y,-N.sin(gam))
103.                            return P
104.
105.                        ########################################
106.
107.                        xnum,ynum,znum = xarr.shape
108.                        Ex,Ey,Ez = N.zeros((xnum,ynum,znum),dtype=complex),N.zeros((xnum
    ,ynum,znum),dtype=complex),N.zeros((xnum,ynum,znum),dtype=complex)
109.                        for nx in range(xnum):
110.                            for ny in range(ynum):
111.                                for nz in range(znum):
112.
113.                                    part = lambda theta,phi,x=xarr[nx,ny,nz],y=yarr[nx,n
    y,nz],z=zarr[nx,ny,nz]: (N.cos(theta)**(0.5))*N.sin(theta)*N.exp(-
    1j*k*(xarr[nx,ny,nz]*N.sin(theta)*N.cos(phi) + yarr[nx,ny,nz]*N.sin(theta)*N.sin(phi) -
     zarr[nx,ny,nz]*N.cos(theta)))
114.
115.                                    rExint = lambda theta,phi: N.real(Exfunc(theta,phi)*
    (P(theta,phi))*part(theta,phi))
116.                                    iExint = lambda theta,phi: N.imag(Exfunc(theta,phi)*
    (P(theta,phi))*part(theta,phi))
117.                                    rEyint = lambda theta,phi: N.real(Eyfunc(theta,phi)*
    (P(theta,phi))*part(theta,phi))
118.                                    iEyint = lambda theta,phi: N.imag(Eyfunc(theta,phi)*
    (P(theta,phi))*part(theta,phi))
119.                                    rEzint = lambda theta,phi: N.real(Ezfunc(theta,phi)*
    (P(theta,phi))*part(theta,phi))
120.                                    iEzint = lambda theta,phi: N.imag(Ezfunc(theta,phi)*
    (P(theta,phi))*part(theta,phi))
121.
122.                                    rEx = simpson.dblsimps(rExint,(0.0,thetamax,tnum),(0
    .0,2*N.pi,pnum))
123.                                    iEx = simpson.dblsimps(iExint,(0.0,thetamax,tnum),(0
    .0,2*N.pi,pnum))
124.                                    rEy = simpson.dblsimps(rEyint,(0.0,thetamax,tnum),(0
    .0,2*N.pi,pnum))
125.                                    iEy = simpson.dblsimps(iEyint,(0.0,thetamax,tnum),(0
    .0,2*N.pi,pnum))
126.                                    rEz = simpson.dblsimps(rEzint,(0.0,thetamax,tnum),(0
    .0,2*N.pi,pnum))
127.                                    iEz = simpson.dblsimps(iEzint,(0.0,thetamax,tnum),(0
    .0,2*N.pi,pnum))
128.
129.                                    Ex[nx,ny,nz] = N.complex(rEx,iEx)
130.                                    Ey[nx,ny,nz] = N.complex(rEy,iEy)
```

```
131.                                    Ez[nx,ny,nz] = N.complex(rEz,iEz)
132.
133.                         return Ex,Ey,Ez
134.
135.                 import pp #Calculation done in parallel using parallel python module
136.                 job_server = pp.Server()
137.                 fn = pp.Template(job_server, E, (), ("numpy as N", "simpson",))
138.
139.                 job1 = fn.submit(X[0],Y[0],Z[0],NA,n,l,gamma,tnum,pnum)
140.                 job2 = fn.submit(X[1],Y[1],Z[1],NA,n,l,gamma,tnum,pnum)
141.                 job3 = fn.submit(X[2],Y[2],Z[2],NA,n,l,gamma,tnum,pnum)
142.
143.                 E1 = job1()
144.                 E2 = job2()
145.                 E3 = job3()
146.
147.                 if mode == 'x':
148.                     Ex,Ey,Ez = N.concatenate((E1[0],E2[0],E3[0]),axis=0),N.concatenate((
    E1[1],E2[1],E3[1]),axis=0),N.concatenate((E1[2],E2[2],E3[2]),axis=0)
149.                 elif mode == 'y':
150.                     Ex,Ey,Ez = N.concatenate((E1[0],E2[0],E3[0]),axis=1),N.concatenate((
    E1[1],E2[1],E3[1]),axis=1),N.concatenate((E1[2],E2[2],E3[2]),axis=1)
151.                 elif mode == 'z':
152.                     Ex,Ey,Ez = N.concatenate((E1[0],E2[0],E3[0]),axis=2),N.concatenate((
    E1[1],E2[1],E3[1]),axis=2),N.concatenate((E1[2],E2[2],E3[2]),axis=2)
153.
154.                 Ex,Ey,Ez = xrot(Ex,Ey,Ez,theta)
155.                 self.Ex,self.Ey,self.Ez = N.squeeze(Ex),N.squeeze(Ey),N.squeeze(Ez)
156.
157.                 end_time = time.time()
158.                 print('Computation completed in '+repr(end_time-
    start_time)+' seconds')
159.
160.
161.             def getpsf(self):
162.                 self.psf = N.abs(self.Ex)**2 + N.abs(self.Ey)**2 + N.abs(self.Ez)**2
163.
164.
165.         def psf(Elist):
166.             '''''This returns the PSF from the superposition of the fields given by Elis
    t.
167.             Elist = (E0,E120,E240) where En = Ematclip(theta=n) will give the three-
    objective
168.             PSF.'''
169.             Exlist,Eylist,Ezlist = [],[],[]
170.             for E in Elist:
171.                 Exlist.append(E.Ex),Eylist.append(E.Ey),Ezlist.append(E.Ez)
172.
173.
174.             Exnet,Eynet,Eznet = N.sum(Exlist,axis=0),N.sum(Eylist,axis=0),N.sum(Ezlist,a
    xis=0)
175.             return N.abs(Exnet)**2 + N.abs(Eynet)**2 + N.abs(Eznet)**2
176.
177.         def otf_from_fields(Elist):
178.             '''''This returns the OTF from the electric fields. The PSF is an intermedia
    te step.'''
179.             return N.fft.fftshift(N.abs(N.fft.fftn(psf(Elist))))
180.
181.         def otf_from_psf(psf):
```

```
182.            '''''This returns the OTF directly from the psf.'''
183.            return N.fft.fftshift(N.abs(N.fft.fftn(psf)))
```

A.3 Phase at Pupils Code

A.3.1 “angspec” module

Note that this calls on the angspec_tools module. It is included just after this one.

```
1.  import numpy as N
2.  import angspec_tools as ast
3.  import divider
4.
5.
6.  class O(object):
7.
8.      def __init__(self,theta=0,dz_obj=0):
9.          ''''''Sets parameters for an individual objective lens and outputs the lens as a
    n object.
10.         Theta is the angular position of an objective as measured counter-
    clockwise from the 'a' objective.
11.         For example, following Fig. 6.1 and assuming the standard geometry,
12.         the 'a' objective has theta=0; 'b', theta=180; 'c',theta=240.
13.         The objective is assumed to have its focal point at the origin of the coordinat
    e system (dz_obj=0).
14.         dz_obj allows for defocusing the objective (focal point not at origin).'''

15.         self.theta = N.deg2rad(theta)
16.         self.dz_obj = dz_obj
17.
18.         if self.theta >= 0 and  self.theta <= N.pi/2:
19.             self.rho = self.theta/(N.pi/2)
20.         elif self.theta > N.pi/2 and self.theta <= N.pi:
21.             self.rho = (N.pi - self.theta)/(N.pi/2)
22.         elif self.theta > N.pi and self.theta <= 3*N.pi/2:
23.             self.rho = -(self.theta-N.pi)/(N.pi/2)
24.         elif self.theta > 3*N.pi/2 and self.theta <= 2*N.pi:
25.             self.rho = -(2*N.pi - self.theta)/(N.pi/2)
26.
27. class P(object):
28.     '''''This object determines the phase across each pupil for a given arrangement.
29.     (xi_abs,eta_abs,z0_abs) are the (x,y,z) coordinates in Fig. 6.1 of the text.
30.     These determine the position of the point source.
31.     P.puplist_wrap returns a stack of the individual pupils and the phase across each.
    The phase is wrapped here.
32.     P.syspup returns the system pupil. This is how the pupils from each objective
33.     should be arranged at the tube lens. P.puplist_un is similar to P.puplist_wrap, exc
    ept
34.     the phase is inwrapped in this case. P._psfpoint() is a function that returns
35.     the electric field at a chosen point in image space due to the system pupil.'''
36.     def __init__(self,xi_abs,eta_abs,z0_abs,objectives,M=63.0,NA=0.9,f2=200000.0,l=0.51
    5,n_medium=1.33,pupnum=257):
37.         self.M = M
38.         self.f2 = f2
39.         self.NA = NA
40.         self.n_medium = n_medium
```

```
41.         self.l  = l
42.
43.         self.f1 = self.f2/self.M
44.         self.dtheta_obj = N.arcsin(self.NA/self.n_medium)
45.         self.R_obj = (self.dtheta_obj/(N.pi/2))*self.n_medium*self.f1
46.         self.R_pupil = self.n_medium*self.f1  #NA*F where sin(theta) = 1
47.
48.         xlist,ylist = N.linspace(-self.R_pupil,self.R_pupil,pupnum),N.linspace(-
    self.R_pupil,self.R_pupil,pupnum)
49.         self.xx,self.yy = N.meshgrid(xlist,ylist)
50.
51.         for O in objectives:
52.             O.f = self.f1
53.
54.         func = lambda O,yarg: N.exp(1j*ast.phase(O.xis,O.etas,O.z0s,self.xx,yarg,O.f,l,
    'front'))*((yarg)**2 + self.xx**2 < self.R_obj**2)
55.         func_unwrap = lambda O,yarg: ast.phase(O.xis,O.etas,O.z0s,self.xx,yarg,O.f,l,'f
    ront')*((yarg)**2 + self.xx**2 < self.R_obj**2)
56.
57.         Plist = []
58.         Plist_centered_wrapped = []
59.         Plist_centered_unwrapped = []
60.
61.         for O in objectives:
62.             ast.abs_to_rel(O,xi_abs,eta_abs,z0_abs)
63.             Plist_centered_wrapped.append(N.fliplr(N.rot90((N.angle(func(O,self.yy))*(1
    -(N.angle(func(O,self.yy))==N.pi)))[N.round(0.2*pupnum):pupnum-
    N.round(0.2*pupnum),N.round(0.2*pupnum):pupnum-N.round(0.2*pupnum)])))
64.             Plist.append(func(O,self.yy - O.rho*self.R_pupil))
65.             Plist_centered_unwrapped.append(N.fliplr(N.rot90(func_unwrap(O,self.yy)[N.r
    ound(0.2*pupnum):pupnum-N.round(0.2*pupnum),N.round(0.2*pupnum):pupnum-
    N.round(0.2*pupnum)])))
66.
67.         P = N.sum(Plist,axis=0)*(self.xx**2 + self.yy**2 < self.R_pupil**2)
68.
69.         self.puplist_wrap = Plist_centered_wrapped
70.         self.syspup = P
71.         self.puplist_un = Plist_centered_unwrapped
72.         self.p_phase = N.angle(P)
73.         self.p_abs = N.abs(P)
74.
75.     def _psfpoint(self,mu=0.0,nu=0.0,z1=0.0):
76.         self.upoint,self.psfpoint = ast.psfpoint(self.P,self.xx,self.yy,self.R_pupil,se
    lf.l,self.f2,mu,nu,z1)
77.
78.
79. class psf(object):
80.     '''''The first three parameters of this object can be either a range of values or a
     single point.
81.     For example, xi_abs_range=(4.0,256) does 256 data points in the range -2<=x<=2.
82.     xi_abs_range=(0.0,1) does a single point at the origin. In this way, the field
83.     can be computed for an arbitrarily shaped volume, plane or line in image space.
84.     The system pupil is an intermediate step in the determination of the field. Therefo
    re,
85.     this is a good check to verify that the geometry of the system pupil is correct.
86.     pupshow=True saves the system pupil resulting from each point in the chosen data ra
    nge.
87.     Note that pupshow will, in addition to a xnum x ynum x znum psf, create
88.     an xnum x ynum x znum array of pnum x pnum arrays. This will cause memory issues
```

```
    for more than a few points. Leave pupshow=False for volumes more than a few points.
    '''
    def __init__(self,xi_abs_range,eta_abs_range,z0_abs_range,objectives,imscale=True,pupshow=False,mu=0.0,nu=0.0,z1=0.0,M=63.0,NA=0.9,f2=200000.0,l=0.515,n_medium=1.33,pupnum=256):
        import time
        start_time = time.time()

        self.M = M
        self.f2 = f2
        self.NA = NA
        self.n_medium = n_medium

        self.f1 = self.f2/self.M
                self.dtheta_obj = N.arcsin(self.NA/self.n_medium)
                self.l  = l
                self.R_obj = (self.dtheta_obj/(N.pi/2))*self.n_medium*self.f1  #This is the pupil radius.
                self.R_pupil = self.n_medium*self.f1  #This is the hemisphere radius. NA*F where sin(theta) = 1

                xlist,ylist = N.linspace(-self.R_pupil,self.R_pupil,pupnum),N.linspace(-self.R_pupil,self.R_pupil,pupnum)
                self.xx,self.yy = N.meshgrid(xlist,ylist)

                for O in objectives:
                    O.f = self.f1

                xilist = N.linspace(-xi_abs_range[0]/2,xi_abs_range[0]/2,xi_abs_range[1])
                etalist = N.linspace(-eta_abs_range[0]/2,eta_abs_range[0]/2,eta_abs_range[1])
                z0list = N.linspace(-z0_abs_range[0]/2,z0_abs_range[0]/2,z0_abs_range[1])

                xic,etac,z0c = N.meshgrid(xilist,etalist,z0list,indexing='ij')

                X,Y,Z,mode = divider.divider(xic,etac,z0c,divisions=3)

                if pupshow == False: #pupshow==True saves the pupnum x pupnum system pupil for each point (xi,eta,z0). pupnum should be off when creating PSFs due to amount of points.

                    def psfbuilder(xic,etac,z0c,objectives,xx,yy,R_pupil,R_obj,l,f2,mu,nu,z1,pupnum): #This function builds the PSF
                        psf = N.zeros((xic.shape[0],xic.shape[1],xic.shape[2]))
                        func = lambda O,yarg: N.exp(1j*ast.phase(O.xis,O.etas,O.z0s,xx,yarg,O.f,l,'front'))*((yarg)**2 + xx**2 < R_obj**2)
                        for i in range(psf.shape[0]):
                            for j in range(psf.shape[1]):
                                for k in range(psf.shape[2]):
                                    Plist = []
                                    for O in objectives:
                                        ast.abs_to_rel(O,xic[i,j,k],etac[i,j,k],z0c[i,j,k])
                                        Plist.append(func(O,yy - O.rho*R_pupil))
                                    P = N.sum(Plist,axis=0)*(xx**2 + yy**2 < R_pupil**2)
```

```
132.                                     psf[i,j,k] = ast.psfpoint(P,xx,yy,R_pupil,l,f2,mu,nu
    ,z1)[1]
133.                         return psf
134.
135.                     import pp #parallel python allows parallel computation across multip
    le CPU cores.
136.                     job_server = pp.Server()
137.                     fn = pp.Template(job_server, psfbuilder, (), ("numpy as N", "angspec
    _tools as ast",))
138.
139.                     if imscale == True:#IMPORTANT STEP. This accounts for magnification
    of the objective.
140.                         mu,nu,z1 = self.M*mu,self.M*nu,(self.M**2)*z1
141.
142.                     job1 = fn.submit(X[0],Y[0],Z[0],objectives,self.xx,self.yy,self.R_pu
    pil,self.R_obj,self.l,self.f2,mu,nu,z1,pupnum) #Parallel python here through 165
143.                     job2 = fn.submit(X[1],Y[1],Z[1],objectives,self.xx,self.yy,self.R_pu
    pil,self.R_obj,self.l,self.f2,mu,nu,z1,pupnum)
144.                     job3 = fn.submit(X[2],Y[2],Z[2],objectives,self.xx,self.yy,self.R_pu
    pil,self.R_obj,self.l,self.f2,mu,nu,z1,pupnum)
145.
146.                     psf1 = job1()
147.                     psf2 = job2()
148.                     psf3 = job3()
149.
150.                     if mode == 'x':
151.                         self.psf = N.concatenate((psf1,psf2,psf3),axis=0)
152.                     elif mode == 'y':
153.                         self.psf = N.concatenate((psf1,psf2,psf3),axis=1)
154.                     elif mode == 'z':
155.                         self.psf = N.concatenate((psf1,psf2,psf3),axis=2)
156.
157.                 elif pupshow == True: #Explained above.
158.
159.                     def psfbuilder(xic,etac,z0c,objectives,xx,yy,R_pupil,R_obj,l,f2,mu,n
    u,z1,pupnum):
160.                         psf = N.zeros((xic.shape[0],xic.shape[1],xic.shape[2]))
161.                         puparr = N.zeros((xic.shape[0],xic.shape[1],xic.shape[2]),dtype=
    N.ndarray)
162.                         func = lambda O,yarg: N.exp(1j*ast.phase(O.xis,O.etas,O.z0s,xx,y
    arg,O.f,l,'front'))*((yarg)**2 + xx**2 < R_obj**2)
163.                         for i in range(psf.shape[0]):
164.                             for j in range(psf.shape[1]):
165.                                 for k in range(psf.shape[2]):
166.                                     Plist = []
167.                                     for O in objectives:
168.                                         ast.abs_to_rel(O,xic[i,j,k],etac[i,j,k],z0c[i,j,
    k])
169.                                         Plist.append(func(O,yy - O.rho*R_pupil))
170.                                     P = N.sum(Plist,axis=0)*(xx**2 + yy**2 < R_pupil**2)

171.                                     puparr[i,j,k] = P
172.                                     psf[i,j,k] = ast.psfpoint(P,xx,yy,R_pupil,l,f2,mu,nu
    ,z1)[1]
173.                         return puparr,psf
174.
175.                     import pp
176.                     job_server = pp.Server()
```

```
                    fn = pp.Template(job_server, psfbuilder, (), ("numpy as N", "angspec
    _tools as ast",))

                    if imscale == True:
                        mu,nu,z1 = self.M*mu,self.M*nu,(self.M**2)*z1

                    job1 = fn.submit(X[0],Y[0],Z[0],objectives,self.xx,self.yy,self.R_pu
    pil,self.R_obj,self.l,self.f2,mu,nu,z1,pupnum)
                    job2 = fn.submit(X[1],Y[1],Z[1],objectives,self.xx,self.yy,self.R_pu
    pil,self.R_obj,self.l,self.f2,mu,nu,z1,pupnum)
                    job3 = fn.submit(X[2],Y[2],Z[2],objectives,self.xx,self.yy,self.R_pu
    pil,self.R_obj,self.l,self.f2,mu,nu,z1,pupnum)

                    puparr1,psf1 = job1()
                    puparr2,psf2 = job2()
                    puparr3,psf3 = job3()

                    if mode == 'x':
                        self.puparr,self.psf = N.concatenate((puparr1,puparr2,puparr3),a
    xis=0),N.concatenate((psf1,psf2,psf3),axis=0)
                    elif mode == 'y':
                        self.puparr,self.psf = N.concatenate((puparr1,puparr2,puparr3),a
    xis=1),N.concatenate((psf1,psf2,psf3),axis=1)
                    elif mode == 'z':
                        self.puparr,self.psf = N.concatenate((puparr1,puparr2,puparr3),a
    xis=2),N.concatenate((psf1,psf2,psf3),axis=2)

                end_time = time.time()
                print('Total computation time was '+repr(end_time-
    start_time)+' seconds.')
```

A.3.2 “angspec_tools” module

```
import numpy as N
import simpson


def abs_to_rel(O1,xis_abs,etas_abs,z0s_abs):
    '''''This converts the coordinates of the point source from the absolute
    coordinate system to the coordinate system relative to the objective.'''
    O1.xis = N.float64(xis_abs)
    O1.etas = N.float64(-(etas_abs*N.cos(O1.theta) + z0s_abs*N.sin(O1.theta)))
    O1.z0s = N.float64(-(-
etas_abs*N.sin(O1.theta) + z0s_abs*N.cos(O1.theta)) + O1.dz_obj)

def phase(a,b,c,x,y,f,l,mode):
    '''''This function finds the phase across the pupil. x,y is a meshgrid of points in
     this application.'''
    k = 2*N.pi/l
    if mode == 'front':
        phase = k*(N.sqrt((x-a)**2 + (y-b)**2 + (N.sqrt(f**2 - x**2 - y**2) - c)**2) -
     f)
    elif mode == 'back':
        phase = k*(N.sqrt((x-a)**2 + (y-b)**2 + (c + N.sqrt(f**2 - x**2 - y**2))**2) -
     f)
```

```
    else:
        print('Please choose either front or back for mode')
    try:
        phase[N.isnan(phase)] = 0.0
    except:
        if N.isnan(phase):
            phase = 0.0
    return phase

def psfpoint(P,xx,yy,R_pupil,l,f2,mu=0.0,nu=0.0,z1=0.0):
    '''''This finds the electric field and intensity for a single point in image space

    due to the distribution P at the tube lens.'''
    integrand = P * N.exp(1j*phase(mu,nu,z1,xx,yy,f2,l,'back'))
    u = simpson.dblsimps_disc(integrand,(-R_pupil,R_pupil),(-R_pupil,R_pupil))
    psf = N.abs(u)**2
    return u,psf
```

A.4 Widefield Code

"evec_wf" module

```
import numpy as N
import simpson
import time
import divider


class EMatwf(object):
    '''''This returns the electric field distribution resulting from an oblique
    focal plane (chapter 5). This is a modified version of the method described
    by Kim et al. It allows for -pi/2<=alpha<=pi/2, whereas the Kim version is
    restricted to 0<=alpha<=pi/2. When alpha=0.0, this returns the same results
    as Richards and Wolf (full pupil).'''
    def __init__(self,xin=(4.0,256),yin=(4.0,256),zin=(4.0,256),phi0=0.0,NA=0.9,n=1.33,
theta=0.0,alpha=0.0,l=0.515,tnum=50,pnum=50):
        start_time = time.time()

        theta = N.deg2rad(theta)
        alpha = N.deg2rad(alpha)

        xlist = N.linspace(-xin[0]/2,xin[0]/2,xin[1])
        ylist = N.linspace(-yin[0]/2,yin[0]/2,yin[1])
        zlist = N.linspace(-zin[0]/2,zin[0]/2,zin[1])

        xA,yA,zA = N.meshgrid(xlist,ylist,zlist,indexing='ij')

        def xrot(xp,yp,zp,angle):
            x = xp
            y = yp*N.cos(angle) - zp*N.sin(angle)
            z = yp*N.sin(angle) + zp*N.cos(angle)
            return x,y,z

        #Transforming coordinates from absolute coord to objective relative coord
```

```
32.         xc,yc,zc = xrot(xA,yA,zA,-theta)
33.
34.         #Dividing calculation into three sets of points,
35.         X,Y,Z,mode = divider.divider(xc,yc,zc,divisions=3)
36.
37.         if alpha >= 0.0:
38.             def E(xarr,yarr,zarr,phi0,NA,n,alph,l,tnum,pnum):
39.                 #Constants
40.                 k = 2*N.pi/l
41.                 thetac = N.arccos(N.abs((NA/n)*N.sin(alph) + N.sqrt(1 -
    (NA/n)**2)*N.cos(alph)))
42.                 yc = -(NA/n)*N.cos(alph) + N.sqrt(1 - (NA/n)**2)*N.sin(alph)
43.                 thetamax = N.arcsin(NA/n)
44.
45.                 ##########################################
46.                 #Functions of theta and phi
47.
48.                 phi1 = lambda theta: N.arcsin(N.abs(-
   (1/N.tan(alph))*(1/N.tan(theta)) + N.sqrt(1 -
    (NA/n)**2)*(1/N.sin(alph))*(1/N.sin(theta))))
49.
50.                 Exfunc = lambda theta,phi: N.sin(phi - phi0)*N.sin(phi) + N.cos(phi -
    phi0)*N.cos(theta)*N.cos(phi)
51.                 Eyfunc = lambda theta,phi: -N.sin(phi - phi0)*N.cos(phi) + N.cos(phi -
    phi0)*N.cos(theta)*N.sin(phi)
52.                 Ezfunc = lambda theta,phi: N.cos(phi - phi0)*N.sin(theta)
53.
54.                 def P1(theta,phi):
55.
56.                     P1 = N.less_equal(0.0,theta)*N.less_equal(theta,thetac)*N.less_equa
   l(0.0,phi)*N.less_equal(phi,2*N.pi)*N.less(yc,0.0)
57.                     return P1
58.
59.                 def P2(theta,phi):
60.
61.                     phi1_ = phi1(theta)
62.                     P2 = N.less_equal(thetac,theta)*N.less_equal(theta,thetamax)*N.less
   _equal(phi1_,phi)*N.less_equal(phi,(N.pi - phi1_))
63.                     return P2
64.                 ##########################################
65.
66.                 xnum,ynum,znum = xarr.shape
67.                 Ex,Ey,Ez = N.zeros((xnum,ynum,znum),dtype=complex),N.zeros((xnum,ynum,z
   num),dtype=complex),N.zeros((xnum,ynum,znum),dtype=complex)
68.                 for nx in range(xnum):
69.                     for ny in range(ynum):
70.                         for nz in range(znum):
71.
72.                             part = lambda theta,phi,x=xarr[nx,ny,nz],y=yarr[nx,ny,nz],z
   =zarr[nx,ny,nz]: (N.cos(theta)**(0.5))*N.sin(theta)*N.exp(-
   1j*k*(xarr[nx,ny,nz]*N.sin(theta)*N.cos(phi) + yarr[nx,ny,nz]*N.sin(theta)*N.sin(phi) -
    zarr[nx,ny,nz]*N.cos(theta)))
73.
74.                             rExint = lambda theta,phi: N.real(Exfunc(theta,phi)*(P1(the
   ta,phi) + P2(theta,phi))*part(theta,phi))
75.                             iExint = lambda theta,phi: N.imag(Exfunc(theta,phi)*(P1(the
   ta,phi) + P2(theta,phi))*part(theta,phi))
76.                             rEyint = lambda theta,phi: N.real(Eyfunc(theta,phi)*(P1(the
   ta,phi) + P2(theta,phi))*part(theta,phi))
```

```
77.                             iEyint = lambda theta,phi: N.imag(Eyfunc(theta,phi)*(P1(the
    ta,phi) + P2(theta,phi))*part(theta,phi))
78.                             rEzint = lambda theta,phi: N.real(Ezfunc(theta,phi)*(P1(the
    ta,phi) + P2(theta,phi))*part(theta,phi))
79.                             iEzint = lambda theta,phi: N.imag(Ezfunc(theta,phi)*(P1(the
    ta,phi) + P2(theta,phi))*part(theta,phi))
80.
81.                             rEx = simpson.dblsimps(rExint,(0.0,thetamax,tnum),(0.0,2*N.
    pi,pnum))
82.                             iEx = simpson.dblsimps(iExint,(0.0,thetamax,tnum),(0.0,2*N.
    pi,pnum))
83.                             rEy = simpson.dblsimps(rEyint,(0.0,thetamax,tnum),(0.0,2*N.
    pi,pnum))
84.                             iEy = simpson.dblsimps(iEyint,(0.0,thetamax,tnum),(0.0,2*N.
    pi,pnum))
85.                             rEz = simpson.dblsimps(rEzint,(0.0,thetamax,tnum),(0.0,2*N.
    pi,pnum))
86.                             iEz = simpson.dblsimps(iEzint,(0.0,thetamax,tnum),(0.0,2*N.
    pi,pnum))
87.
88.                             Ex[nx,ny,nz] = N.complex(rEx,iEx)
89.                             Ey[nx,ny,nz] = N.complex(rEy,iEy)
90.                             Ez[nx,ny,nz] = N.complex(rEz,iEz)
91.
92.                 return Ex,Ey,Ez
93.
94.         elif alpha < 0.0:
95.             def E(xarr,yarr,zarr,phi0,NA,n,alph,l,tnum,pnum):
96.                 alph = -alph
97.                 #Constants
98.                 k = 2*N.pi/l
99.                 thetac = N.arccos(N.abs((NA/n)*N.sin(alph) + N.sqrt(1 -
     (NA/n)**2)*N.cos(alph)))
100.                        yc = (NA/n)*N.cos(alph) - N.sqrt(1 - (NA/n)**2)*N.sin(alph)
101.                        thetamax = N.arcsin(NA/n)
102.
103.                        ##########################################
104.                        #Functions of theta and phi
105.                        phi1 = lambda theta: N.pi + N.arcsin(N.abs(-
    (1/N.tan(alph))*(1/N.tan(theta)) + N.sqrt(1 -
     (NA/n)**2)*(1/N.sin(alph))*(1/N.sin(theta))))
106.
107.                        Exfunc = lambda theta,phi: N.sin(phi -
     phi0)*N.sin(phi) + N.cos(phi - phi0)*N.cos(theta)*N.cos(phi)
108.                        Eyfunc = lambda theta,phi: -N.sin(phi -
     phi0)*N.cos(phi) + N.cos(phi - phi0)*N.cos(theta)*N.sin(phi)
109.                        Ezfunc = lambda theta,phi: N.cos(phi - phi0)*N.sin(theta)
110.
111.                        def P1(theta,phi):
112.
113.                            P1 = N.less_equal(0.0,theta)*N.less_equal(theta,thetac)*N.le
    ss_equal(0.0,phi)*N.less_equal(phi,2*N.pi)*N.less(0.0,yc)
114.                            return P1
115.
116.                        def P2(theta,phi):
117.
118.                            phi1_ = phi1(theta)
119.                            P2 = N.less_equal(thetac,theta)*N.less_equal(theta,thetamax)
    *N.less_equal(phi1_,phi)*N.less_equal(phi,(3*N.pi - phi1_))
```

```
                            return P2
                        ########################################

                        xnum,ynum,znum = xarr.shape
                        Ex,Ey,Ez = N.zeros((xnum,ynum,znum),dtype=complex),N.zeros((xnum
    ,ynum,znum),dtype=complex),N.zeros((xnum,ynum,znum),dtype=complex)
                        for nx in range(xnum):
                            for ny in range(ynum):
                                for nz in range(znum):

                                    part = lambda theta,phi,x=xarr[nx,ny,nz],y=yarr[nx,n
    y,nz],z=zarr[nx,ny,nz]: (N.cos(theta)**(0.5))*N.sin(theta)*N.exp(-
    1j*k*(xarr[nx,ny,nz]*N.sin(theta)*N.cos(phi) + yarr[nx,ny,nz]*N.sin(theta)*N.sin(phi) -
     zarr[nx,ny,nz]*N.cos(theta)))

                                    rExint = lambda theta,phi: N.real(Exfunc(theta,phi)*
    (P1(theta,phi) + P2(theta,phi))*part(theta,phi))
                                    iExint = lambda theta,phi: N.imag(Exfunc(theta,phi)*
    (P1(theta,phi) + P2(theta,phi))*part(theta,phi))
                                    rEyint = lambda theta,phi: N.real(Eyfunc(theta,phi)*
    (P1(theta,phi) + P2(theta,phi))*part(theta,phi))
                                    iEyint = lambda theta,phi: N.imag(Eyfunc(theta,phi)*
    (P1(theta,phi) + P2(theta,phi))*part(theta,phi))
                                    rEzint = lambda theta,phi: N.real(Ezfunc(theta,phi)*
    (P1(theta,phi) + P2(theta,phi))*part(theta,phi))
                                    iEzint = lambda theta,phi: N.imag(Ezfunc(theta,phi)*
    (P1(theta,phi) + P2(theta,phi))*part(theta,phi))

                                    rEx = simpson.dblsimps(rExint,(0.0,thetamax,tnum),(0
    .0,2*N.pi,pnum))
                                    iEx = simpson.dblsimps(iExint,(0.0,thetamax,tnum),(0
    .0,2*N.pi,pnum))
                                    rEy = simpson.dblsimps(rEyint,(0.0,thetamax,tnum),(0
    .0,2*N.pi,pnum))
                                    iEy = simpson.dblsimps(iEyint,(0.0,thetamax,tnum),(0
    .0,2*N.pi,pnum))
                                    rEz = simpson.dblsimps(rEzint,(0.0,thetamax,tnum),(0
    .0,2*N.pi,pnum))
                                    iEz = simpson.dblsimps(iEzint,(0.0,thetamax,tnum),(0
    .0,2*N.pi,pnum))

                                    Ex[nx,ny,nz] = N.complex(rEx,iEx)
                                    Ey[nx,ny,nz] = N.complex(rEy,iEy)
                                    Ez[nx,ny,nz] = N.complex(rEz,iEz)

                        return Ex,Ey,Ez

                import pp
                job_server = pp.Server()
                fn = pp.Template(job_server, E, (), ("numpy as N", "simpson",))

                job1 = fn.submit(X[0],Y[0],Z[0],phi0,NA,n,alpha,l,tnum,pnum)
                job2 = fn.submit(X[1],Y[1],Z[1],phi0,NA,n,alpha,l,tnum,pnum)
                job3 = fn.submit(X[2],Y[2],Z[2],phi0,NA,n,alpha,l,tnum,pnum)
                E1 = job1()
                E2 = job2()
                E3 = job3()

                if mode == 'x':
```

```
163.                     Ex,Ey,Ez = N.concatenate((E1[0],E2[0],E3[0]),axis=0),N.concatenate((
    E1[1],E2[1],E3[1]),axis=0),N.concatenate((E1[2],E2[2],E3[2]),axis=0)
164.                 elif mode == 'y':
165.                     Ex,Ey,Ez = N.concatenate((E1[0],E2[0],E3[0]),axis=1),N.concatenate((
    E1[1],E2[1],E3[1]),axis=1),N.concatenate((E1[2],E2[2],E3[2]),axis=1)
166.                 elif mode == 'z':
167.                     Ex,Ey,Ez = N.concatenate((E1[0],E2[0],E3[0]),axis=2),N.concatenate((
    E1[1],E2[1],E3[1]),axis=2),N.concatenate((E1[2],E2[2],E3[2]),axis=2)
168.
169.                 Ex,Ey,Ez = xrot(Ex,Ey,Ez,theta)
170.                 self.Ex,self.Ey,self.Ez = N.squeeze(Ex),N.squeeze(Ey),N.squeeze(Ez)
171.
172.                 end_time = time.time()
173.                 print('Computation completed in '+repr(end_time-
    start_time)+' seconds')
174.
175.             def getpsf(self):
176.                 self.psf = N.abs(self.Ex)**2 + N.abs(self.Ey)**2 + N.abs(self.Ez)**2
177.
178.
179.         def psf(Elist):
180.             '''''SEE evec_clipping FOR DESCRIPTION.'''
181.             Exlist,Eylist,Ezlist = [],[],[]
182.             for E in Elist:
183.                 Exlist.append(E.Ex),Eylist.append(E.Ey),Ezlist.append(E.Ez)
184.             Exnet,Eynet,Eznet = N.sum(Exlist,axis=0),N.sum(Eylist,axis=0),N.sum(Ezlist,a
    xis=0)
185.             return N.abs(Exnet)**2 + N.abs(Eynet)**2 + N.abs(Eznet)**2
186.
187.         def otf(Elist):
188.             '''''SEE evec_clipping FOR DESCRIPTION.'''
189.             return N.fft.fftshift(N.abs(N.fft.fftn(psf(Elist))))
190.
191.         def otf_from_psf(psf):
192.             '''''SEE evec_clipping FOR DESCRIPTION.'''
193.             return N.fft.fftshift(N.abs(N.fft.fftn(psf)))
```

A.5 Utility Modules

A.5.1 "divider" module

```
1.  import numpy as N
2.
3.
4.  def divider(xarr,yarr,zarr,divisions=3):
5.          '''''This takes input coordinate arrays (3D Meshgrid) and
6.          divides each of them into 'divisions' smaller arrays. This is so that
7.          parallel python module can operate simultaneously on the multiple, smaller
8.          arrays and the concatenate the results after computation. 'divisions'
9.          should be the number of available cpu cores for calculation.'''
10.         xlen,ylen,zlen = xarr.shape
11.
12.         #Determine axis to divide (largest one)
13.         if ylen > xlen:
```

```
            mode = 'y'
        elif zlen > ylen:
            mode = 'z'
        elif xlen > zlen:
            mode = 'x'
        elif xlen == ylen or xlen == zlen:
            mode = 'x'
        else:
            mode = 'y'

        #Divide along chosen axis for 'divisions' divisions.
        if mode == 'x':
            X,Y,Z = [],[],[]
            for i in range(divisions):
                a,b = (i*xlen)//divisions,((i+1)*xlen)//divisions
                X.append(xarr[a:b,:,:])
                Y.append(yarr[a:b,:,:])
                Z.append(zarr[a:b,:,:])

        if mode == 'y':
            X,Y,Z = [],[],[]
            for i in range(divisions):
                a,b = (i*ylen)//divisions,((i+1)*ylen)//divisions
                X.append(xarr[:,a:b,:])
                Y.append(yarr[:,a:b,:])
                Z.append(zarr[:,a:b,:])

        if mode == 'z':
            X,Y,Z = [],[],[]
            for i in range(divisions):
                a,b = (i*zlen)//divisions,((i+1)*zlen)//divisions
                X.append(xarr[:,:,a:b])
                Y.append(yarr[:,:,a:b])
                Z.append(zarr[:,:,a:b])

        return X,Y,Z,mode
```

A.5.2 “simpson” module

```
import numpy as N
from scipy import integrate as Int

def dblsimps(integrand,xparams,yparams):
    '''''Performs a 2D Simpson integration by taking discrete samples from a given inte
grand
    function over the given integration ranges. The integrand must be a lambda function

    of the form lambda x,y: ___. xparams is of the form (xa,xb,xnum) where xa is
    the bottom integration bound, xb is the top integration bound and xnum is the
    number of samples taken from this range.'''
    xa,xb,xnum = xparams[0],xparams[1],xparams[2]
    ya,yb,ynum = yparams[0],yparams[1],yparams[2]
    x = N.linspace(xa,xb,num=xnum)
    y = N.linspace(ya,yb,num=ynum)
    f = integrand(x[:,None],y)
    return Int.simps(Int.simps(f, x), y)
```